

1999

# Computer modeling of ultrashort pulsed laser ablation of diamond and graphite with experimental verification

Michael D. Shirk  
*Iowa State University*

Follow this and additional works at: <https://lib.dr.iastate.edu/rtd>

 Part of the [Mechanical Engineering Commons](#)

## Recommended Citation

Shirk, Michael D., "Computer modeling of ultrashort pulsed laser ablation of diamond and graphite with experimental verification " (1999). *Retrospective Theses and Dissertations*. 12483.  
<https://lib.dr.iastate.edu/rtd/12483>

This Dissertation is brought to you for free and open access by the Iowa State University Capstones, Theses and Dissertations at Iowa State University Digital Repository. It has been accepted for inclusion in Retrospective Theses and Dissertations by an authorized administrator of Iowa State University Digital Repository. For more information, please contact [digirep@iastate.edu](mailto:digirep@iastate.edu).

## INFORMATION TO USERS

This manuscript has been reproduced from the microfilm master. UMI films the text directly from the original or copy submitted. Thus, some thesis and dissertation copies are in typewriter face, while others may be from any type of computer printer.

**The quality of this reproduction is dependent upon the quality of the copy submitted.** Broken or indistinct print, colored or poor quality illustrations and photographs, print bleedthrough, substandard margins, and improper alignment can adversely affect reproduction.

In the unlikely event that the author did not send UMI a complete manuscript and there are missing pages, these will be noted. Also, if unauthorized copyright material had to be removed, a note will indicate the deletion.

Oversize materials (e.g., maps, drawings, charts) are reproduced by sectioning the original, beginning at the upper left-hand corner and continuing from left to right in equal sections with small overlaps.

Photographs included in the original manuscript have been reproduced xerographically in this copy. Higher quality 6" x 9" black and white photographic prints are available for any photographs or illustrations appearing in this copy for an additional charge. Contact UMI directly to order.

Bell & Howell Information and Learning  
300 North Zeeb Road, Ann Arbor, MI 48106-1346 USA

**UMI**<sup>®</sup>  
800-521-0600



Computer modeling of ultrashort pulsed laser ablation  
of diamond and graphite with experimental verification

by

Michael D. Shirk

A dissertation submitted to the graduate faculty  
in partial fulfillment of the requirements for the degree of  
DOCTOR OF PHILOSOPHY

Major: Mechanical Engineering  
Major Professor: Palaniappa Molian

Iowa State University

Ames, Iowa

1999

Copyright ©Michael D. Shirk, 1999. All rights reserved

UMI Number: 9950119

UMI<sup>®</sup>

---

UMI Microform 9950119

Copyright 2000 by Bell & Howell Information and Learning Company.

All rights reserved. This microform edition is protected against  
unauthorized copying under Title 17, United States Code.

---

Bell & Howell Information and Learning Company

300 North Zeeb Road

P.O. Box 1346

Ann Arbor, MI 48106-1346

Graduate College  
Iowa State University

This is to certify that the Doctoral dissertation of  
Michael D. Shirk  
has met the dissertation requirements of Iowa State University

Signature was redacted for privacy.

Major Professor

Signature was redacted for privacy.

For the Major Program

Signature was redacted for privacy.

For the Graduate College

## DEDICATION

I dedicate this work to the people who have been very supportive to me throughout my life so far. To my major professor, Pal Molian, you have been an example of integrity, patience, and straight talk that I hope to live up to. I am greatly appreciative of your help and support over these three years that I have worked with you. To my parents, Jerry and Nancy, you have always been there for me and encouraged me to be my best. Your support has made my life both easier and more fulfilling. Finally, I would like to give my greatest thanks to my wife Jenny, who has stood by me here in Ames as our friends have come and gone. It has been an interesting journey that I have had with you as I completed first my Masters and now my Doctorate. You have also given me the joy of our new son Joseph, who is the inspiration for my continued desire to excel. Thank you all, I honestly could not have finished any of this without your help and support.

## TABLE OF CONTENTS

LIST OF FIGURES	vi
LIST OF TABLES	x
ABSTRACT	xi
CHAPTER 1. INTRODUCTION	1
CHAPTER 2. BACKGROUND	6
CHAPTER 3. A REVIEW OF ULTRASHORT PULSED LASER ABLATION OF MATERIALS	14
CHAPTER 4. ULTRASHORT PULSED LASER ABLATION OF DIAMOND	49
CHAPTER 5. MOLECULAR DYNAMICS MODELING OF ULTRASHORT PULSED LASER ABLATION OF SINGLE CRYSTAL DIAMOND	63
CHAPTER 6. CHIRPED PULSE AMPLIFIED TI:SAPPHIRE LASER ABLATION OF DIAMOND: MODELING AND EXPERIMENTAL VERIFICATION	73
CHAPTER 7. FEMTOSECOND LASER-INDUCED PERIODIC STRUCTURE WRITING ON DIAMOND CRYSTALS AND MICRO-CLUSTERS	96
CHAPTER 8. ULTRASHORT PULSED LASER ABLATION OF HIGHLY ORIENTED PYROLYTIC GRAPHITE	108
CHAPTER 9. GENERAL CONCLUSIONS	143
CHAPTER 10. FUTURE RESEARCH	146
APPENDIX A. ULTRASHORT PULSED TITANIUM SAPPHIRE LASER SYSTEM	148
APPENDIX B. FINITE DIFFERENCE CODE FOR ELECTRON AND LATTICE TEMPERATURES	154
APPENDIX C. DESCRIPTION OF TIGHT-BINDING MOLECULAR DYNAMICS	160
ACKNOWLEDGEMENTS	162

## LIST OF FIGURES

Figure 2-1.	Intensity in Watts/cm <sup>2</sup> with pertinent applications marked	8
Figure 2-2.	A comparison of a stable and an unstable laser cavity (resonator)	10
Figure 2-3.	Beam profile of a typical excimer beam	11
Figure 2-4.	Diagram of an image projection machining setup	13
Figure 3-1.	(a) The positive group delay dispersion expander stretches pulses by making the path length longer for shorter (blue) wavelengths than for longer (red) wavelengths, distributing the various wavelengths over time. (b) The negative group delay dispersion compressor acts to regenerate the initial pulse profile by making the optical path longer for longer (red) wavelengths than shorter (blue) wavelengths.	18
Figure 3-2.	A solid state regenerative amplifier, the seed pulse (vertical polarized) is injected into the system at the input Brewster prism. It is then passed through the amplifier until the voltage is removed from the Q switch, thereby letting the amplified pulse reflect out the output Brewster prism.	19
Figure 3-3.	A simplified schematic of an excimer-dye laser, the excimer laser pumps a short pulsed dye laser, which is then passed through a grating and imaged into the DF DL cell, creating a periodic grating of both refractive and population inverted dye. The output from the DF DL cell is then compressed to 300-500 fs. This output can then be passed through a second harmonic generator to create UV pulses.	20
Figure 4-1.	A plot of 23 ns depth per pulse data vs. fluence for both graphite and CVD diamond thin films.	52
Figure 4-2.	(a) Raman spectra of a CVD diamond thin film which has not been exposed to laser light. (b) Raman spectra of CVD diamond exposed to 23 ns 248 nm pulses.	52
Figure 4-3.	Experimental setup for the 248 nm, 500 fs diamond ablation studies.	56
Figure 4-4.	SEM images of CVD diamond ablated using 400 pulses of 248 nm and 500 fs t fluences of 0.8 J/cm <sup>2</sup> (400E4), 2.86 J/cm <sup>2</sup> (400E3), 4.44 J/cm <sup>2</sup> (400E2), and 6.43 J/cm <sup>2</sup> (400E1).	58
Figure 4-5.	(a) Raman spectra of the surface of untreated single crystal diamond. (b) Raman spectra of a hole ablated in single crystal diamond using 10 248 nm, 500 fs pulses at 6.43 J/cm <sup>2</sup> .	58

Figure 4-6.	Ablation depth per pulse vs. fluence for 500 fs and 23 ns pulses at 248 nm.	59
Figure 4-7.	Experimental data from Konov et al. (see Ref. 5) showing the relation between threshold fluence energy, pulse width and depth per pulse at 248 nm.	59
Figure 5-1.	A plot of temperature profiles for a first order 1-D simulation of the electrons and lattice of diamond during after 100-fs laser ablation.	66
Figure 5-2.	Results from a simulation using ultrashort pulsed conditions, electrons at 15,000 K, lattice at 300 K.	67
Figure 5-3.	Results from a simulation with the electrons and lattice at 2700 K, simulating longer pulsed laser ablation.	68
Figure 5-4.	Ablation depth versus fluence for 23-ns and 500-fs 248-nm lasers on CVD diamond.	70
Figure 6-1.	Beam diagnostics setup, the reticle is placed at the same place that the sample would be so that the image on the camera is identical to that used for ablation.	82
Figure 6-2.	The modified density of states used in this simulation, free electron conditions were assumed above 13 eV	82
Figure 6-3.	Calculated heat capacity for the electron gas in diamond	84
Figure 6-4.	Electron temperature versus absorbed energy for a 100 $\mu\text{m}$ diameter, 10 nm absorption depth region, only applicable to pulse widths less than about 500 fs	84
Figure 6-5.	Results of a finite-difference calculation at $1.3 \times 10^{17} \text{ W/cm}^2$ for a 100 fs pulse	85
Figure 6-6.	(001) diamond surface undergoing thermal decomposition at 4000 K	85
Figure 6-7.	(001) diamond surface undergoing amorphitization at an electron temperature of 25,000 K	86
Figure 6-8.	Thermal decomposition of a (111) surface at 2700 K	87
Figure 6-9.	(111) surface undergoing graphitization at 15,000 K electron temperature	87
Figure 6-10.	Bulk diamond as it undergoes severe atomic disordering at 60,000 K electron temperature	88

Figure 6-11.	SEM image of untreated CVD diamond surface	90
Figure 6-12.	SEM image showing 4 holes ablated in CVD diamond with 1000 pulses, left two at 150 $\mu\text{J}/\text{pulse}$ , right two at 200 $\mu\text{J}/\text{pulse}$ using a 100 $\mu\text{m}$ focused spot size	90
Figure 6-13.	SEM image of a hole ablated in CVD diamond with 1000, 150 $\mu\text{J}$ pulses (100 $\mu\text{m}$ spot size)	91
Figure 6-14.	SEM image of a hole ablated in CVD diamond with 1000, 200 $\mu\text{J}$ pulses (100 $\mu\text{m}$ spot size)	91
Figure 6-15.	AFM image of a hole ablated in single crystal type IIA diamond with 1,000, 120 fs pulses (spot size=90 $\mu\text{m}$ and 200 $\mu\text{J}/\text{pulse}$ )	92
Figure 6-16.	AFM image of a groove ablated in single crystal type IIA diamond with 120 fs pulses at 1 kHz.	92
Figure 6-17.	Raman spectrum of untreated single crystal type IIA diamond	93
Figure 6-18.	Raman spectrum of IIA single crystal type diamond ablated with 825 nm (120 fs) laser	93
Figure 6-19.	Raman spectrum of CVD diamond ablated with 120 fs 150 $\mu\text{J}$ pulses	94
Figure 6-20.	Raman spectrum of CVD diamond in untreated form (a) and ablated with an excimer laser using 23 ns pulses (b)	94
Figure 7-1.	Scanning electron micrographs of a) original untreated single crystal type IIA diamond surface, b) excimer fs laser treated ( $F=1.5 \text{ J}/\text{cm}^2$ , 100 pulses, $\tau_p=380 \text{ fs}$ , $\lambda=248 \text{ nm}$ ) CVD diamond surface, c) same surface at a higher magnification, with multiple periodicities, $\sim 250 \text{ nm}$ as well as $\sim 50$ to 100 nm.	102
Figure 7-2.	Scanning electron micrographs of unpolished CVD diamond irradiated with a Ti-Sapphire fs laser ( $E=2.5 \text{ J}/\text{cm}^2$ , 1000 pulses, $\tau_p=150 \text{ fs}$ , $\lambda=825 \text{ nm}$ ), a) single interference pattern, b) two interference patterns crossing each other at 90 degrees.	103
Figure 7-3.	Scanning electron micrographs of polished CVD diamond irradiated with an excimer fs laser ( $E=0.7 \text{ J}/\text{cm}^2$ , 1000 pulses, $\tau_p=380 \text{ fs}$ , $\lambda=248 \text{ nm}$ ), a) clusters formed around the ablation area, b) at a close-up view, periodic patterns are observable, c) and d) 2 $\mu\text{m}$ sized clusters with concentric periodic ring structures.	104

Figure 7-4.	A schematic of proposed model for formation of 3D interference pattern, and hence writing on diamond clusters	104
Figure 8-1.	Anisotropic layered structure of HOPG	114
Figure 8-2.	Optical setup for beam diagnostics	117
Figure 8-3.	A sample window from the beam diagnostics software	117
Figure 8-4.	A schematic of experimental setup	118
Figure 8-5.	Depth per pulse fit for 2.1 J/cm <sup>2</sup> (120-fs)	121
Figure 8-6.	Depth per pulse fit for 4.2 J/cm <sup>2</sup> (120-fs)	121
Figure 8-7.	Depth per pulse fit for 5.3 J/cm <sup>2</sup> (120-fs)	122
Figure 8-8.	Depth per pulse fit for 10.6 J/cm <sup>2</sup> (120-fs)	122
Figure 8-9.	Plot of depth per pulse showing evidence of saturation above 5.2 J/cm <sup>2</sup> for 120-fs pulses	123
Figure 8-10.	A hole ablated in HOPG with 10,000 (120 fs) pulses	126
Figure 8-11.	A hole ablated in HOPG with 1,000 (120 fs) pulses	126
Figure 8-12.	A hole ablated in HOPG with 1,000 (1 ps) pulses	129
Figure 8-13.	A hole ablated in HOPG with 1,000 (5 ps) pulses	129
Figure 8-14.	A hole ablated in HOPG with 1,000 (10 ps) pulses	130
Figure 8-15.	A hole ablated in HOPG with 1,000 (20 ps) pulses	130
Figure 8-16.	A hole ablated in HOPG with 10,000 (20 ps) pulses	131
Figure 8-17.	Hole ablated with 120 fs, 1 mJ pulses, demonstrating the effects of excess fluence	131
Figure 8-18.	AFM image of HOPG ablated with 120 fs pulses	132
Figure 8-19.	825 nm fringes on the bottom of the hole pictured in Figure 18	132
Figure 8-20.	The edge of a hole ablated with 0.8 J/cm <sup>2</sup> 1 ps pulses	134
Figure 8-21.	A hole ablated in HOPG with 0.8 J/cm <sup>2</sup> 5 ps pulses	134

Figure 8-22.	A hole ablated in HOPG with $0.8 \text{ J/cm}^2$ 10 ps pulses	135
Figure 8-23.	An AFM image of a hole ablated with $50 \times 0.8 \text{ J/cm}^2$ , 20 ps pulses	135
Figure 8-24.	Raman spectra of untreated HOPG	138
Figure 8-25.	Raman spectra of 120 fs treated HOPG	138
Figure 8-26.	Raman spectra of 20 ps treated HOPG	139
Figure 8-27.	Raman spectra of untreated (top) and 248 nm, 28 ns treated (bottom) HOPG	139

## LIST OF TABLES

Table 3-1.	Several examples of current sub-picosecond lasers	17
Table 3-2.	Typical data in vacuum; depth per pulse is for 0.3 J/cm <sup>2</sup>	24
Table 8-1.	Benefits of ultrafast lasers	112
Table 8-2.	Properties of HOPG at room temperature.	114
Table 8-3.	Characteristics of Ti:Sapphire laser	114
Table 8-4.	Micro-Raman parameters.	119

## ABSTRACT

Ultrashort pulsed lasers create a fundamentally different ablation mechanism than that of conventional pulsed lasers because of the ultrashort laser pulse's extreme intensity ( $>10^{12}$  W/cm<sup>2</sup>) and time duration ( $< 10^{-12}$  s), which is shorter than the electron-lattice transfer time ( $>10^{-12}$  s). Consequently, a thermally excited plasma is generated in a cool lattice. Assumptions used in conventional pulsed laser ablation, such as the assumption that absorption processes are governed by the Beer-Lambert Law and that thermal equilibrium of the electrons and lattice is achieved, are invalid for ultrashort pulses. In this work, computer modeling of ultrashort pulsed ablation was performed for large band-gap insulating solids such as diamond. A two-step model was developed in which a heat transfer, finite-difference model was formulated and tight-binding molecular dynamics simulations were performed to evaluate the dynamics of ablation events. The heat transfer model incorporated intensity dependent absorption of the laser light by the electrons and predicted the thermal profiles within the electrons from the start of a laser pulse to 1 ps. The tight-binding molecular dynamics predicted the threshold electron temperatures (room temperature lattice) and overall equilibrium temperature (electron and lattice at the same temperature) required for changes in structure and ablation to occur in the material. The results of both simulations were then used to predict ablation threshold, ablation volume, and the size of the heat-affected zone within the material.

Ultrashort pulsed laser ablation experiments were performed on chemical vapor deposited and on single crystal diamonds, as well as on highly-oriented pyrolytic graphite, in order to verify the model predictions. Scanning electron microscopy, atomic force microscopy, profilometry, and micro-Raman spectroscopy were employed to characterize the ablated surfaces.

Results showed that ultrashort pulses, compared with nanosecond laser pulses, yield lower threshold fluences, higher material removal rates, and much more precise ablation, all of which are attributed to the increased absorption coefficient and improved energy coupling. The most significant observation is that the surfaces of diamond and graphite did not undergo phase transformation, demonstrating that chemical cleanliness is increased with use of ultrashort pulses rather than nanosecond or longer pulses. In addition, thermal damage and the associated debris and recast layer formation were virtually non-existent with ultrashort pulses. The investigation further showed that ultrashort pulsed lasers significantly reduced the feature size and improved the feature resolution, leading to sub-micron machining, which is not achievable in nanosecond or longer pulsed lasers. These experimental observations are consistent with predictions based on the finite difference and molecular dynamics models.

## CHAPTER 1. INTRODUCTION

The purpose of this body of research is to investigate the use of ultrashort ( $<10^{-12}$  sec.) pulsed lasers for micromachining of diamond and graphite phases of carbon. Diamond and graphite in numerous forms are extensively used in engineering. Diamond is of particular interest because of its extreme properties: It is the hardest substance known, it has the highest thermal conductivity, and its large band gap makes it transparent to light into the ultraviolet range. These properties make it useful in many applications, ranging from cutting tools to thermal spreaders for microelectronics, and is also being investigated for use as the most desirable material for MEMS devices. On the other hand, its drawbacks are its hardness, which makes mechanical forming processes uneconomical; its extremely high sublimation point (carbon has no stable liquid phase at normal pressures), which makes most thermal processes problematic; and its extreme optical band gap, which complicates conventional laser machining operations. Graphite, in contrast to diamond, is soft and an excellent lubricant. It is very useful for absorbing and catalyzing reactions. The carbon atoms in diamond are arranged as a tetrahedron, in which where each atom is bound to 4 others in a 3-dimensional network by extremely strong covalent bonds. In contrast, graphite consists of sheets of strongly bonded hexagonal rings, each sheet weakly bound to the next sheet.

This report of investigations of ultrashort pulsed laser ablation of carbon will have three sections: experimental investigations using the chirped pulse amplification (CPA) Ti:Sapphire laser at Lawrence Livermore National Laboratory, a finite difference computer model of the temperature gradients created in the electrons and lattice of irradiated carbon, and a molecular dynamics simulation of the atoms in the lattice modeling in which the atoms move when subjected to the excited electronic conditions generated by the laser beam. Additional

experimental data were obtained using an ultrashort pulsed excimer/dye laser at Laser Laboratorium in Germany and a similar unit at the University of Arkansas. The general findings of this work show that ultrashort pulsed laser ablation is superior to longer pulsed ablation in that it has significantly superior precision and repeatability, it yields a cleaner surface both chemically and physically after ablation, and heat affected zones are greatly reduced.

### ***Dissertation Organization and Contributions***

This chapter (Chapter 1. Introduction) states the goals of the research and summarizes the work that will be presented in later chapters.

Chapter 2. Background includes a generalized statement of the rationale for the research as well as important background information on why and how the work was performed.

Chapter 3. *A review of ultrashort pulsed laser ablation of materials*, a paper that was published in the Journal of Laser Applications, presents a review of literature pertinent to ultrashort pulsed lasers and their applications to materials processing. The author wrote this review paper with the assistance of his major professor, Dr. Molian. The specific contributions of this paper include:

- An up-to-date, complete state-of-the-art survey of information on ultrashort pulsed lasers and their applications to micromachining
- A reference guide for those already working in this field

*Chapter 4: Ultrashort pulsed laser ablation of diamond*, another paper published in the Journal of Laser Applications, reviews the literature on laser processing of diamond and presents results from ultrashort pulsed laser ablation of diamond, with analysis of advantages of the ultrashort pulsed process over the older longer pulsed laser ablative processes. The experimental work on ultrashort pulsed laser ablation in this section was performed by Dr. Malshe (coauthor of the paper) at Laser Laboratorium Goettingen in Germany and the Raman spectroscopy was

performed at The Penn State University. The bulk of the paper's analysis was the author's work. The specific contributions of this work are:

- A review of the current status of laser micromachining of diamond
- Evidence that ultraviolet femtosecond laser offers lower threshold, higher material removal rate, chemically clean surfaces, and absence of graphite formation, compared with ultraviolet nanosecond lasers.

Chapter 5. *Molecular dynamics modeling of ultrashort pulsed laser ablation of single crystal diamond* describes the results that the author presented at the International Conference on Applications of Lasers and Electro-Optics (ICALEO). It includes an initial first-order solution to the finite difference model, along with results from the tight-binding molecular dynamics simulation for the (111) diamond surface. The molecular dynamics simulations were performed by Cai-Zhuang Wang, a research scientist at Ames Laboratory with whom the author closely collaborated. The coauthors, Ozkan and Malshe, have contributed to some discussion. Their names appear as coauthors primarily because they are part of this NSF-sponsored research project.

Chapter 6. *Chirped pulse amplified Ti:Sapphire laser ablation of diamond: modeling and experimental verification*, a continuation of Chapter 5, presents an in-depth discussion of the finite-difference model, including the theoretical calculation of the electronic heat capacity and conductivity, all of which were developed and coded by the author, although Dr. Ho and Dr. Wang were both instrumental in development and improvement of the theoretical assumptions underlying this model. A simple solver was used to predict the temperatures of the electrons in a specific laser interaction volume with regard to absorbed energy, and a 1-dimensional finite-difference model was then used to predict the temperature profiles. Dr. Prusa was the faculty committee member who mentored the author by suggesting several different algorithms to solve the partial

differential equations and who helped debug initial instabilities within the numerical model. Dr. Wang contributed results from TBMD simulations for the (111) and (001) surfaces and bulk diamond. The paper also provides the results of CPA Ti:Sapphire laser ablation studies that the author performed at Lawrence-Livermore National Laboratory on CVD and single-crystal diamond. The sample characterization was performed by the author at Iowa State University, except for the SEM images obtained from the University of Arkansas and the Raman Spectroscopy data made available by The Penn State University. The author performed the bulk of the analysis in this chapter, including the finite-difference modeling and the atomic force microscopy characterization. The specific contributions of this paper are:

- Development of the electron temperature finite-difference model to predict the temperature distribution of the electrons.
- Capability to predict threshold and heat-affected zone size.
- Prediction of atomic motions that occur during ablation.
- Experimental verification of the model.

Chapter 7. *Femtosecond laser-induced periodic structure writing on diamond crystals and micro-clusters* is a paper written and published by collaborators from the University of Arkansas, Fayetteville, Arkansas. It is included here because it incorporates some of the experimental work the author performed at Lawrence-Livermore National Laboratory on CVD and single crystal diamond, and its discussion adds significant mechanistic understanding to the processes that occur in ultrashort pulsed laser ablation of diamond. The specific contributions of this work include:

- Utilization of periodic ripple structures in laser writing of specific shapes on diamond for device applications.

Chapter 8. *Ultrashort pulsed laser ablation of highly oriented pyrolytic graphite* is a paper that is to be submitted to the journal Carbon for publication. The author performed all the experimental work at Lawrence-Livermore National Laboratory, Iowa State University, and Ames Laboratory. The author received significant training in the use of the atomic force microscope from S. Wong, one of Marc Porter's graduate students. The only characterization that the author did not perform directly was the micro-Raman spectroscopy; it was performed at The Penn State University. The specific contributions of this paper include:

- Ablation phenomena of graphite under ultrashort pulsed laser conditions.
- Benefits and limitations of micromachining graphite using lasers.

Chapter 9. General conclusions draws the significant conclusions from the findings in the papers, and Chapter 10. Future work recommends additional work that could produce an improved understanding of the effects of ultrashort pulsed laser ablation.

There are three appendices. Appendix A. Ultrashort pulsed titanium sapphire laser system discusses theoretical and practical information on operation of chirped-pulse amplified Ti:Sapphire laser systems. It also presents some basic theory on micromachining and beam characterization.

Appendix B: finite-difference model covers the theory and code that was used to perform the calculations in the papers included in this dissertation. It also discusses the theoretical calculation of the relevant electronic properties needed for these simulations.

Appendix C: tight-binding molecular dynamics discusses the molecular dynamics simulations used in this work. It specifically covers the theory of the interatomic potential, the boundary conditions used, and the overall simulation method.

## CHAPTER 2. BACKGROUND

The growth of lasers in manufacturing is rapidly expanding, because lasers can perform tasks faster, cheaper, and better than competitive technologies. Lasers have been used for numerous applications, from cutting ½-inch-thick plate steel to drilling sub-micron holes in the manufacture of millipore filters. The choice of a laser and goal of a process are of primary importance in achieving specific results.

Lasers have significant advantages over many other technologies. They are versatile tools that can be used for many different purposes, merely by, for example, changing optics. CO<sub>2</sub> lasers that operate in continuous wave mode at several kilowatts can be used for a myriad of tasks, including cutting, drilling, welding, and heat treatment. Nd:YAG lasers can be used for welding, hole drilling, and marking operations. Lasers also have the ability to perform tasks that traditional mechanical tools cannot do: They can drill holes in very hard materials without wearing out expensive tools, drilling can be performed at almost any angle into a surface, complex shapes can be formed on a surface through use of mask image projection techniques, and very small features can be created on microelectronic devices without contamination from chemicals or abrasive residues.

For a given job to be performed optimally, a laser is usually chosen on the basis of the following criteria: power, pulse width, beam quality, and wavelength. As technology advances, the limits for each of the criteria continue to expand: Average and peak power continue to grow, beam quality continues to improve, and wavelengths continue to decrease.

The power of a laser is of extreme importance. In large-scale manufacturing (e.g., automobile production) in which steels are cut and welded, a laser with multikilowatts of power is required to achieve acceptable results. Simple hole drilling and spot welding require less

energy, usually around several hundred watts, while even less power is required for small jobs such as micromachining. We refer to two types of power when discussing lasers: average power and peak power. Average power is easily understood; it is a measure of how much power a laser can deliver over large time-frames. Peak power is the term used in discussing pulsed lasers; it is the amount of power delivered during a single pulse of laser energy divided by the pulse width. For continuous wave lasers, the average and peak powers are the same.

Pulse width strongly affects a laser's peak power, which is defined by the following equation:

$$\text{Peak Power} = \text{Pulse Energy} / \text{Pulse Width} \quad (1)$$

Pulse widths vary from milliseconds in free-running, arc lamp pulsed Nd:YAG lasers to less than 10 femtoseconds in advanced lasers. For most common pulsed lasers, the pulse widths vary from around 20-ns to 20-mS, although shorter pulse width lasers are becoming more common; Nd:YAG lasers with pulse widths of a few picoseconds are now readily available.

Consequently, peak powers can reach trillions of watts.

The predominant lasers currently used in industry have pulse widths that vary from around 20-ns to continuous wave. Pulse width is very important, as it defines the time during which light interacts with the material. Long interaction times (millisecond pulsed and continuous wave lasers) are usually associated with lower intensity lasers that are useful for heat treatment, welding, or drilling/cutting by melt ejection and reactive (e.g., oxygen-assisted cutting) mechanisms. With increased need to remove material by vaporization, the intensity goes up, which necessitates the use of shorter pulse widths. This is the case for smaller scale processes (e.g., drilling through-holes on chips made from silicon wafers, marking applications) and for high precision laser machining (e.g., manufacture of micro-electromechanical systems, or MEMS). Pulse width and pulse energy are the key factors contributing to the peak power of the

laser. Other factors in achieving very high intensity including beam shape, beam size, energy distribution, and beam divergence. Figure 1 shows a plot of peak intensity and interaction time, with specific applications marked.

The quality of the beam is one factor that limits how small a spot the beam can be focused to. The most desirable beam for achieving high intensity is the perfectly circular Gaussian profile beam. The smaller the diameter and divergence of the beam, the smaller the spot size. The other factor that limits the spot size is the wavelength of the beam. The shorter the wavelength, the more easily the beam is focused to a small spot size. The ideal Gaussian beam can theoretically be focused to a spot with the same diameter as the wavelength. This limit is not attainable because truly Gaussian beams do not exist, and aberrations in the optics do not allow it. The spot size along with power determines intensity, which is defined as follows:

$$\text{Intensity} = \text{peak power} / \text{spot area} \quad (2)$$

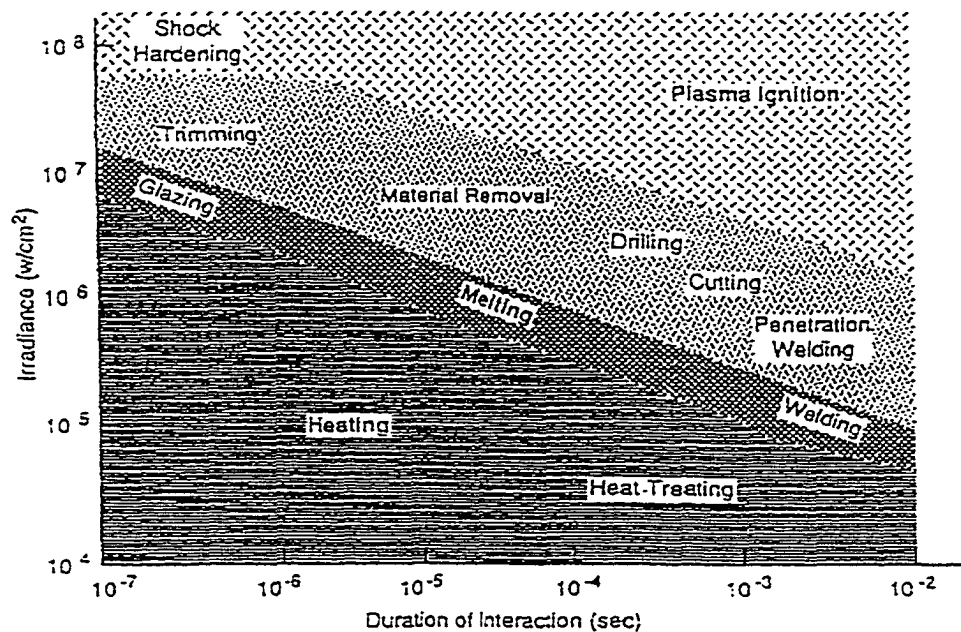


Figure 1. Intensity in Watts/cm<sup>2</sup> with pertinent applications marked<sup>1</sup>

The spot area is determined by assuming a Gaussian energy distribution and using the  $1/e^2$  value of the beam dimension. Because the spots are usually circular, the peak intensity is quadrupled if the diameter of the spot is halved. Peak intensity and the laser's wavelength control the kind of interactions the laser energy will have with a material. If a material is transparent to a wavelength of light at low intensity (normal viewing illumination), very intense light will be required to cause optical damage and absorption of the light. High intensities are also needed for highly reflective materials, such as copper and aluminum.

The factors in the laser that determine the power, wavelength, pulse width, and beam quality are the resonator cavity, the laser medium, and the optical pumping mechanisms. The types of laser of greatest importance to industry and materials processing are solid-state lasers and gas lasers; several other kinds of laser that use laser mediums such as dye in a liquid medium are not commonly used except in research and in very specialized industrial applications.

The most common gas laser is the  $\text{CO}_2$  laser, which operates at  $10.6 \mu\text{m}$  wavelength and is pumped by use of electrical discharge. It is usually run in continuous wave (CW) mode and has power outputs that range from a few watts to tens of kilowatts. It also has a large range of beam profiles; the lower power lasers tend to be very close to round Gaussian beams, whereas the higher power lasers utilize laser resonator cavities that optimize power output instead of beam quality. Stable cavities have better beam quality, while unstable cavities make better use of the amplification medium for improved peak power. Figure 2 shows a comparison between stable and unstable resonator cavities.

The most common solid state laser in industry is the Nd:YAG laser, which operates at  $1.06 \mu\text{m}$  (or  $532 \mu\text{m}$  if frequency-doubling crystals are used) and which is optically pumped with flash

lamps, arc lamps, or diode lasers. Diode laser pumping, relatively new on the market, has greatly improved the Nd:YAG laser by reducing its size and significantly improving its power efficiency and beam quality. However, Nd:YAG lasers rarely attain Gaussian beams, because of the optical properties of the Nd:YAG rod. Because Nd:YAG lasers can be operated in continuous wave mode, free running pulsed mode, or Q-switched mode, pulse widths can vary from approximately 10 picoseconds up to continuous wave.

Lasers that operate in the ultraviolet range are widely used in applications such as micromachining and laser marking. The most common of these are the excimer lasers, which use a mixture of noble gases and chlorine or fluorine gas and are also pumped by use of electrical discharge. The most common wavelengths are 308 nm, 248 nm, and 193 nm. The gas mixtures used to achieve these wavelengths are xenon and chlorine, krypton and fluorine, and argon and fluorine, respectively. The pulse widths of these lasers range from around 1 ns to 30 ns, and the energy output ranges from a few  $\mu\text{J}$  to 500 mJ per pulse. The beam profile of

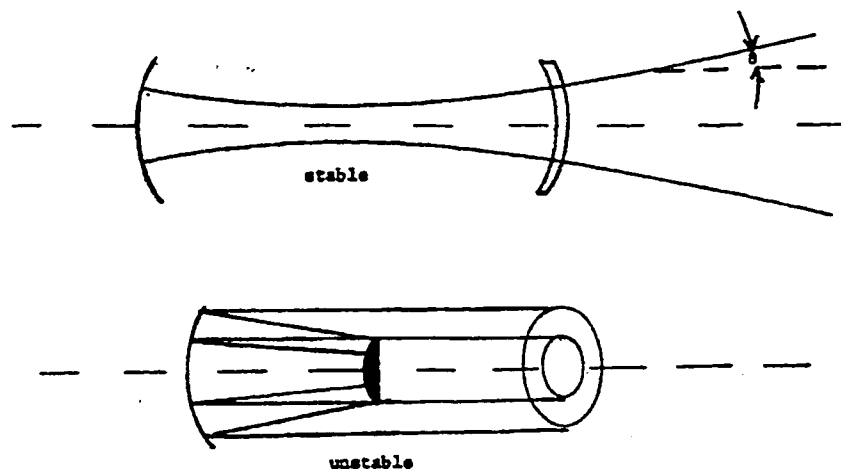


Figure 2. A comparison of a stable and an unstable laser cavity (resonator) <sup>2</sup>

most excimer lasers is rectangular; in the long axis the beam profile is top-hat shaped, in the short axis it is Gaussian. This limits the achievement of small spot sizes. Figure 3 illustrates an excimer laser profile. The ultraviolet light offers two significant advantages. The first is the short wavelength; recall that wavelength is a limiting factor for focusing to a small spot. The second is the high photon energy of ultraviolet light. Materials that are transparent to visible and near infrared light are often strongly absorbing in the ultraviolet range, so that the pulse energy required for material ablation is greatly reduced. These lasers are also often referred to as cold lasers; they tend to cause vaporization rather than melting and boiling of the ablated material, and this property also improves their precision. Although there is still an area of collateral thermal damage around the ablated region.

A new class of lasers with ultrashort pulses has been developed recently. These lasers are capable of generating pulses much shorter than one picosecond ( $10^{-12}$  s). This is very important, because short pulses can perform precise tasks such as micromachining effectively. Individual pulse energies for these lasers are usually small, 1-20 mJ, but intensities are extremely large because of the short pulse widths, usually in the range of giga- ( $10^9$ ) to tera- ( $10^{12}$ ) watts per square

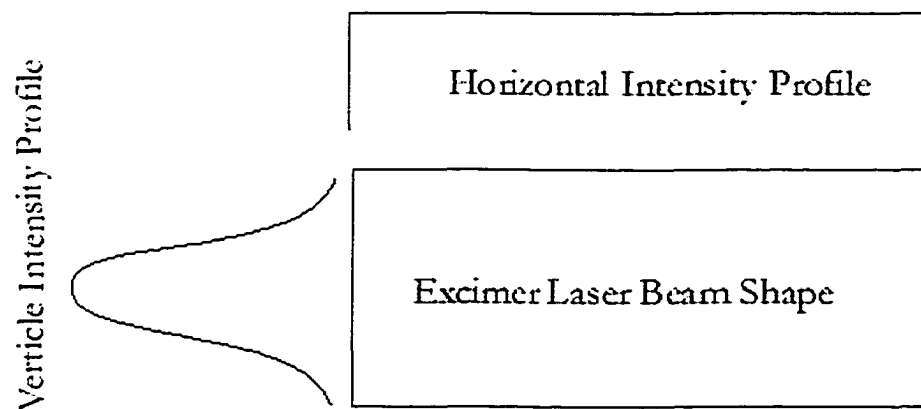


Figure 3. Beam profile of a typical excimer beam

centimeter. (The intensity of sunlight hitting the earth is approximately  $0.1 \text{ W/cm}^2$ , as a number for comparison.) The way materials react to this extreme intensity is fundamentally different from the way they react to lower intensities. The materials undergo processes such as multi-photon absorption and electron avalanche excitation, making them highly absorbing, independent of the wavelength. In addition, the interaction time of the energy with the material is so short that the thermal diffusion distance into the material is much shorter than the optical skin depth, which improves energy coupling and greatly reduces undesirable collateral thermal effects. This property makes it easier to predict the effects of ultrashort pulses, and increases the precision these lasers can attain. These lasers which will likely be the enabling technology for micromachining and manufacture of extremely small structures such as MEMS, are also capable of drilling deep, high-aspect-ratio holes that are useful in single crystal superalloys as cooling holes on jet engine turbine blades.

Micromachining is a frontier technology for advancing the miniaturization of devices and structures. Structural, electro-mechanical, and microelectronic devices that need very small parts (e.g., arterial stents, gears, levers) and physical features (e.g., small holes and grooves) will be necessary for advances in fields such as the aerospace, automotive, and medical areas. These very small-featured devices will be machined of many materials, the most likely being ceramics such as diamond, boron nitride, silicon, and alumina. Medical devices such as stents, which are minute cylindrical supports used inside arteries, ureters, and similar structures, will be machined out of metals (titanium and stainless steel) and biopolymers.

Micromachining uses different kinds of laser beam delivery optics. The first configuration is mask projection, a method in which a mask is made using either plastic or metal depending on the laser wavelength. This piece is placed in the unfocused beam path and then imaged onto the surface of the work piece with a lens or system of lenses. Figure 4 shows a typical optical

configuration for mask projection machining. Complex shapes can be created using this method, which is also the method used for laser marking. Direct etching can also be accomplished, by using a focused beam and micropositioners to raster the part or beam to create the structures. As feature sizes decrease, tools that can visualize very small structures will be required; atomic force microscopy (AFM) and scanning electron microscopy (SEM) are examples of such technology.

### References

1. J. F. Ready, "Absorption of Laser Energy," *Guide to Laser Materials Processing* (CRC Press, Boca Raton 1993), p.93.
2. J. T. Lyuxon, "Laser Optics/Beam Characteristics," *Guide to Laser Materials Processing* (CRC Press, Boca Raton 1993), p.57.

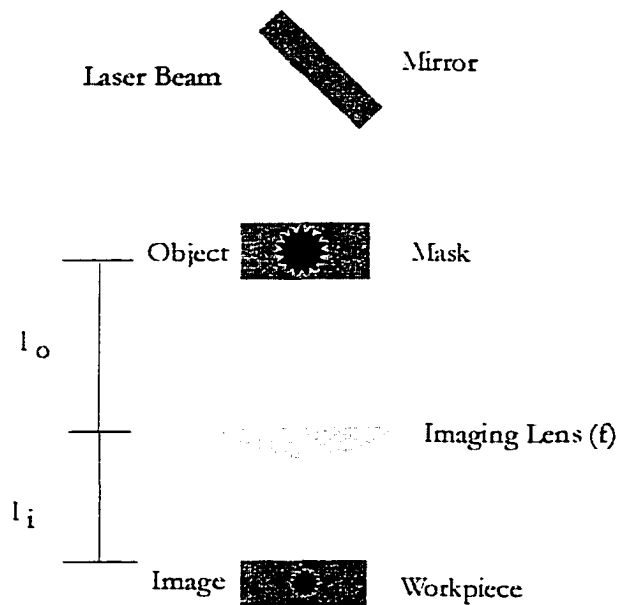


Figure 4. Diagram of an image projection machining setup

## CHAPTER 3. A REVIEW OF ULTRASHORT PULSED LASER ABLATION OF MATERIALS

A paper published in the Journal of Laser Applications (1998)<sup>a</sup>

M. D. Shirk and P. A. Molian

### *Abstract*

The use of ultrashort pulsed lasers in materials processing is an emerging technology. These lasers have the capability to ablate materials precisely with little or no collateral damage, even with materials that are impervious to laser energy from conventional pulsed lasers. The extreme intensities and short timescale at which ultrashort pulsed lasers operate differentiate them from other lasers. The means of ultrashort pulsed laser generation is discussed; included are a survey of pulse compressor techniques with solid state lasers and a brief discussion of excimer-dye lasers. This is followed by a discussion of specific examples of ultrashort pulsed machining of specific materials, along with mechanistic details. Optical breakdown mechanisms, including electron avalanche ionization and multiphoton absorption are discussed. It is shown that as pulse width increases and intensity decreases, laser damage becomes a stochastic process in which the ultrashort pulsed, high intensity light causes optical breakdown over a very narrow range. This, along with the lack of significant thermal conduction, greatly improves the precision of ultrashort pulsed lasers in micromachining applications.

### *Introduction*

Progress in the field of laser materials processing relies on the development of innovative laser systems. Recently laser systems of a new class of ultrashort pulsed, high intensity lasers

---

<sup>a</sup>. Journal of Laser Applications 10:1 (1998) p. 18-28, published by Laser Institute of America

have appeared and are being used to investigate laser materials processing phenomena and applications. Two laser systems of interest are the Ti:sapphire (735 nm to 1053 nm) and excimer-dye (220 nm to 300 nm, 380 nm to 760 nm) laser configurations. With the advent of chirped pulse amplification (CPA) and pulse compressor techniques, these lasers offer pulse widths in the femtosecond range and pulse energies up to 125 mJ for Ti:sapphire and 15 mJ for excimer-dye laser configuration. The maximum focused intensities are currently around  $10^{19}$  W/cm<sup>2</sup>.<sup>1</sup> Potential applications of these lasers in manufacturing include micromachining and pulsed laser ablation for deposition of thin films. Understanding the beam-material interaction phenomena on a molecular level rather than on a macro heat transfer scale would allow evaluation of the potential of femtosecond lasers for new laser materials processing applications. Some general characteristics of material interaction with subpicosecond laser pulses include reduction or elimination of lateral thermal damage, lower and more precise threshold fluences of ablation, and reduced material redeposition. These effects result from the extreme intensities and short time-scales of these pulses compared with the timescale of photon-electron-lattice interactions.

### *Types and capabilities of ultrashort pulsed lasers*

Ultrashort pulsed lasers are quite complex in design and generally exhibit low average power levels. For a laser to exhibit high intensity, ultrashort pulses, the following conditions are necessary:

- (1) The laser medium must have a broad spectral bandwidth. A well known example is Nd:Glass.
- (2) The laser should be mode-lockable by active or passive techniques.
- (3) The pulse spreading due to the gain in the active medium, and optical dispersion of the components, should be eliminated.

- (4) A method should be used that amplifies the laser energy without damage to the optics as a result of high intensity.

Various sub-picosecond pulsed lasers are being researched currently. The successful laser media for generating ultrashort pulses include Ti:sapphire, Nd:glass, Yb:YAG, Yb:glass, alexandrite, and dyes. The two that have been investigated most widely for materials processing are the excimer-dye combination and the CPA Ti:sapphire sapphire. Table 1 shows a sample of current laser systems that produce sub-picosecond pulses. A wide variety of pulse lengths and pulse energies are available. It should be noted that the maximum power may not be available at the shortest pulse length listed in the table; the figures listed are presented to show the limits of maximum pulse energy and minimum pulse widths each system can produce. The Ti:Sapphire systems may also be tunable within a range of near infrared (NIR) wavelengths close to those listed.

The CPA process has been applied to lasers since 1985, when Strickland and Mourou<sup>2</sup> used a CW mode-locked Nd:YAG with a Nd:glass amplifier to generate 2 ps, 1 mJ level pulses. This system used single mode fiber to dispersively stretch the seed pulses by use of a combination of group velocity dispersion and self-phase modulation. This induced a positive dispersive delay line. A double grating compressor was then used to induce a negative dispersive delay line, thereby shortening the pulse. The pulse must be stretched so that it can be safely amplified

Table 1. Several examples of current sub-picosecond lasers

Reference	Type	Wavelength	Pulse width	Rep rate	Pulse Energy
2	Ti:sapphire	780-nm	20-fs	10 Hz	100 mJ
3	Ti:Sapphire	780-nm	18-fs	50 Hz	80 mJ
4	Excimer:dy	248-nm	500-fs	-	10 mJ
5	Ti:Sapphire	1053-nm	270-fs	1 kHz	60 mJ
6	Excimer:dy	248-nm	300-fs	1 Hz	-

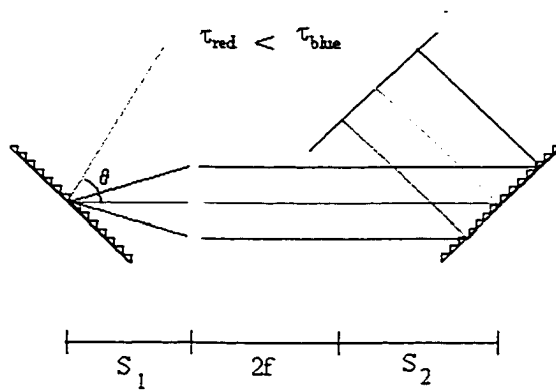
without optical degradation occurring in the amplifier material. If the frequency elements of the pulse are distributed over time, the overall intensity, which is reduced during amplification, can then be regained through use of the compressor which effectively reverses the stretching of the pulse. Since the work of Strickland and Mourou, CPA has been used successfully to create ultrashort pulses in many mediums.

Barty<sup>3</sup> describes the most common process very simply as follows: a mode-locked laser, or other oscillator capable of producing ultrashort pulses, is used to create a low intensity, broadband seed pulse. This pulse is then dispersively stretched using a 2 grating expander [Figure 1(a)], to induce the positive group delay. This means that the time required to go through the expander is shorter for red (longer wavelength) light than for blue (shorter wavelength) light because of the difference in optical path length, which broadens the pulse width by spreading the frequency distribution of the pulse spatially. This broadened pulse is then amplified in a broadband regenerative amplifier. The amplified pulse is then passed through the compressor [Figure 1(b)], which adds a negative group delay line, such that blue (shorter wavelength) light takes less time to pass than red light, thereby reconstructing the initial pulse if the proper conditions are met. This assumes that the incident angles on the initial gratings are the same ( $\theta_{\text{exp.}} = \theta_{\text{comp.}}$ ) and that the following condition is met:

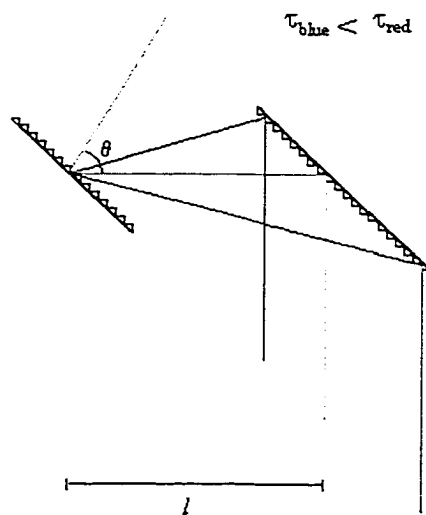
$$l = 2 f - S_1 - S_2 \quad (1)$$

so that the optical path length differences of any wavelength of light is the same after it has been through both the expander and compressor, so that the initial pulse shape is recreated.

In CPA solid state lasers (Fig. 2), the light is introduced into the regenerative amplifier by passing it through a vertical polarizer and a prism. The light is then passed through a Pockels



(a)



(b)

Figure 1. (a) The positive group delay dispersion expander stretches pulses by making the path length longer for shorter (blue) wavelengths than for longer (red) wavelengths, distributing the various wavelengths over time. (b) The negative group delay dispersion compressor acts to regenerate the initial pulse profile by making the optical path longer for longer (red) wavelengths than shorter (blue) wavelengths.

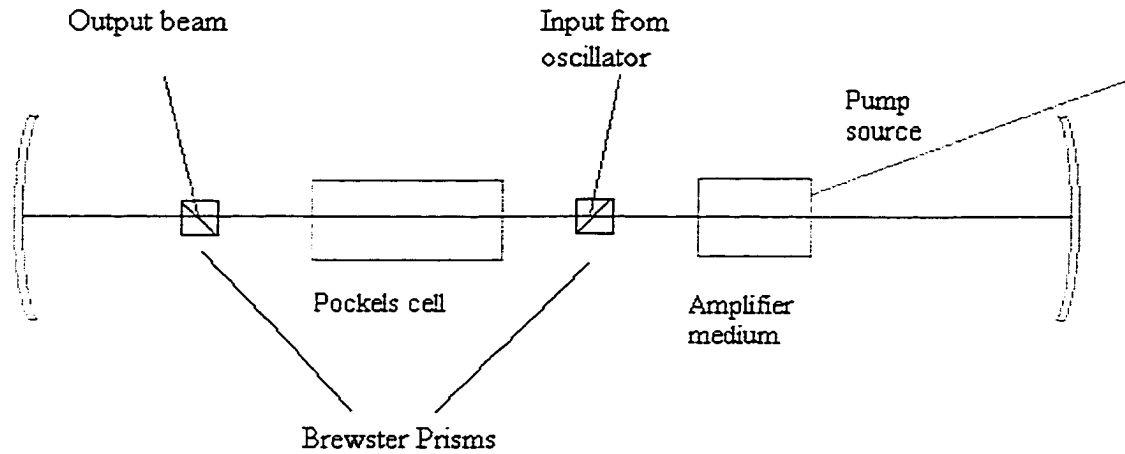


Figure. 2 A solid state regenerative amplifier, the seed pulse (vertical polarized) is injected into the system at the input Brewster prism. It is then passed through the amplifier until the voltage is removed from the Q switch, thereby letting the amplified pulse reflect out the output Brewster prism.

cell, and then through the output prism; reflected off a mirror; repassed through the prism and Pockels cell through the input prism and then through the amplifier medium; reflected off a mirror; and finally passed back through the amplification medium. The light is amplified with each of these passes. The voltage on the Pockels cell is then removed, allowing light to exit through the output prism. Thus the Ti:sapphire uses a pair of prisms to circumvent the dispersion effects and a pair of gratings (chirped pulser) to amplify the light energy without damaging the internal optics. It should be noted that this laser has additional electro-optical elements. The shortest pulse obtainable with it is 6-fs.

Szatmari et al.<sup>4</sup> described the generation of subpicosecond pulses using an excimer-dye laser. Figure 3 is a schematic of an excimer-dye laser from Laser Laboratorium Gottingen, Germany. The principle underlying the generation of ultrashort pulses by use of a distributed feedback dye laser (DFDL) is that an excimer laser is used to pump a quenched (short-pulse) dye laser that

emits at 340-nm at 200-ps, which is then used to pump the distributed feedback dye cell through passage of the output beam through a cylindrical telescope and then through a transmission grating. The interference pattern from the grating is imaged into the distributed feedback dye cell by use of a microscope objective. One important aspect of this system is that a block is placed so that the zeroth order (center bar) of the diffraction pattern is blocked. The resulting excitation in the dye produces both population inversion and refractive index changes periodically in the dye. The wavelength is tunable by changing the distance of the objective and the diffractive grating, along with selecting the appropriate dye for the predicted wavelength of interest. The output wavelength is determined by the spacing of the diffraction pattern imaged into the pump cell. The output from this cell is then passed through a dye amplifier to raise the output from the  $\mu\text{J}$ -level to the mJ-level. The output was tunable over the visible spectrum with 500-fs pulses, which are potentially compressible to 300-fs.

There are several ongoing efforts to create laser systems with shorter, more intense pulses. Researchers are working at Stanford and the University of California, San Diego on CPA Ti:Sapphire lasers to create pulses with petawatt intensities<sup>5</sup>. Problems that must be fully overcome include compensating for a dispersion induced by the optical material within the laser system and its amplifiers<sup>6</sup> and gain narrowing within the amplification medium.<sup>7</sup>

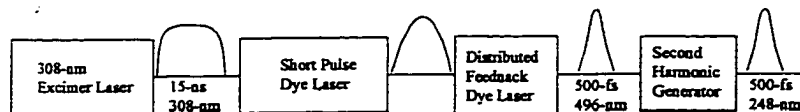


Figure 3. A simplified schematic of an excimer-dye laser, the excimer laser pumps a short pulsed dye laser, which is then passed through a grating and imaged into the DFDL cell, creating a periodic grating of both refractive and population inverted dye. The output from the DFDL cell is then compressed to 300-500 fs. This output can then be passed through a second harmonic generator to create UV pulses.

### **Dispersion induced by optical materials**

Materials-induced dispersion causes pulse broadening in ultrashort pulses. This occurs because current lasers dispersively stretch a short (10-20-fs) seed pulse, usually broadening it to several tens of picoseconds to amplify it without creating intensities that would cause optical breakdown in the amplification medium. The pulse is then recompressed after the amplification to regain the original pulsewidth. Errors induced in the stretcher, amplifier, and compressor optics have been the limiting factors in preventing these systems from regenerating these pulses perfectly. One source of error is dispersion induced in refractive optical materials, which is a wavelength-dependent phenomenon. To overcome and/or compensate for material-induced dispersion, Lemoff et al.<sup>6</sup> and Stingl et al.<sup>8</sup> have designed reflective optics-based systems to avoid and compensate for dispersion induced by the transparent optical materials, such as the Brewster prisms, and amplification medium. The two groups approached the problem differently. The main points of the papers by Lemoff et al. are the choice of prism materials and design of the optical system that uses ray-tracing analysis to eliminate dispersive problems. Stingl et al. used specially designed chirped multilayer dielectric mirrors to induce negative group delay dispersion across a very broad bandwidth, which helps compensate for many dispersive problems and which has allowed for creating systems with <10-fs broadband pulses.

### **Gain narrowing**

The gain cross section of Ti:sapphire and other amplifier materials is an important consideration. Because some wavelengths are amplified more efficiently than others, a shift occurs in the bandwidth of the pulse, leading to distortion of the pulse as it is recompressed, and resulting pulse broadening. Barty et al.<sup>7</sup> discussed the requirements of a laser system to achieve 100 TW peak energy, 15-fs pulses at a 10 Hz repetition rate. One main design point presented is that, even though Ti:Sapphire is a broadband amplification medium, it is most efficient just

below 800-nm in wavelength; therefore, whatever the frequency spectrum of the incoming pulse, it is shifted so that its maximum is closer to 780-nm. A filter placed within the amplification cavity can partially attenuate the signal in the ranges of the gain medium's maximum gain, thereby flattening the gain spectrum over a broad range of frequencies to preserve spectral bandwidth. This reduces amplifier efficiency, so that more passes are required to obtain a given amplification. This is not a significant problem, because the system was designed to compensate for greater dispersion associated with the optical material's greater path length, which is induced by the additional number of passes through the amplifier. This compensation enables the compressor to recreate a pulse within 5% of the initial seed pulse width, but strongly amplified. It should be noted that with the generation of such short pulses, reflective optics must be used for beam delivery in order to prevent materials-induced dispersion.

Ultrashort pulses offer many advantages. These include precise ablation of materials without significant heat affected zones (HAZ), ablation of large band-gap materials including insulating ceramics<sup>9</sup> and fluoropolymers,<sup>10</sup> ablation of high reflectivity materials,<sup>11</sup> smaller and more precise fluences for ablation, avoidance of plasma absorption effects, and low amounts of redeposition.<sup>12</sup> These effects lead to cleaner, more precise micromachining processes.

#### *The state of the art of ultrashort pulsed laser materials processing*

A few publications in the literature address the effects of ultrashort pulsed lasers used in materials processing. Most of these works deal with experimental observations; there has been little effort to explain the fundamental phenomena associated with such short pulses. The effects of ultrashort pulses are summarized below for each class of materials.

## Metals

Chichkov et al.<sup>11</sup> investigated hole drilling of metals with a commercial Ti:sapphire laser with repetition rate 10 Hz, pulse width 0.2 to 5000 ps and pulse energy up to 100 mJ. The image projection method was used to obtain a spot size of 0.17 mm. Laser hole drilling experiments were carried out in a vacuum chamber ( $10^{-4}$  mbar) on 100  $\mu\text{m}$  steel and copper foils at energy fluences from 0.1 to 5 J/cm<sup>2</sup>. For steel, after  $10^4$  pulses (laser parameters of 200-fs, 120  $\mu\text{J}$ , 0.5 J/cm<sup>2</sup>), there was no evidence of molten material around the hole. In contrast, the pico (80 ps, 900  $\mu\text{J}$ , 3.7 J/cm<sup>2</sup>) and the nano (3.3 -ns, 1 mJ, 4.2 J/cm<sup>2</sup>) second pulsed lasers resulted in formation of a molten phase, which leads to an unstable drilling process. This "instability" is more severe with nanosecond pulses. In summary, the energy fluence required for hole drilling increases with increased pulse width from the femtosecond range to the nanosecond range, and the hole quality improved with shorter pulse widths and lower fluences (close to ablation threshold).

In a second experiment, a second harmonic Ti:sapphire laser at 390-nm wavelength (250 fs, 0.5 mJ, 2.5 J/cm<sup>2</sup>) was used to drill holes in 0.5 mm thick steel sheet and 1 mm copper sheet. The hole characteristics, investigated as a function of the number of pulses, showed that the plane evaporation front was unstable. This instability was attributed to diffraction effects and variation of the quality of the laser beam. There was no evidence of a molten phase. This study did not compare ablation behavior in copper and in steel. However, it can be inferred from the data that thermal properties of the substrate play minor roles in the ablation of metals at femtosecond pulse width.

Chichkov et al.<sup>11</sup> concluded that femtosecond machining of metals rapidly creates vapor and plasma phases with negligible heat conduction to the bulk and with no liquid phase. In addition,

reproducibility of data is better with femtosecond machining because the hole drilling process is stable and no liquid phase is present.

Preuss et al.<sup>13</sup> reported laser ablation of metals, including Ni, Cu, Mo, In, W, and Au, by use of 500-fs, 248-nm wavelength laser pulses. Table 2 summarizes the results. Threshold fluences are listed, along with a depth-per-pulse comparison at 300 mJ per cm<sup>2</sup>.

Ablation rates were also studied for both nickel and indium in air. In each case, the ablation threshold was not affected by the environment, but the ablation rate/redeposition rate was strongly affected by ambient atmosphere. For both metals, the ablation rate decreased by a factor of 2-3 as the pressure increased from 10<sup>-8</sup> bar to 1 bar. Also, as pressure increased, the redeposition rate increased, as evidenced by additional material detected around the ablated hole by stylus profilometer measurements and optical microscopy. The data were compared to a rather simple ablation model which uses the reflectivity, absorptive coefficient ( $\alpha$ ), and incident intensity to predict ablation fluence thresholds. It was assumed that the ablation threshold is reached when the volume energy density, as calculated from the above variables, was equal to the evaporation enthalpy at 298 K. Molybdenum showed an excellent fit, whereas data for the most of the others were judged to be good approximations. The exception was indium, for

Table 2. Typical data in vacuum; depth per pulse is for 0.3 J/cm<sup>2</sup><sup>a</sup>.

Metal	Threshold fluence	Depth per pulse
Ni	0.1 J/cm <sup>2</sup>	15-nm
In	0.125 J/cm <sup>2</sup>	90-nm
Cu	0.175 J/cm <sup>2</sup>	8-nm
Mo	0.15 J/cm <sup>2</sup>	6-nm
Au	0.21 J/cm <sup>2</sup>	17-nm

<sup>a</sup>Source: see reference<sup>†</sup>.

which the model failed. This model would not work for longer pulses because thermal conduction away from the ablation site would then need to be taken into account.

It has been shown that ablation of areas that are smaller than the laser's spot size may be possible.<sup>12</sup> An 800-nm Ti:sapphire laser was used so that the center of the Gaussian shaped pulse was just above the threshold fluence for ablation. The spot size was on the order of 3  $\mu\text{m}$ , whereas the diameter of the pit generated was 300 nm. The pit depth was only 52 nm however. This indicates that large effects of thermal diffusion have been eliminated. A comparison using a similar nanosecond pulsed laser showed that the minimum ablation area achievable was about 60 % of the laser's spot size, or 6 times as large as the area achieved with the femtosecond pulsed laser. The morphology of the hole, as determined by atomic force microscopy, indicated that a molten pool had been formed and that material had flowed, in contrast to the apparently clean ablation achieved with the ultrashort pulsed laser.

Stuart et al.<sup>14</sup> reported that high aspect ratio holes can be produced in metals without a heat affected zone by a 1054-nm, 350-fs pulsed laser. In addition, slots of various geometry can be cut into the stainless steels by varying the spatial profiles of the beam. Liu et al.<sup>15</sup> compared hole drilling in superalloys such as Inconel and MA 956 with 350-ps and 100-fs pulses of a Ti:sapphire laser system. The holes produced by the 350-ps laser contained a recast layer, approximately 40  $\mu\text{m}$  thick, on the walls, whereas no layer was present in the holes produced by the 100-fs laser. Also, the 350-ps pulses induced microcracks, none of which were found in the samples processed with the 100-fs pulses.

In summary, ultrashort pulses for metal ablation offer two primary benefits:

- (1) Plasma formation does not occur during the pulse.
- (2) Heat diffusion into the metal is insignificant during the pulse's timescale.

These benefits lead to two effects on the material removal rate (MRR):

- (1) Compared with long pulsed lasers, the ultrashort pulsed lasers provide a MRR that is less dependent on the spot size.
- (2) The threshold fluence for ablation is both smaller and more precise for ultrashort pulsed lasers.

One group has suggested that there are limits to these claims.<sup>16</sup> At fluences far above the threshold for ablation, thermal effects are observed, including the presence of material that has melted and undergone viscous flow. Pressure effects resulting from high ablation and plasma pressures were also observed. A comparison of various pulse widths was conducted, using three different lasers: a copper vapor laser, a mode-coupled Nd:YLF, and a CPA Ti:sapphire laser. Unwanted thermal effects were found in all cases in which deep holes were produced by use of very high fluences. At  $700 \text{ J/cm}^2$ , a comparison of the copper vapor laser (50 ns) and the Ti:sapphire laser (200 fs) showed that the shorter-pulse-length laser would drill through a 1 mm thick copper sheet in 145 pulses, whereas the copper vapor laser required 290 pulses. Thus both lasers ablated a few micrometers per pulse, even though the Ti:sapphire's intensity was five orders of magnitude greater. The samples used were cold rolled, to the point that their recrystallization temperatures were quite low, so that any thermal effects could be detected. Both lasers created heat affected zones of a few microns in size, as determined by scanning electron microscopy (SEM). Analysis of hole cross sections also show that redeposition of material was higher up in the hole for the femtosecond laser than the nanosecond laser,  $250 \mu\text{m}$  for the copper vapor, and  $400 \mu\text{m}$  for the Ti:sapphire. It was also observed that, regardless of laser type, the heat affected zone was larger at the top of the hole than at the bottom. The heat affected zone at the top was attributed to the interaction of the substrate with the plasma, vapor,

melt, and redeposited material that transferred heat to the sides of the holes, rather than to thermal diffusion.

Other observations on the effects of ultrashort pulsed laser material processing include the following: The ablation threshold is not affected by the air or vacuum environment, but ablation in air yields a lower ablation rate than in vacuum. Redeposition of material occurs in air, but is virtually absent when ablation is performed under a vacuum. The explanation is that in a vacuum, the ejected material can expand freely, whereas in air, the ejected material interacts with gaseous molecules, leading to significant redeposition of the material.

It is apparent that as long as extremely high fluences are avoided and deep, narrow holes are not drilled, ultrashort pulsed ablation in metals can be modeled using the classical photoablation equation, in which  $D$  is the depth ablated per pulse,  $\alpha$  is the absorption coefficient,  $E$  is the actual fluence and  $E_t$  is the threshold fluence:

$$D = 1/\alpha \ln (E/E_t) \quad (2)$$

provided the following are satisfied: (1) Absorption follows the Beer-Lambert law, (2) reflectivity is constant, (3) ablation takes place after the pulse is over, (4) heat conduction is negligible, (5) redeposition does not occur.

This equation is not valid for metals ablated using pulses of nanosecond duration because the thermal diffusion distance is two orders of magnitude over the optical penetration distance making assumption (4) meaningless.<sup>13</sup>

The ablation of metals has always been noted to be different from the ablation of semiconductors and insulators at moderate fluences. This difference is due to the transition from linear absorption processes to nonlinear processes, including multiphoton absorption. Two classes of materials that exhibit this behavior; polymers and ceramics have been investigated.

Polymers are very different from metals in that they are held together by weak bonds, van der Waals, dipole-dipole, and hydrogen bonds. Ceramics, on the other hand, are held together by strong covalent and ionic chemical bonds. Subpicosecond ablation of these materials will be discussed below and compared to the ablation of metals.

### Polymers

Kuper et al.<sup>10</sup> investigated the ablation of polytetrafluoroethylene (PTFE) with pulsed 248-nm laser pulses. Attempts at ablation of PTFE with nanosecond pulsed excimer (248-nm, 16-ns, 2 J/cm<sup>2</sup>) lasers led to a chemically degraded and disrupted surface after 50 pulses. To improve these outcomes, shorter but more intense pulses were used. In a different experiment, 300-fs, 1 J/cm<sup>2</sup> pulses smoothly ablated PTFE and the edges of the ablation showed little or no evidence of thermal damage.

The experiment used 4-mm thick commercial Teflon sheets ( $\alpha_{248}=158 \text{ cm}^{-1}$ , density = 2.15 g/cm<sup>3</sup>) that had been polished and cleaned with methanol. Multiple holes were ablated, with a range of fluences and numbers of pulses at 248 nm and 300 fs. The repetition rate was set at 1 Hz to avoid any concerns about residual thermal effects. A stylus profilometer was used to determine hole depths; then the depth per pulse was determined using a linear regression from a plot of the number of pulses versus hole depth. In other polymeric materials, such as polymethylmethacrylate, it has been shown that ablation is possible with lower intensity nanosecond pulsed lasers because chemical changes occur in the polymer during the first few pulses, causing the optical properties of the material to change from transparent to 248-nm light to strongly absorbing of 248-nm light. This kind of incubation and chemical modification was not observed in PTFE. As the fluence increased in this experiment, the etch rate did not remain linear, as would be the case if the light has been absorbed linearly as in classic Beer-Lambert

behavior. Rather, the rate was exponential, and therefore highly indicative of non-linear absorption processes, which include multiphoton absorption and electron avalanche ionization. The ablation of PTFE was determined to have a threshold fluence of approximately  $0.5 \text{ J/cm}^2$  for the 300-fs pulses. The ablation depth per pulse increased approximately linearly between fluences of  $0.5$  and  $1 \text{ J/cm}^2$ , after which the rate of increase slowed dramatically, with the highest experimental point corresponding to approximately  $13 \text{ }\mu\text{m}$  per pulse at a fluence of  $4 \text{ J/cm}^2$ . This is large compared with the disrupted surface that occurred at  $2 \text{ J/cm}^2$  for the 18-ns pulsed laser, which had not removed a significant amount of material even after 50 pulses.

Investigations on ablation of other polymers also illustrate some of the mechanistic properties of subpicosecond ablation of polymeric materials. Bor et al.<sup>17</sup> determined the time dependent reflectivity of polymethylmethacrylate (PMMA), Mylar, and Kapton that had been exposed to 7-mJ, 0.5-ps pulses at 248 nm. The purpose was to identify a material that would work as an ultrafast mirror for an optical switch. The laser used was a KrF excimer distributed feedback dye laser. An unamplified seed pulse was diverted from the oscillator to be used as the probe beam to determine reflectivity. The probe was computer controlled, with an accuracy of 30-fs. In all cases the increase in reflectivity was not observed at  $t=0$ , but within 2-3 ps the reflectivity had peaked between 0.6 and 0.94 for  $50 \text{ J/cm}^2$  pulses in all three materials. A pump pulse of  $5 \text{ J/cm}^2$  was used in PMMA, which led to increased reflectivity approximately 3 ps after the pump pulse. It peaked slightly above 0.6. Kapton was the most promising material investigated, as it showed a reflectivity of approximately 0.94, 2 ps after the pump pulse. In all cases the Fresnel reflectivity for a flat plane was not observed after the pulse, because of the roughened surface. It was clear from the reflectivity data that the plasma lifetime was on the order of 15-30 ps in all cases.

Liu et al.<sup>15</sup>, using a 50-mm polyethylene terephthalate film demonstrated that a 200-ps Ti:sapphire laser required about  $8 \text{ J/cm}^2$  as threshold fluence, or five times higher than the fluence with the 80-fs pulsed laser. The 80-fs pulses also produced clean, uniform holes, whereas the 200-ps pulses resulted in uneven holes with cracking (possibly due to heat diffusion and shock-waves).

It is clear from the data presented, especially the data on Teflon ablation, that the ablation threshold for polymers becomes both smaller and more precise with use of subpicosecond pulses. This result is similar to results with metals and shows a general trend toward the same conclusion across all materials. In the following discussion, which examines the use of subpicosecond lasers for the ablation of covalent and ionic bonded solids, this will be shown to continue to hold true.

### **Ceramics**

Ceramics are more similar to metals than to polymers, in that they are materials with strong bonds. These bonds are covalent or ionic in nature (rather than metallic bonds), but are definitely stronger than the weak forces holding polymers together. The main difference between ceramics and metals is related to the fact that the Fermi energy of the electrons is between the valence and conduction bands. For materials that are considered to be semiconductors, this gap is small, so that a relatively small amount of energy is sufficient to promote electrons to the conduction band. For other ceramics, which are considered to be insulators, including many oxide ceramics and diamond, a larger amount of energy is required to excite electrons to the conduction band. If the band-gap energy is below the photon energy of incident light, then absorption is strong and linear. If the band gap energy is greater than the photon energy, then absorption is small at low intensity and is nonlinear in nature.

*Semiconductors*

Several investigations of subpicosecond laser ablation of semiconductors have been reported, specifically on silicon and germanium, which are covalently bonded solids with a diamond crystal structure.

Herbst et al.<sup>18</sup> reported the use of an excimer-dye laser to ablate both silicon and germanium, using pulses of 15 mJ at 400-fs and 7.5 mJ at 100 fs. The maximum intensity achieved was  $3 \times 10^{13}$  W/cm<sup>2</sup>. The samples were ablated using a 1-mm aperture, imaged at 55:1 onto the sample. During the drilling process, interference and beam inhomogeneities led to the formation of vertical cones and pillars of material. There was no evidence of a liquid phase present on any of the samples ablated with pulses of these energies and durations, which indicates that melt ejection is not the mechanism of material removal. It was found that beam quality could be improved by using a thin sample, previously ablated, held above the sample so that its round hole would cause reflective focusing of the beam, which both increased power density and improved the beam shape and profile. One piece of evidence that melt ejection is not a material removal mechanism is the horizontal steps, approximately  $\lambda/2$  in size, observed on the sides of the ablated holes. The morphology of these steps very closely resembled threshold ablation patterns. The most probable mechanism of ablation appeared to be a direct transition to either a vapor or a plasma phase.<sup>19</sup> Evidence of sonic shock waves around the irradiated areas included some minor chipping. SEM studies comparing grounded to ungrounded samples produced evidence of permanent structural changes caused by multi-photon emission of electrons. This emission caused a negative charge depletion within the material, which in turn creates defects and amorphous regions, which both affect electronic conductivity. It was also found that the 100-fs pulses created sharper edges than the longer 400-

fs pulses. A point of interest is that if a rectangular mask is projected onto a surface, the beam restructures during drilling to become circular in shape, with a diameter approximately 10% smaller than the edges of the rectangle by the exit. This was attributed to reflective focusing of the beam.

Glezer et al.<sup>20</sup> suggested that ultrafast electronic transitions occur when semiconductors are irradiated with high intensity, short-pulsed laser light. It was suggested that the valence electrons are excited to a state that destabilizes the covalent bonds within the material, thereby causing a phase transition. This transition then eliminates the band gap, and the affected volume of the semiconductor consequently behaves like a metal. Multiangle pump probe reflectivity measurements were taken using gallium arsenide, a direct band gap intrinsic semiconductor, and dielectric constants were determined from the data. It was found that above  $0.5 \text{ kJ/m}^2$  ( $0.05 \text{ J/cm}^2$ ) the Drude model was no longer accurate in predicting the dielectric constant. From this, the authors concluded that initial rises in reflectivity are caused not by changes in the dielectric constant, but by significant changes in the electronic structure of semiconductors. The claim was made, based on calculations of others, that when 10% of the valence electrons are excited to the conduction band, the covalent bonds within the material become sufficiently disrupted to result in degradation of the crystal lattice. This destabilization leads to ionic motion and the generation of amorphous material. This finding is significant because simple Drude models are often used in attempts to describe behavior of materials subjected to ultrashort pulsed laser pulses.

As the band gap becomes larger than incoming photon energy, processes such as multi-photon absorption and impact ionization become more important. Investigations of the ablation

behavior of insulating ceramics, which have significantly higher band gap in comparison to semiconductor have also been investigated.

### *Oxide Ceramics*

Ablation of oxide ceramics by use of sub-picosecond pulsed lasers has been studied, with respect to various applications, including micromachining, thin film deposition, and study of optical damage mechanisms. An understanding of the causes and results of optical damage in transparent optical materials is essential when considering ultrashort pulsed laser ablation of insulating ceramics, including fused silica and other metal oxides.

Stuart et al.<sup>9</sup> studied the damage thresholds in two materials, calcium fluoride and fused silica (super polished < 1-nm rms surface roughness). This review will focus mainly on results achieved with fused silica. Damage thresholds were determined by visual observation of the material after multishot exposure to laser light of various fluences and pulse widths. Damage was evaluated using a Nomarski microscope. The practical limit of detection of damaged material was approximately 0.5  $\mu\text{m}$ , which was significantly less than the laser spot size. It should also be noted that material damage was evaluated on only the front surface of the material. Multiple exposures were used to ensure that any damage that occurred within the material would grow to an observable size after several pulses.

Measurements were taken up to 1-ns. Above 20 ps, the fluence threshold was proportional to the square root of the pulse width ( $\tau$ ). Below 20 ps, this relationship did not hold; the fluence threshold continued to decrease, but at a slower rate. The minimum damage threshold was 2 J/cm<sup>2</sup> at 400-fs. Additionally, the morphology of the damaged material changed at around 20 ps. Above 20 ps, the damage was definitely thermal in nature, as evidenced by material that had been melted and undergone viscous flow. Below 20 ps, the damage appeared

as “a shallow fractured and pitted crater characteristic of a thin layer of material removed by ablation.” It was also reported that the damaged areas of the ultrashort pulses ( $< 10$  ps) was many orders of magnitude smaller than with the longer pulses. A more in-depth discussion was included in a paper by Stuart et al.<sup>9</sup> on the theoretical predictions of electron transitions caused by multiphoton absorption and impact ionization.

Du et al.<sup>21</sup> studied the breakdown of fused silica induced by 780-nm laser pulses at pulse widths from 150 fs to 7 ns. The energy fluence threshold varied with the square root of pulse width only if the pulse width was greater than 10 ps. The breakdown mechanism was photoionization for the generation of the initial free electrons, followed by electron avalanche ionization. The experimental data on the ionization rate closely followed results predicted by impact ionization theory.

Ihlemann et al.<sup>22</sup> compared nanaosecond- and femtosecond-pulsed ablation of fused silica. They used 193, 248, and 308-nm with 20-30-ns pulses, along with 248-nm, 500-fs pulses. Experiments were all carried out in vacuum (1 bar for the ns pulses,  $10^{-2}$  mbar for the fs pulses). The lower vacuum was required for the femtosecond pulses to prevent air breakdown in front of the sample.

At 193 nm and lower fluences ( $3 \text{ J/cm}^2$ ), the ablation of fused silica occurred at the back face of the sample. Deep holes with sharp edges and smooth grounds (hole bottoms) were created. At higher fluences, ablation occurred at the front surface, which resulted in a lower material removal rate and better-defined walls than with the rear surface ablation.

At 248 nm and 28 ns, smooth silica surfaces underwent two phases of ablation. Rough silica surfaces underwent only one phase of ablation, which was similar to the second phase for the smooth surfaces. In this experiment, the smooth surfaces underwent the first phase for 20-50

pulses. This phase is characterized by a clean ablation process and low material removal rates, in contrast to the second phase, characterized by rugged craters and high material removal rates.

At 308-nm with 33-ns pulses smooth samples showed very high ablation thresholds, 20 J/cm<sup>2</sup>, above which destructive cracking occurred. Rough samples could be ablated in a controlled way at lower fluences.

The effects of ablation at 248-nm, 8.2 J/cm<sup>2</sup>, and 500 fs also showed a two-phase ablation process on the front surface of the samples. The femtosecond and nanosecond ablation processes differed significantly. The incubation period is only one or two pulses, and the material removal rate remains constant (as opposed to increasing). The surface of the hole switches from a smooth, reflecting surface to a rippled surface with a few drops of melted and recooled glass attached.

It is obvious from the above data that when nanosecond and femtosecond pulses are compared, the femtosecond pulses show a reduced thermal diffusion effect. Large-scale cracks were observed in the nanosecond pulsed samples, but not in the femtosecond pulsed samples; this indicates that thermal diffusion and material heating are causing thermomechanical stresses that lead to cracking. In the femtosecond-pulsed sample, the strongest evidence for thermal damage is small droplets of material that had obviously melted and quickly recooled. It is interesting that the higher photon energy at 193-nm created smoother holes than all other conditions used. Data presented also showed that the 248-nm, 500-fs pulses had a threshold of ablation around 1 J/cm<sup>2</sup>. It would be interesting to determine whether fluences kept close to threshold would result in the ultrashort pulsed ablation which was cleaner and more precise, as reported by Chichkov et al.<sup>2</sup> in metals.

Ihleemann et al.<sup>24</sup> compared femtosecond- and nanosecond-pulsed excimer-laser ablation of oxide ceramics with pulse characteristics of 248 nm for 500 fs and 30 ns pulses, and 308 nm 30 ns. The experimental conditions were similar to those of the previous study<sup>22</sup> on silica. The results were similar for alumina and magnesia. A general trend of lower threshold fluence and increased material removal rate was observed for sub-picosecond (500 fs) pulses when compared with 30-ns pulses. Threshold fluence decreased with decreasing wavelength (increasing photon energy). Pulse probe experiments with the alumina showed increased reflectivity due to plasma formation for about 18 ns after the beginning of the pulse, which indicates that much of the laser energy from a nanosecond length pulse is not directly absorbed by the material. The sub-picosecond pulses showed an improved coupling of radiative energy with the material, because the pulse is absorbed before significant plasma can form. This led to a process that yielded less thermal damage within the sample. Zirconia was shown to have similar ablation thresholds for both the 248-nm pulse widths. This was attributed to zirconia's low bandgap, which decreases the importance of nonlinear absorption processes. In all cases, the femtosecond pulses showed a larger material removal rate at identical energy fluence. Threshold fluences were lower for the larger band gap materials; this was attributed to the increased absorption due to the ultrahigh intensity.

Stuart et al.<sup>14</sup> demonstrated the benefits of a 350-fs pulsed laser over a 1.4-ns pulsed laser for hole drilling of tooth enamel. In the case of 1.4-ns pulses, an energy fluence of 30 J/cm<sup>2</sup> was required to drill the holes, yet the uncontrolled nature of material removal resulted in cracking and significant thermal damage. In contrast, the 350-fs laser required only 3 J/cm<sup>2</sup>, and material removal did not involve any thermal damage. Temperature measurements showed that in the

case of the 1.4-ns laser, the bulk temperature of 1 mm slices of tooth increased over 40° C, whereas for the 350-fs laser, the temperature rise was only 2° C.

Ashkenasi et al.<sup>24</sup> reported that the nonlinear optical effects of femtosecond pulsed ablation, along with the reduced thermal effects and high precision, allowed manufacture of 3D microstructures in transparent materials such as sapphire, quartz and CaF<sub>2</sub>. The Ti:Sapphire laser processing of the transparent materials at 4.5 ps and 200 fs showed that the 200 fs ablations greatly improved surface quality.

Subpicosecond lasers have been shown to create more precise, lower threshold fluences of ablation in insulating oxide ceramics. Theories on this finding point toward an increase in nonlinear absorption compared with nanosecond-pulsed lasers. It has also been shown that ablation with fluences far above the ablation threshold continue to create unwanted thermal effects within the materials. Therefore, for precise applications, fluences should be kept close to the threshold for ablation.

### *Laser-material interactions*

When a laser beam interacts with a material, electrons are excited by the absorption of photons. The electrons are heated to high temperature by absorbing laser energy through collisions with ions. Subsequent electron-phonon interactions allow the absorbed energy to be transferred to the lattice in a time frame of picoseconds for most materials. For femtosecond pulses, there is insufficient time for energy transfer to the lattice; consequently, thermal damage is minimal. If the fluence in a femtosecond pulse exceeds 0.1 J/cm<sup>2</sup>, very high carrier densities of 10<sup>22</sup> /cm<sup>2</sup> in semiconductors and high electron gas temperatures (10,000 K) in metals may be achieved,<sup>25</sup> so the workpiece does not melt, but is vaporized. Because the atoms have too little time to move during the pulse, extremely high pressures and high temperatures can be attained.

Several important phenomena must be considered with respect to laser-material interaction. These include the type and magnitude of light energy absorption and the time scale of the laser pulse in relation to the time scale of the electron and lattice reactions to the laser energy. In the ultrashort pulsed laser area, understanding these processes is extremely important, because the extreme intensity of the light, along with its short time frame compared with classical heat transfer, make predictions impossible. In materials, light absorption is classically described in terms of the Beer-Lambert law, which states that the absorption of a specific wavelength of light transmitted through a material is a function of the material path length, and is independent of incident intensity. This expression is generally acceptable for moderate intensities, but at extremely high intensities, as in ultrashort pulsed laser processing, nonlinear effects become important and light is absorbed more quickly in processes such as multiphoton absorption. Linear absorption implies that the electrons, heated by photon absorption, transfer the heat energy to the lattice, thereby causing melting or vaporization. Linear processes are used to describe lower-intensity laser-material interactions. At extreme intensities, as is the case for femtosecond lasers, the bound electrons of the material can be directly ionized. A bound electron can be freed from the valence band by absorbing “m” photons when  $mh\nu > U$ , where “U” is the ionization potential or bandgap strength. Other interactions, which include processes involving avalanche ionization and photon-phonon interactions, also may be important. Another important consideration for pulsed material processing is thermal conduction within a material, which can draw laser energy away from the focal area.<sup>12</sup> This can lead to large heat-affected zones and reduced ablation efficiency in longer pulse width lasers. At low intensity, conduction effects are minimized in ultrashort pulse processing of materials.

### Photon absorption processes

The first step that must occur in laser ablation is absorption of a significant amount of the laser light. In materials such as metals, this is not a problem; the band structure of the material allows absorption of most low-to moderate-energy photons, because the Fermi level is in the middle of an electron band. For semiconductors and insulators, including ceramics and insulating polymers, the Fermi energy is between the valence and conduction bands. This creates a region of photon energies that cannot be absorbed by linear processes because of the requirement that an electron absorb enough energy to be elevated through the forbidden region between the valence and conduction bands. This can be accomplished by one of two processes: electron avalanche and strong multiphoton absorption. Electrons at defect sites, which have intermediate energies, can be easily excited into the conduction band by single photon absorption. Also, small amounts of multiphoton absorption can lead to a small number of electrons entering the conduction band. Electrons in the conduction band can absorb single photons of light, which increases their kinetic energy. Collisions of these excited electrons with bound electrons leads to avalanche ionization. Strong multiphoton absorption can also occur.<sup>25</sup> It is claimed that use of intensities in excess of  $10^{12}$  W/cm<sup>2</sup> makes it possible to heat the surface of any material to temperatures above  $10^4$  K.

Multiphoton absorption is important in two different instances of high intensity ultrashort pulse laser material processing. The obvious case is nonlinear absorption of photons in semiconductors and insulators, in which the band gap is greater than the incident photon energy. The second case is in materials exposed to ultrahigh intensities, in which absorption deviates from Beer-Lambert behavior by showing more intense absorption due to nonlinear absorption processes. This means that absorption becomes intensity dependent.

Jones et al.<sup>26</sup> have reviewed the most probable causes of laser-material breakdown in wide-gap optical materials, including the history of laser-induced damage. They also discuss a theory in which the accumulation of multiphoton generated electrons produces thermomechanical stresses and eventual breakdown in dielectrics. The equation that describes multiphoton absorption is as follows:

$$\frac{dn}{dt} = N \cdot \sigma^{(m)} \cdot F^m \quad (3)$$

This generally states that the rate of change of valence electrons to conduction electrons is dictated by  $N$ , the active ion density;  $\sigma^{(m)}$ , the  $m$ -photon absorption cross section; and  $F$ , the incident photon flux density. Electrons excited by this mechanism can then undergo other processes, such as low energy photon absorption, that can lead to impact ionization<sup>5</sup>. Another mechanism for electron heating is photon-phonon-electron collisions. Once the conduction electrons gain enough kinetic energy, then collisions with valence electrons can yield two low-energy conduction electrons. In certain cases, intense pulses may create enough multiphoton absorption to eliminate the need for further impact ionizations to obtain an electron density that will absorb sufficient laser light. In general, once the material has a critical density of electrons, it starts absorbing sufficient photon energy to undergo ablation.

Pronko et al.<sup>19</sup> developed a finite difference scheme to describe the interactions between 800-nm laser pulses and silicon in the energy regime where melting and vaporization can occur and at pulse widths ranging from 80-fs to 0.2-ns. The mechanism of fs-laser pulse energy absorption, in contrast to that of ns-laser pulse widths, involves energy absorption by a thin surface plasma generated by avalanche ionization and having near-solid density.

The numerical procedure consisted of solving two transport equations that involve heat absorption by electrons in silicon's surface and subsequent energy transfer to the lattice ions and

atoms. In addition, the temperature-dependent electron-lattice coupling coefficient was calculated and incorporated into the model. The model calculations showed that the electron temperatures can reach 20,000 K, nearly 15 times that of the lattice.

The model was also used to compute the absorption depth and energy thresholds for silicon vaporization as a function of pulse width. For long pulses, the absorption depth for silicaon was 6.6  $\mu\text{m}$  at 800-nm. The computer model predicted a smaller absorption depth of 78-nm, which is verified by the energy balance equation given by:

$$C_i(T_V - T_\infty) + L_v + L_m = E_{th}\delta \quad (4)$$

where  $C_i$  is the volume heat capacity of the ions,  $\delta$  is the depth of the vaporization layer, and  $L_v$  and  $L_m$  are the latent heats of vaporization and melting, respectively. There was excellent correlation between the computer-predicted and experimental energy thresholds, especially in the pulse width range from 0.1-ps to 100-ps.

#### **Thermal conduction in solids**

In thermal conduction in ultrashort-pulsed laser processing, several important factors must be considered. These include the effects of physical processes (including electron-lattice energy coupling, thermal conduction, and phase transition such as melting and vaporization) on laser energy deposited in a material.<sup>27</sup> The thermal diffusion length, which readily considered, is approximately obtained by the following equation:

$$L = \sqrt{D \cdot t} \quad (5)$$

where  $L$  is the diffusion length and  $D$  is the ratio of thermal conductivity to the volume heat capacity, and  $t$  is the pulse width. It can be seen that for sufficiently short  $t$ ,  $L$  can become extremely small, and for cases such as ultrashort-pulsed laser processing,  $L$  can become smaller than the focal size of the laser. Many models use this fact in asserting that thermal diffusion is

negligible. However, this is not so if the energy delivered is such that the plasma can deliver a significant amount of energy to the surrounding material, as was the case in the previously discussed paper by Luft et al.<sup>16</sup> The necessary considerations should then be that the energy delivered must be sufficient to cause material removal and to allow the plasma to expand so that it does not interact significantly with adjacent material. If the plasma transfers sufficient energy to the adjacent material, then undesirable effects, including melting, may become problems. For long pulses, the volume of material heated by the laser pulse is determined by the thermal diffusion length. This implies that the energy threshold is proportional to the square root of pulse width. But when the pulse width becomes small, the absorption depth governs the heated volume and the threshold therefore becomes independent of the pulse width.

#### **Material removal mechanisms and models**

For long-pulsed lasers, ablation of materials occurs through melt expulsion driven by the vapor pressure and the recoil pressure of light. This is an unstable process in which the dynamics of the fluid phase and the driving vapor conditions are quite complicated. The melt layer is resolidified, resulting in geometric changes of the holes. With ultrashort pulses, the deposited energy is limited to a smaller depth and the absorbed energy heats the material very quickly past the melt to the vapor phase, with its high kinetic energy. The material is removed by direct vaporization away from the surface without formation of a recast layer.

For transparent materials, the mechanism is said to be “laser-induced optical breakdown”; i.e., the material is changed to a plasma upon absorption of laser energy, and subsequent absorption of laser energy by the plasma leads to damage of the material. Two phenomena, avalanche ionization and multiphoton absorption, are responsible for the laser-induced optical

breakdown. As pulse width decreases, intensity increases, and the mechanism of laser absorption shifts from avalanche ionization to multiphoton absorption.

Avalanche ionization is caused by ionization of bound electrons. The bound electrons require energies higher than available photon energies. To ionize the bound electrons, highly excited free electrons will collide with them; this collision exceeds the ionization potential of the bound electron, leading to two free electrons. These electrons in turn absorb more photons of light, gaining kinetic energy. The process repeats itself, leading to a large number of electrons in the conduction band. The density of ions produced by this mechanism is approximately  $10^{18}$  /cm<sup>3</sup> for ns-pulses and  $10^{21}$  /cm<sup>3</sup> for fs-pulses.

A material ablation model must take into account three aspects: the volume of material that absorbs energy sufficient to result in a phase transition, the heat conducted out of the material, and, finally, the energy required for melting and/or vaporization. The model presented by Chichkov et al.<sup>11</sup> works well for metals and may be sufficient for materials with a significant band gap, given certain modifications. Most electric insulators are also poor thermal conductors. Therefore, the assumption that thermal conduction is negligible during the timescale of ultrashort pulsed processing appears to remain valid. The assumption that reflectivity is constant has been shown to be false, but perhaps can be compensated for by using data from pump probe reflectivity experiments. This would probably lead to a compensation in which the laser energy reflected exceeds that attributed to the Fresnel reflection at low intensity. The assumption that ablation and plasma formation occur after the laser energy is delivered should be true for sufficiently short pulses, a phenomenon that may be material dependent. The final factor that must be determined is the enthalpy of sublimation for a material at the processing temperature and pressure. This may or may not be available in the literature, but an

approximation from appropriate chemical bonding calculations should be possible. The last consideration is the effects of nonlinear absorption on the ablation volume.

Equation (2) then will become a volume integral in which  $\alpha$  will show a strong dependence on incident intensity and the energy absorbed by the material will be affected by changes of the absorption coefficient within that space.

The threshold energy fluence can be a stochastic or deterministic quantity, depending on the pulse width. For long-pulsed lasers, energy fluence varies significantly because of the statistical variation of free electrons and, consequently, avalanche ionization. With ultrashort pulsed lasers, multiphoton ionization occurs and breakdown is completed by avalanche ionization; here, the electron density becomes so high that it does not exhibit statistical variations. Thus, the threshold fluence is very precise for ultrashort pulsed laser ablation.

### *Conclusion*

Research has clearly indicated that ultrashort pulsed lasers offer advantages over longer-pulse lasers for ablation and micromachining applications. Femtosecond lasers are widely considered the manufacturing tools of the future because of their characteristics: capability of processing practically any material, high precision, larger material removal rate, and minimal thermal damage. The advantages of femtosecond lasers over long-pulsed lasers, which are attributed to the deposition of laser energy into the electrons of the material in a time much shorter than the transfer time to the lattice, are a result of two processes: thermal diffusion and nonlinear absorption.

The first, thermal diffusion, is negligible on the time scales of these pulses. It has been shown conclusively that the reaction volumes are consistently below those of the thermal diffusion volume, which is not the case for longer ( $> 20$  ps) pulses. This prevents material

outside the area irradiated above threshold from being affected by thermal energy, unless the pulse is so energetic that the plasma that remains at the ablation site is able to transfer energy to the workpiece. Factors including sonic shock and other effects of high intensity radiation can lead to other non-thermal deformation processes, but these appear to be less significant than the problems encountered when a hole-drilling process experiences instabilities due to a molten phase.

The second factor that contributes to production of smaller interaction volumes is the nonlinear absorption induced by the extreme intensities of ultrashort pulses. The most significant processes in nonlinear absorption are multiphoton absorption and avalanche ionization, which are insignificant at low intensities but which become increasingly probable at the gigawatt- and terawatt-per-square-centimeter intensities these lasers create. The consequence of nonlinear absorption is that the laser light is absorbed by a much smaller volume of the material than would be predicted by the Beer-Lambert relationship.

The consequence of both these processes is a more precise ablation process, as demonstrated in metals, polymers, and ceramics. In metals, the femtosecond laser can precisely remove small amounts of metal (0.01 to 1  $\mu\text{m}$ ) through selection of a pulse width that gives rise to a thermal diffusion distance equal to the optical skin depth. The accompanying minimization of energy loss by thermal conduction allows machining of holes that have very high aspect ratios, no recast layer, and no cracking. It has been shown that materials difficult to process with longer pulse treatments are laser machinable with ultrashort pulses and that high reflectivity materials such as copper can be ablated with moderate energy, ultrashort pulses. Other materials that have been ablated successfully with ultrashort pulses are high-band-gap materials, including Teflon, oxide ceramics, and diamond. Previous studies on ablation of Teflon had shown that

the best effect achievable was a thermally disrupted surface, even with intense high energy pulses at wavelengths as short as 193-nm. In summary, ultrashort pulsed laser material processing has expanded the range of ablatable materials, along with greatly improving the precision with which a feature can be created by use of laser light.

### *References*

1. M. C. Richardson, "New Opportunities with intense ultrashort pulse lasers," Proc. SPIE **1410**, 15-25 (1991).
2. D. Strikland and G. Mourou, "Compression of amplified chirped optical pulses," Opt. Commun. **56**, 219-221 (1985).
3. C. P. J. Barty, "Ten-femtosecond amplifier creates multiterawatt pulses," Laser Focus World **32**, 93-106 (1996).
4. S. Szatmari and F. P. Schafer, "Subpicosecond, widely tunable distributed feedback dye laser," Appl. Phys. B: Photophys. Laser Chem., **46**, 305-311 (1988).
5. J. R. Hobbs, "Chirped-pulse amplification sustains 30-fs multiterawatt pulses," Laser Focus World, **30**, 29-30 (1994); **63**, 109-115 (1996).
6. B. E. Lemoff and C. P. J. Barty, "Generation of high-peak-power 20-fs pulses from a regeneratively initiated, self-modelocked Ti:sapphire laser," Opt. Lett. **17**, 1367-1369 (1992).
7. C. P. J. Barty, C. L. Gordon, III, B. E. Lemoff, C. Rose-Petruk, F. Raski, Ch. Spielmann, K. R. Wilson, V. V. Yakovlev, and K. Yamakawa, "Methods for generation of 10-Hz, 100-TW optical pulses", Proc. SPIE **2377**, 311-322 (1995).
8. A. Stingl, M. Lenzner, Ch. Spielmann, and F. Krausz, "Sub-10-fs mirror-dispersion-controlled Ti:sapphire laser", Opt. Lett. **20**, 602-604 (1995).
9. B. C. Stuart, M. D. Feit, A. M. Rubenchik, B. W. Shore, and M. D. Perry, "Laser-Induced damage in dielectrics with nanosecond to subpicosecond pulses," Phys. Rev. Lett. **74**, 2248-2251 (1995).
10. S. Kuper and M. Stuke, "Ablation of polytetrafluoroethylene (Teflon) with femtosecond UV excimer laser pulses," Appl. Phys. Lett. **54**, 4-6 (1988).
11. B. N. Chichkov, C. Momma, S. Nolte, F. von Alvensleben, and A. Tunnermann, "Femtosecond, picosecond, and nanosecond laser ablation of solids," Appl. Phys. A: Solids Surf. **63**, 109-115 (1996).

12. P. P. Pronko, S. K. Dutta, J. Squier, J. V. Rudd, D. Du., and G. Mourou, "Machining of sub-micron holes using a femtosecond laser at 800-nm," *Opt. Commun.* **114**, 106-110, (1995).
13. S. Preuss, A. Demchuk, and M. Stuke, "Sub-picosecond UV laser ablation of metals," *Appl. Phys. A: Solids Surf.* **61**, 33-37 (1995).
14. B. C. Stuart, M. D. Perry, M. D. Feit, L. B. Da Silva, A. M. Nev Rubenchik, S. Herman, H. Nguyen, and P. Armstrong, "Femtosecond laser processing," *Conference on Lasers and Electro-optics, 1997 OSA Technical Digest Series* (Optical Society of America, Washington DC, 1997), Vol. 11, pp. 159-160.
15. X. Liu, X. Chen, W. T. Lotshaw, and A. C. Tien, "Elimination of recast layer and microcracking in laser machining with femtosecond pulses," *Conference on Lasers and Electro-optics, 1997 OSA Technical Digest Series* (Optical Society of America, Washington DC, 1997), Vol. 11, p.162.
16. A. Luft, U. Franz, A. Emsermann, and J. Kaspar, "A study of thermal and mechanical effects on materials induced by pulsed laser drilling," *Appl. Phys. A: Solids Surf.* **63**, 93-101 (1996).
17. Z.m. Racz, B. Bor, G. Szabo, D. Xenakis, C. Kalpouzou, and C. Fotakis, "Femtosecond transient reflection from polymer surfaces during femtosecond UV photoablation," *Appl. Phys. A: Solids Surf.* **60**, 365-368 (1995).
18. G. Herbst, M. Steiner, G. Marowsky, and E. Matthias, "Ablation of Si and Ge using UV femtosecond laser pulses," *Mater. Res. Soc. Symp. Proc.* **397**, 69-74 (1996).
19. P. P. Pronko, P. A. VanRompay, R. K. Singh, F. Qian, D. Du, and X. Liu, "Laser Induced Avalanche Ionization and Electron-Lattice Heating of Silicon with Intense Near IR Femtosecond Pulses" *Mater. Res. Soc. Symp. Proc.* **397**, 45-51 (1996).
20. E. N. Glezer, L. Huang, Y. Siegal, J. P. Callan, and E. Mazur, "Phase transitions induced by femtosecond pulses," *Mater. Res. Soc. Symp. Proc.* **397**, 3-20 (1996).
21. D. Du, X. Liu, G. Korn, J. Squier, and G. Mourou, "Laser-induced breakdown by impact ionization in SiO<sub>2</sub> with pulse widths from 7 ns to 150 fs," *Appl. Phys. Lett.* **64**, 3071-3073 (1994).
22. J. Ihlemann, B. Wolff, and P. Simon, "Nanosecond and femtosecond excimer laser ablation of fused silica," *Appl. Phys. A: Solids Surf.* **54**, 363-368 (1992).
23. J. Ihleman, A. Scholl, H. Schmidt, and B. Wolff-Rottke, "Nanosecond and femtosecond excimer-laser ablation of oxide ceramics," *Appl. Phys. A: Solids Surf.* **60**, 411-417 (1995).
24. D. Ashkenasi, A. Rosenfeld, H. Varel, and E. E. B. Campbell, "Laser-induced microstructuring of dielectrics using ultrashort laser pulses," *Conference on Lasers and Electro-optics, 1997 OSA Technical Digest Series* (Optical Society of America, Washington D.C., 1997), Vol. 11, p.161.

25. N. Bloembergen, "Laser-Material interactions; fundamentals and applications," Proceedings of LAMP, pp. 3-8, 1992.
26. S. C. Jones, P. Braunlich, R. T. Casper, X. A. Shen, and P. Kelly, "Recent progress on laser-induced modifications and intrinsic bulk damage of wide-gap optical materials," *Opt. Lett.* **28**, 1039-1068 (1989).
27. P. P. Pronko, S. K. Dutta, and D. Du, "Thermophysical effects in laser processing of materials with picosecond and femtosecond pulses," *J. Appl. Phys.* **15**, 6233-6240 (1995).
28. C. P. J. Barty, T. Guo, C. Le Blanc, F. Raksi, C. Rose-Petruck, J. Squier, K. R. Wilson, V. V. Yakovlev, and K. Yamakawa, "Generation of 18-fs, multiterawatt pulses by regenerative pulse shaping and chirped-pulse amplification," *Opt. Lett.* **21**, 668-670 (1996).

## CHAPTER 4. ULTRASHORT PULSED LASER ABLATION OF DIAMOND

A paper published in the Journal of Laser Applications (1998)<sup>a</sup>

M. D. Shirk, P. A. Molian, and A. P. Malshe

### *Abstract*

Laser processing of diamond and chemical vapor-deposited (CVD) diamond thin films is important in the microelectronics and cutting tool industries because the manufacture of diamond films with low surface roughness and complex shapes has proven to be difficult. In this paper we present a review of current laser polishing and ablation processes followed by a discussion of ultrashort pulsed processing of diamond. Compared with the use of longer pulsed lasers, the use of 248-nm, 500-fs duration pulses at extreme intensity offered multiple advantages, including a lack of lateral thermal damage and significant improvements in the structural purity of the ablated surface. Experimental data, including Raman spectra and scanning electron micrographs (SEM), were presented to demonstrate the superior capabilities of this new class of lasers.

### *Introduction*

Studies on ablation of the two common phases of carbon, graphite and diamond, will be reviewed with respect to wavelength and temporal electronic properties. An attempt will be made to present a picture that can be used to explain the results of original femtosecond ablation data obtained by Molian et al.<sup>1,2</sup>.

---

<sup>a</sup>. Journal of Laser Applications 10:2 (1998) p. 64-70, published by Laser Institute of America

The chemical-vapor-deposited (CVD) diamond field is a multimillion-dollar-per-year market that has numerous applications in manufacture of products ranging from tools to electronic modules. CVD diamond is the material of choice as a thermal spreader for advanced electronic packages such as 3-D MCMs (multichip modules) and laser diode thermal spreaders. The state-of-the-art CVD diamond growth technology led to films with large surface roughness, wavy patterns due to stress-related phenomena, and impurities such as graphite. Smoothing and hole drilling of the films are necessary for electronic device and tribological applications.

The sub-picosecond ablation of diamond produced evidence of the expected effects of the high intensity short pulse. Diamond is a difficult material to ablate, and some of the effects observed in long-pulse processing are absent in the ultrashort processes. Diamond usually undergoes a transition to graphite during ablation. Because diamond is a large band gap material, it must undergo a transition that makes it opaque to the incident light. This can occur by multiphoton absorption, photon-phonon-electron collisions, phase transition, or the development of color centers through defect formation.

CVD diamond machining currently uses millisecond Nd:YAG and nanosecond excimer lasers. Drawbacks of this method include the formation of non-diamond phases, low material removal rates, and a lack of precision.

Studies by Windholz and Molian, Konov et al., Christensen, and Tosin et al.<sup>3-7</sup> have generated papers on the practical applications of lasers for microprocessing, micromachining, and light-induced polishing of diamond and graphite.

Windholz and Molian<sup>3,4</sup> studied the effects of 248 nm pulses on the ablation of chemical vapor deposited (CVD) diamond thin films and graphite. These studies included ablation at 23-ns, along with Raman spectroscopy, profilometry, and SEM analysis. The main conclusion was

that the ablation threshold was nearly the same for CVD diamond and graphite, but increased energy fluence increased the material removal rate much more for the graphite, as can be seen in Figure 1, which is a comparison plot of depth-per-pulse versus fluence for both. The Raman spectra for pristine and laser treated diamond (Figure 2) show that the peak at  $1332\text{ cm}^{-1}$  was lost on treatment with the laser, which indicates that the surface is no longer diamond in structure. This conversion of the surface from diamond to graphite explains both the ablation threshold similarities of the two materials and the limiting kinetics of the ablation of diamond. The diamond must be converted to an optically absorbing, thermally insulating surface for the ablation to take place with 23-ns laser pulses at 248 nm. The graphite on the diamond's surface undergoes sublimation, because liquid carbon is not in a stable phase at atmospheric pressures.

Konov et al.<sup>5</sup> studied KrF excimer laser processing of diamond and amorphous diamond-like thin films. Both chemical vapor deposited diamond and diamond-like carbon thin films were irradiated with a 248 nm KrF excimer laser. Two pulse widths, 20-ns and 0.8-ns, were studied. The maximum fluence investigated was  $10\text{ J/cm}^2$ . The ablation threshold fluence was shown to be approximately  $4\text{ J/cm}^2$  for the 20 ns pulse width, whereas the threshold ablation fluence was much smaller,  $0.15\text{ J/cm}^2$  for the 0.8 ns pulse. The ablation mechanism this group proposed was a transformation from diamond to graphite, followed by sublimation. Laser polishing was also demonstrated in this paper by scanning a laser beam over large areas. SEM micrographs showed noticeably smoother surfaces, and a ripple structure that appeared to be approximately  $10\text{ }\mu\text{m}$  wide. The behavior of the diamond-like films with regard to laser ablation showed a strong dependence on atmosphere. The threshold for ablation in vacuum was very high, whereas ablation in air and pure oxygen had far lower thresholds. This indicated

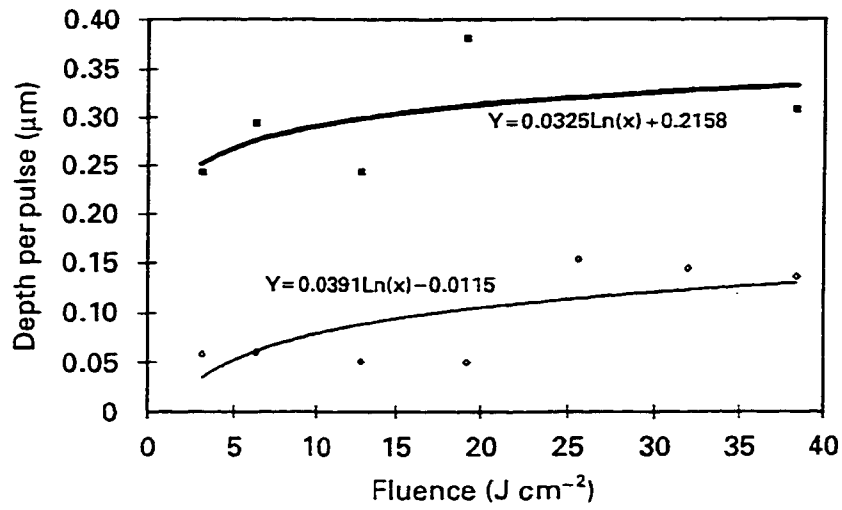


Figure 1. A plot of 23 ns depth per pulse data vs. fluence for both graphite and CVD diamond thin films.

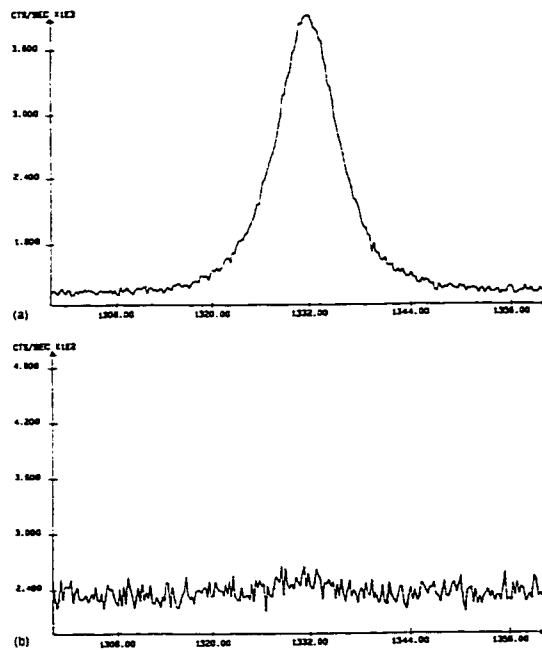


Figure 2. (a) Raman spectra of a CVD diamond thin film which has not been exposed to laser light. (b) Raman spectra of CVD diamond exposed to 23 ns 248 nm pulses.

that ablation was occurring by oxidation of the carbon and hydrogen present in the diamond surface. The etch rates appeared to follow the same curve for all three atmospheres after approximately  $500 \text{ mJ/cm}^2$ , which was the position of the threshold for ablation was shown to be for the vacuum ablated diamond-like films.

In a report on micromachining of diamond and diamond films with a waveguide excimer laser, Christensen<sup>6</sup> reported that three dimensional structures can be created by a combination of scanning the workpiece under the focused beam and varying the beam intensity. The structures described had high spatial resolution and good surface finishes. The laser used was a  $50 \mu\text{J}$ , 80-ns, 248 nm laser capable of a repetition rate up to 2 kHz. The system uses a CAD/CAM controlled x-y stage. The precision the author claims possible is due to a mechanism involving conversion of the diamond surface to graphite by interaction with the 248 nm light, followed by sublimation of the thin graphite film. This sublimation is possible because graphite is more highly absorbing of the laser light as well as showing a much lower thermal conductivity than diamond<sup>5</sup>.

Tosin et al.<sup>7</sup> investigated the use of lasers to polish thin diamond films. It had been shown previously<sup>5</sup> that laser polishing of diamond with excimer lasers at 248 nm and 193 nm yielded a ripple structure. Because the mechanism of rippling on the surface was not understood, both a 193 nm ArF and a  $1.06 \mu\text{m}$  Nd:YAG were used to study wavelength effects on the surface of the diamond. It was determined that laser wavelength had no effect on the rippling structure, which was finally, but not conclusively, attributed to the crystal size of the diamond film. It was shown that rotating the sample during treatment eliminated shadowing effects from the grains, which in turn eliminated the rippling structure. The following conditions were set to avoid rippling:

- 1) An equal number of pulses must be applied to the film within each azimuthal angle interval.
- 2) The energy flux density cumulated over all pulses must be identical at all spots.

An attempt to understand the effect of ultrashort pulse interactions with diamond and graphite was pursued by Reitze et al.<sup>8</sup> Pulse-probe experiments were used to examine diamond and graphite reflectivity after sub-picosecond laser excitation of the structure. The reflectivity of both diamond and highly oriented pyrolytic graphite (HOPG) in a highly excited dense electron-hole plasma was reported. Reflectivities were found to be similar, although that of diamond was slightly lower. This difference was attributed to the difference in density of the two materials, diamond is higher than that of graphite (3.5 g/cm<sup>3</sup> vs. 2.2 g/cm<sup>3</sup>). The general trend in both cases is an abrupt rise in reflectivity within the first picosecond after the pump pulse, followed by a constant decline in reflectivity, to below the initial reflectivity, for at least the next 15-20 ps. The initial reflectivity increase was explained by the creation of a highly reflective dense liquid, or plasma. This theory is supported by similar observations in gallium arsenide obtained in a study by Glezer et al.<sup>9</sup>, in which the lattice was degraded by subpicosecond, high-intensity laser illumination. The excitation was followed by hydrodynamic expansion approximately 3-ps after the initial pulse, which caused degradation of the optical properties of the surface. The authors stressed that the phenomena of interest must be observed within the first few picoseconds after the initial femtosecond-duration pulse. Several other lines of evidence were cited regarding the importance of the first picosecond. These include results of previous experiments that showed that electron relaxation times were approximately the same for carbon excited to states both above and below the ablation threshold. Further evidence was obtained in ab initio molecular dynamics studies by Galli et al.<sup>10</sup> This evidence indicated that structural and electronic relaxation occurred within 1 ps in molten carbon. It was concluded that within 1-ps, both diamond and graphite have equilibrated to the same liquid phase, or possibly the same solid dense plasma.

Data reported by Reitze et al.<sup>8</sup> included a comparison of the threshold fluences for ablation of graphite and diamond using 620 nm, 90-fs laser pulses. The threshold fluence for HOPG was approximately 0.1 J/cm<sup>2</sup>; diamond required a higher energy density, 0.6 J/cm<sup>2</sup>. This difference points to the different absorption mechanisms which both materials encounter. Graphite is a narrow band gap semiconductor, whereas diamond is an electronic insulator with a wide band gap. It was shown that reflectivity (R) and transmittivity (T) in diamond were related to the fluence<sup>8</sup>; both R and T were reduced from 0.75 and 0.25, respectively, at low fluence to approximately equal values of 0.2 at the damage fluence. When the fluence was increased to 10 times the damage fluence, R increased to 0.4 whereas T dropped nearly to zero.

### *Experimental procedure*

Femtosecond pulsed-laser experiments were performed at Laser-Laboratorium, Gottingen, Germany, using Lambda Physik's FAMP system with UV-amplifier module. Figure 3 shows the experimental setup. The beam was passed through a circular aperture, reflected off a 45° mirror, and then imaged to a spot size of 150 μm on the sample mounted inside a vacuum chamber. The machining was carried out on 700-μm-thick, freestanding diamond films and on type IIA single crystal diamond. The following five different energy fluences were used for the processing:  $E_1 = 6.43 \text{ J/cm}^2$ ,  $E_2 = 4.44 \text{ J/cm}^2$ ,  $E_3 = 2.86 \text{ J/cm}^2$ ,  $E_4 = 1.59 \text{ J/cm}^2$ ,  $E_5 = 0.833 \text{ J/cm}^2$ . The number of pulses for each energy fluence, were varied to 50, 100, 200 and 400. Following laser processing, the samples were examined with scanning electron microscopy and surface sensitive Raman spectroscopy. The depth was measured using a Dektak diamond profilometer, and the cross-sectional area of the laser-machined region was calculated from the SEM micrographs. The nanosecond laser machining was conducted at Iowa State University using Lambda Physik's 110 Excimer laser at 248 nm.

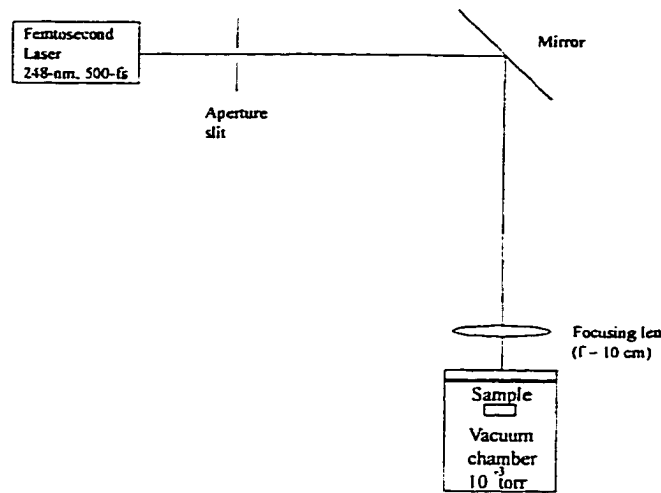


Figure 3. Experimental setup for the 248 nm, 500 fs diamond ablation studies

### *Results*

SEM analysis of femtosecond-pulsed, laser-machined surfaces revealed an absence of signs of physical degradation such as cracking, particulate, or recast layers which are common in long-pulsed lasers. Figure 4 presents a set of SEM images of 500-fs pulsed laser machined holes of CVD-diamond at different energy fluences for 400 pulses. Cross-sectional area increased slightly with increased energy fluence. SEM analysis further revealed that the lowest fluence provided a surface that has undergone relatively clean ablation, leading to sharp interfaces and little thermal damage. In the case of samples ablated near threshold fluence, the grain structure and the voids, which are the measures of thermal damage, remained the same as in the original substrate.

Figure 5 show the Raman spectra of pristine and 500-fs laser-machined regions of single crystal diamond. The negligible shift in the position and width of the single crystal diamond peak at  $1332\text{ cm}^{-1}$  indicate the very strong chemical cleanness of 500-fs laser machining. It is also seen (Figure 5) that there is no evidence of graphite or amorphous carbon. In contrast, Figure 2 shows that the 23-ns laser machining created non-diamond carbon phases, which are very

detrimental to sensitive electronic applications. Thus, the 500-fs laser does not instigate the phase transition in diamond. This phase transition may be attributed to the extended heating of the diamond by the 23-ns laser and to the transient resonant reaction below the threshold energy fluence by the 500-fs laser.

### *Discussion*

Figure 6 illustrates the effect of pulse width on the etch depth per pulse. The threshold fluence was  $0.8 \text{ J/cm}^2$  for both fs- and ns-lasers. Threshold energy fluence ranged from 0.8 to  $2.3 \text{ J/cm}^2$ , with a minimum value of  $0.8 \text{ J/cm}^2$ , for ns-lasers, and was almost constant at  $0.8 \text{ J/cm}^2$  for the fs-laser indicating, that it is a stochastic quantity for the ns-laser. As long as other conditions remain unchanged, the fs-laser should provide a lower energy threshold than the ns-laser. In this case, the difference could be due to the spot size variations (note that the ns laser had a larger spot size, which gives rise to lesser heat dissipation) and to phase transition of diamond to graphite, in addition to the effect of pulse width. However, as the fluence increased, the 500-fs laser produced a higher material removal rate than the 23-ns laser. The largest fluence reported for the fs-laser was  $6.43 \text{ J/cm}^2$ , which yielded a material removal rate of  $50 \text{ nm/pulse}$ . The corresponding depth per pulse for the ns-laser was  $30 \text{ nm}$ , approximately 60% of that of the fs-laser. It is interesting to note that the depth per pulse at  $20 \text{ J/cm}^2$  for the ns-laser was only 20% more than that of fs-laser at  $6.4 \text{ J/cm}^2$ .

Konov et al.<sup>5</sup> reported similar results for diamond-like carbon films subjected to 0.8-ns laser and 15-ns laser irradiation. Figure 7, reproduced from the work of Konov et al's, demonstrates that the depth per pulse increases with a decrease in pulse width. A notable difference from our results is that the threshold energy fluence also increased with a decrease in pulse width. As can be seen in Figure 7, the ablation threshold for 0.8-ns pulses was about  $0.3 \text{ J/cm}^2$ , or only

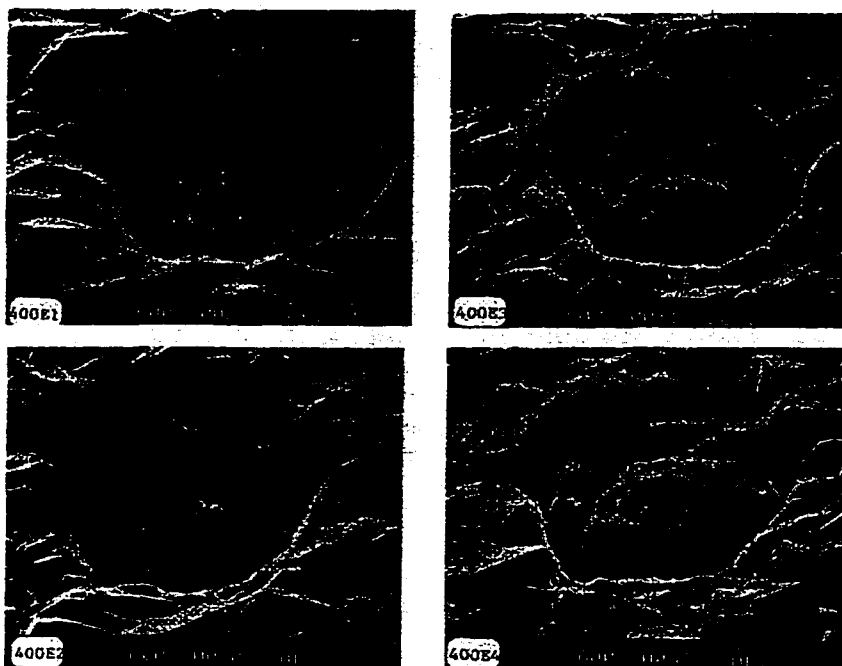


Figure 4. SEM images of CVD diamond ablated using 400 pulses of 248 nm and 500 fs pulses with fluences of  $0.8 \text{ J/cm}^2$  (400E4),  $2.86 \text{ J/cm}^2$  (400E3),  $4.44 \text{ J/cm}^2$  (400E2), and  $6.43 \text{ J/cm}^2$  (400E1)

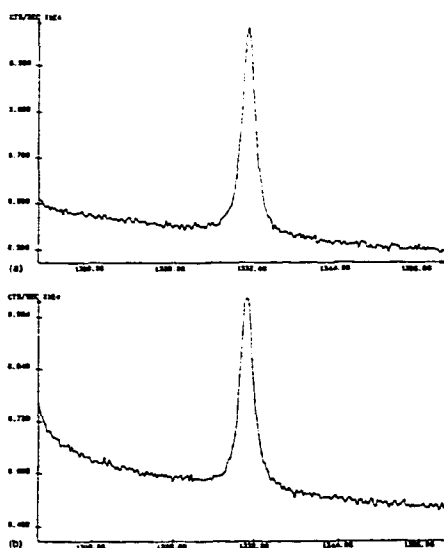


Figure 5. (a) Raman spectra of the surface of untreated single crystal diamond. (b) Raman spectra of a hole ablated in single crystal diamond using 10 248 nm, 500 fs pulses at  $6.43 \text{ J/cm}^2$

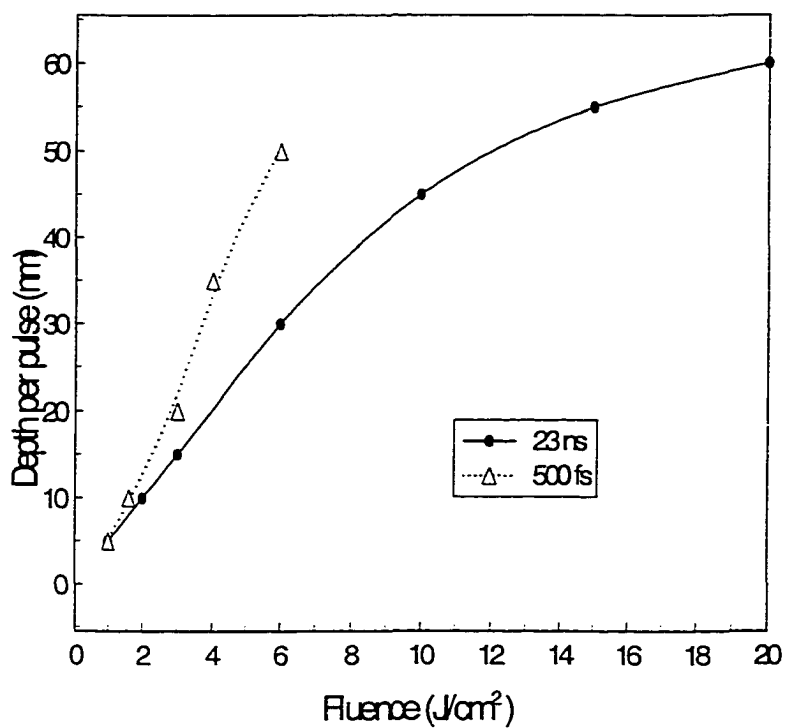


Figure 6. Ablation depth per pulse vs. fluence for 500 fs and 23 ns pulses at 248 nm

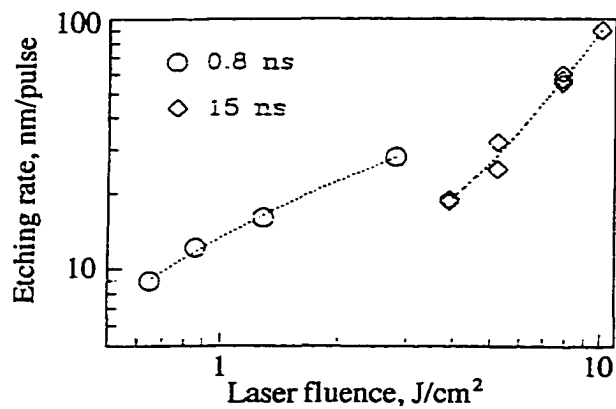


Figure 7. Experimental data from Konov et al. (see Ref. 5) showing the relation between threshold fluence energy, pulse width and depth per pulse at 248 nm

one-tenth of the  $3 \text{ J/cm}^2$  threshold for 15-ns pulses.

The effectiveness of femtosecond pulses may be explained by their larger absorption depth-to-thermal diffusion distance ratios. The absorption depth for diamond is typically about  $10^{-3}$  cm, which is much larger than the thermal diffusion distance of  $5 \times 10^{-6}$  cm for the 500-fs pulse. In contrast, the thermal diffusion distance is only  $2 \times 10^{-2}$  cm for the 23-ns pulse. As a result, heat is deposited in a thin layer and the evaporation temperature can be reached at lower energy fluence. It is important to emphasize that evaporation occurs after the fs pulse ceases and that the energy is supplied to the carriers in less time than is necessary for the energy exchange with the lattice. Thus, fs pulses create an extremely hot carrier gas on a cold substrate, and subsequent energy transfer to the phonons occurs after the fs pulse. Reflective loss due to plasma formation is ruled out in view of the shorter time frame. However, even if plasma develops, it will be thin and optically transparent.

It appears that the 23-ns data asymptotically approach a maximum depth per pulse, whereas the rate of increase of the 500-fs pulsed laser does not appear to slow as dramatically, which suggests the possibility of attaining higher ablation rates.

### *Conclusion*

Ultrashort pulsed laser ablation of diamond allows for ablation of diamond with a great reduction in undesirable changes in the material's surface structure. Characterization of the surface with Raman spectroscopy and SEM analysis clearly demonstrated a reduction of thermally induced changes, which include a lack of non-diamond carbon or recast layers. The mechanisms of ns-laser material damage are stochastic in nature, whereas the effects of ultrashort pulsed ablation are consistent and predictable, yielding more precise ablation

thresholds and materials effects. Following is a comparison of ns-laser and fs-laser effects on diamond machining.

Laser interaction time: For ns lasers, the interaction time was  $10^{-9}$  seconds, which is much longer than the free time between atomic lattice collisions ( $10^{-11}$ - $10^{-13}$ seconds); thus the diamond is heating while absorbing energy. With fs lasers, this time is  $10^{-15}$  seconds, a much shorter time than the free time between lattice collisions. Therefore, the surrounding material should be cool while the area under the laser beam is absorbing energy.

Laser induced plasma formation: For ns lasers, the plasma forms during the laser pulse, resulting in secondary ionization of the plasma and heating of the workpiece atomic lattice. With fs lasers, the plasma forms only after the end of the laser pulse; thus plasma effects should be negligible.

Controlled Processing: With fs lasers, the laser-induced absorption is resonant with the lattice, and hence the process is well controlled and homogeneous.

Phase Transition: Resonant transient reaction below threshold energy fluence did not cause the phase transition of diamond to non-diamond carbon.

The benefits that use of ultrashort pulsed lasers offers with respect to surface finish and purity of the ablated surface of diamond make it an attractive alternative to longer pulsed ablation methods. Improved material removal rates (per unit time, not per pulse) should be accomplished by using a higher frequency of pulses at the ablation threshold. Thus because the pulses are shorter and less energetic, there will be little increase of thermal effects with increases in average power. This is especially true in diamond, which has a thermal conductivity approximately 4 times that of copper. Such advances will lead to greater efficiency and precision of spatial structures ablated in diamond.

## References

1. P. A. Molian, and A. P. Malshe, "Femtosecond laser processing of CVD-diamond," *Proceedings of the Applied Diamond Conference 1995, 3rd International Conference on the Applications of Diamond Films and Related Materials*, edited by A. Feldman (NIST, Gaithersburg, MD, 1996).
2. Molian, P. A., R. Windholz, and A. P. Malshe, "Femtosecond laser-diamond interactions for laser machining applications," *Proceedings of the 2nd International Conference on Beam Processing of Advanced Materials*, American Society for Metals, Feb. 1996, edited by J. Singh, S. M. Copley, and J. Mazumder (ASM International, Materials Park, Ohio, 1996) pp. 199-206.
3. R. Windholz, , and P. A. Molian, "Nanosecond pulsed excimer laser machining of CVD diamond and HOPG graphite, part I: an experimental investigation," *J. Mater. Sci.* **32**, 4295-4301 (1997).
4. R. Windholz, and P. A. Molian, "Nanosecond pulsed excimer laser machining of CVD diamond and HOPG graphite, part II: Analysis and modeling," *J. Mater. Sci.*, (in Press).
5. V. I. Konov, V. G. Ralchenko, S. M. Pimenov, A. A. Smolin, and T. V. Kononenko, "Laser microprocessing of diamond and diamond-like films," *Proc. SPIE* **2045**, 184-192 (1994).
6. C. P. Christensen, "Micromachining of diamond substrates with waveguide excimer lasers," *Proc. SPIE* **2062**, 14-21 (1994).
7. P. Tosin, , A. Blatter, and W. Luthy, "Laser-induced surface structures on diamond films," *J. Appl. Phys.* **78**, 3797-3800 (1995).
8. D. H. Reitze, H. Ahn, and M. C. Downer, "Optical properties of liquid carbon measured by femtosecond spectroscopy," *Phys. Rev. B* **45**, 2677-2693 (1992).
9. E. N. Glezer, , L. Huang, , Y. Siegal, J. P. Callan, , and E. Mazur, "Phase transitions induced by femtosecond pulses," *Mater. Res. Soc. Symp. Proc.* **397**, 3-20 (1996).
10. G. Galli, R. Martin, R. Car, and M. Parrinello, "Ab initio calculation of properties of carbon in the amorphous and liquid states," *Phys. Rev. B* **42**, 7470-7482 (1990).

## CHAPTER 5. MOLECULAR DYNAMICS MODELING OF ULTRASHORT PULSED LASER ABLATION OF SINGLE CRYSTAL DIAMOND

A paper published in the ICALEO 1998 proceedings (1998)<sup>a</sup>

M. D. Shirk, P. A. Molian, C. Z. Wang, A. Ozkan, and A. P. Malshe

### *Abstract*

Ultrashort pulsed ( $\rho < 500$ -fs) laser ablation of diamond has been shown to produce chemically cleaner surfaces than ablation with longer, ns-pulsed lasers. To investigate this phenomenon, the process was modeled in two steps. A finite difference two-temperature model of the electrons and ions was developed to obtain accurate predictions of the temperature profiles during ablation. Tight-binding molecular dynamics modeling was then used to investigate the atomistic events that occur under conditions of both ultrashort and long pulsed ablation. In most pulsed lasers, energy is delivered in a time much longer than the electron-lattice equilibration time, which is on the order of 1-ps. Ultrashort pulses create highly excited electrons that do not have time to transfer energy to the lattice during the energy delivery. Therefore, the energy is highly concentrated within the electrons of a small region of the material. This alters the ablative mechanism, producing very clean ablated surfaces.

---

<sup>a</sup>. Proceedings of the Laser Materials Processing Conference, 85 (1998) p. 38-43, published by the Laser Institute of America

## *Introduction*

Diamond is used industrially in many applications, ranging from cutting tools to thermal spreaders in multichip modules. It is valued for its hardness, its electrical insulating properties, and its thermal conductivity. Developing processes capable of removing material precisely without significantly altering the properties of the diamond surface is desirable. Nanosecond pulsed lasers have been shown to create undesirable phases of carbon on the surface<sup>1,2</sup>. Recent investigations have shown that ultrashort pulsed laser ablation is capable of generating structurally pure diamond surfaces<sup>3</sup>.

Modeling of ultrashort pulsed laser irradiation using a two-temperature finite difference model<sup>4,5,6</sup> has been carried out previously for metals and semiconductors. The following equations describe the thermal transport for the electrons and the lattice.  $C_e$  and  $C_i$  are the electron and lattice heat capacities, respectively.  $\kappa_e$  and  $\kappa_i$  are the thermal conductivities,  $T_e$  and  $T_i$  are the electron and lattice temperatures in Kelvin, and  $G(T_e, T_i)$  is the function describing the transfer of energy between the electrons and the lattice.

$$C_e \frac{\delta T_e}{\delta t} = \frac{\delta}{\delta x} \left( \kappa_e \frac{\delta T_e}{\delta x} \right) - G(T_e, T_i) \quad (1)$$

$$C_i \frac{\delta T_i}{\delta t} = \frac{\delta}{\delta x} \left( \kappa_i \frac{\delta T_i}{\delta x} \right) + G(T_e, T_i) \quad (2)$$

This model shows that the lattices do not reach ablative temperatures until well after the pulse energy has been delivered. The temperature profiles in the material are very steep, which reduces collateral effects from thermal energy.

Although the temperature profiles give insight into the physical environment in the material, they do not provide an understanding of the actual mechanisms of ablation. To achieve a better understanding of the atomistic movements, tight-binding molecular dynamics has been used to

investigate the differences among the different pulse length lasers. Tight-binding molecular dynamics has been proven to be a computationally accurate model for carbon<sup>7</sup>. It is capable of handling electrons at a different state of excitation than the lattice. With currently available computation resources, it is practical to model several hundred atoms for a few picoseconds.

### *Finite difference model*

A finite-difference model was coded to predict electron and lattice temperatures under ultrashort pulsed laser ablation. The model uses equations 1 and 2, and it assumes that the electrons at the surface are the sole absorbers of laser energy. This is a reasonable assumption, as there is a large increase in non-linear absorption at the intensities present in ultrashort pulses because of multiphoton absorption and electron avalanche. After the surface electrons have absorbed the laser energy, it is then transferred into the material by diffusion within the electron gas, transfer from the electrons to the lattice, and thermal diffusion between the lattice points. The model assumes an infinite solid by setting the innermost node within the solid to be held at initial temperatures. There is strong evidence that this is an accurate assumption with ultrashort pulsed lasers. One example is work performed by Stuart et al.<sup>8</sup> on laser drilling of teeth. With Q-switched nanosecond pulsed lasers, the temperature of the tooth rose significantly, whereas the temperature of the tooth rose less than 2 degrees during ultrashort pulsed drilling.

The two dimensions of the simulation are spatial and temporal, and extreme temperature gradients are observed in each dimension. After the pulse has ceased, the electron temperatures fall as energy is conducted into the sample by diffusion and transferred to the lattice. Because of the short time scale of the pulse, the lattice does not approach temperatures required for sublimation (carbon does not exhibit a stable liquid phase at atmospheric pressure). Figure 1

shows an example of the predicted temperature profiles after 100 fs in diamond exposed to a 100 fs,  $1 \times 10^{18}$  W/m<sup>2</sup> pulse.

### *Tight-binding molecular dynamics model*

Tight-binding molecular dynamics has been performed to simulate the conditions of both ultrashort pulses and longer pulses. The model shows some fundamental differences between the way the material reacts to the energy delivered by the two different pulse regimes, one using pulses much greater than 1-ps and the other using ultrashort pulses, which are less than 1-ps. Simulations performed on a 288 atom model of a diamond (111) surface show that the way surfaces evolve differs greatly during the different ablation conditions.

Under ultrashort pulsed conditions, the electron temperature was set at 15,000 K and the lattice temperature was set at 300 K. As the simulation progressed, the carbon atoms underwent

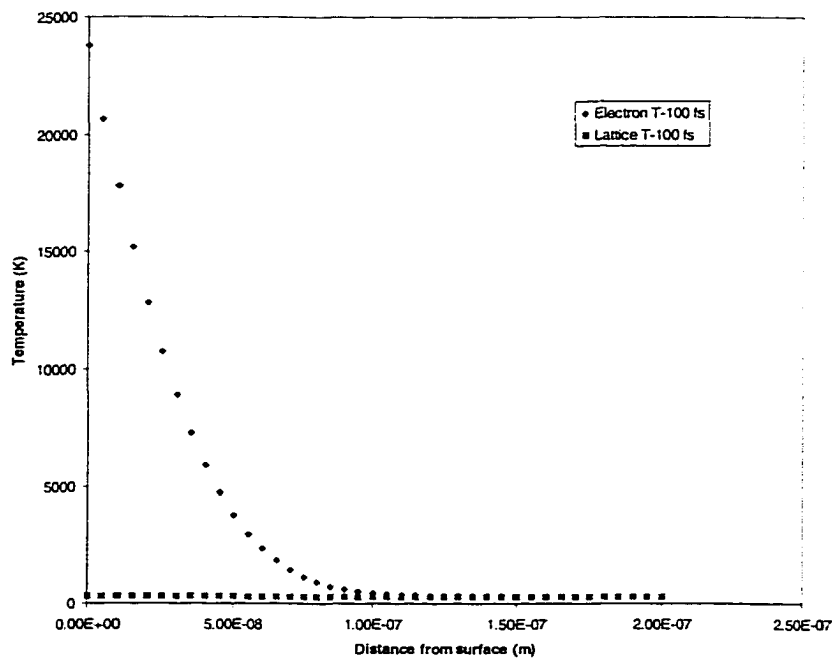


Figure 1. A plot of temperature profiles for a first order 1-D simulation of the electrons and lattice of diamond during after 100-fs laser ablation.

a phase transition from the tetrahedrally bonded lattice to planar graphite sheets. This transition progressively moved in from the surface over the time scale of the simulation. The transition is very fast, lasting less than 500-fs for the first three layers of a surface. Figure 2 shows snapshots at 0, 100, 200, 300, 400, and 500-fs, during which time the top and bottom surfaces (z-axis) become trigonally coordinated graphite sheets. The periodic boundary conditions connect the atoms at the edges of the x- and y-axis. It is evident from the simulation that the graphitization proceeds layer by layer, indicating that the mechanism for the removal of material is a rapid conversion to graphite, followed by sublimation.

Conditions simulating longer pulsed laser ablation set the electrons and lattice at the same temperature. Longer pulsed lasers have much lower intensity, and thermal diffusion becomes significant at longer times. These factors keep the temperatures reached in the material lower

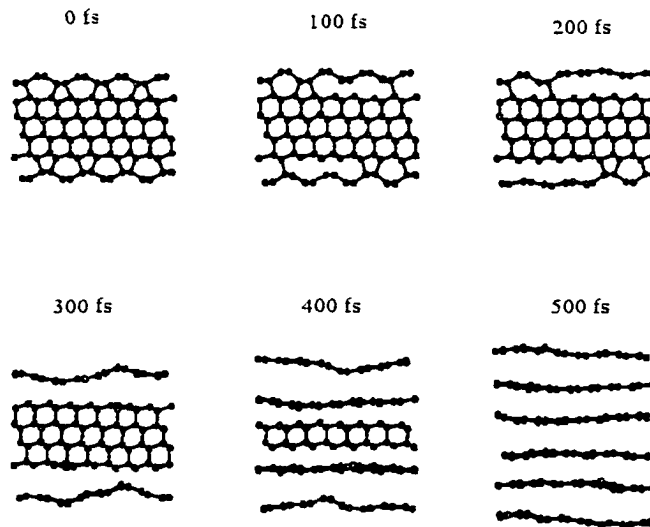


Figure 2. Results from a simulation using ultrashort pulsed conditions, electrons at 15,000 K, lattice at 300 K.

than those in the ultrashort pulsed case. Figure 3 shows the same (111) diamond surface at 2700 K for both electrons and lattice. The transitions that take place are much slower than those that occur during ultrashort pulsed irradiation, and the layer-by-layer transformation is not present. The conversion is much more penetrating. During ablation, the lattice distortions will propagate beyond the ablated region, yielding a surface with non-diamond carbon phases. Simulations indicate that the diamond structure is stable below 2500 K.

These two simulations demonstrate the differences between the two different mechanisms of material removal. For the ultrashort pulsed case, excitation of the electrons leads to disruption of the bonding within the material and subsequent change from  $sp^3$  to  $sp^2$  hybridization. Slower transitions occur with the thermal processes associated with longer pulses. Kinetic energy causes the bonds to stretch and break. This creates a disorderly and penetrating change of phase.

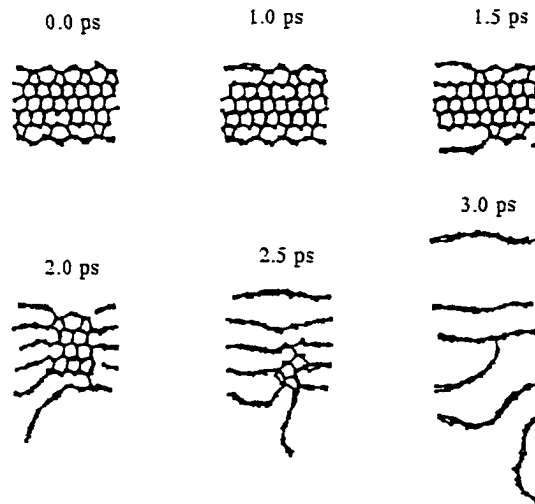


Figure 3. Results from a simulation with the electrons and lattice at 2700 K, simulating longer pulsed laser ablation.

### *Discussion*

The experimental evidence regarding improved diamond processing has shown that diamond exposed to ultrashort pulses is cleaner structurally than that exposed to longer pulses. The strongest evidence for this comes from Raman scattering spectra taken from diamond ablated with the two different classes of pulse. Windholz and Molian<sup>1</sup> and Pimenov et al.<sup>2</sup> both showed that, in Raman spectra of diamond exposed to ns-pulses, the sharp peak at  $1332\text{ cm}^{-1}$  is no longer present after ablation, and peaks for diamond-like carbon and graphite appeared. Pimenov et al. reported that the layer of non-diamond carbon was less than 200 nm in thickness. Shirk et al.<sup>3</sup> showed that the non-diamond carbon phases could be avoided by using a 248 nm 500 fs excimer:dye laser. When a single crystal diamond was ablated with the ultrashort pulsed laser, the Raman spectra exhibited the strong  $1332\text{ cm}^{-1}$  peak.

The experimental evidence, along with the modeling data, confirm that the mechanisms of ablation for ultrashort pulsed lasers are far different from the more thermally dominated mechanisms for pulses in excess of several picoseconds. The physical properties of diamond and graphite are very different; diamond shows excellent thermal conductivity and is a very strong electrical insulator, whereas graphite is a semi-metal and has relatively poor thermal conductivity. This is important, as the rapid conversion to planar graphitic sheets with ultrashort pulses works to isolate the laser energy at the surface and remove the newly formed graphite sheets. The slow thermal mechanisms generated by longer pulses allow the material to conduct laser energy away from the ablated material. This causes undesirable phase changes on the freshly exposed surface and reduces the efficiency of the ablation process. At equivalent energy densities, the ultrashort pulsed laser removes more material per pulse, as shown in Figure 4,

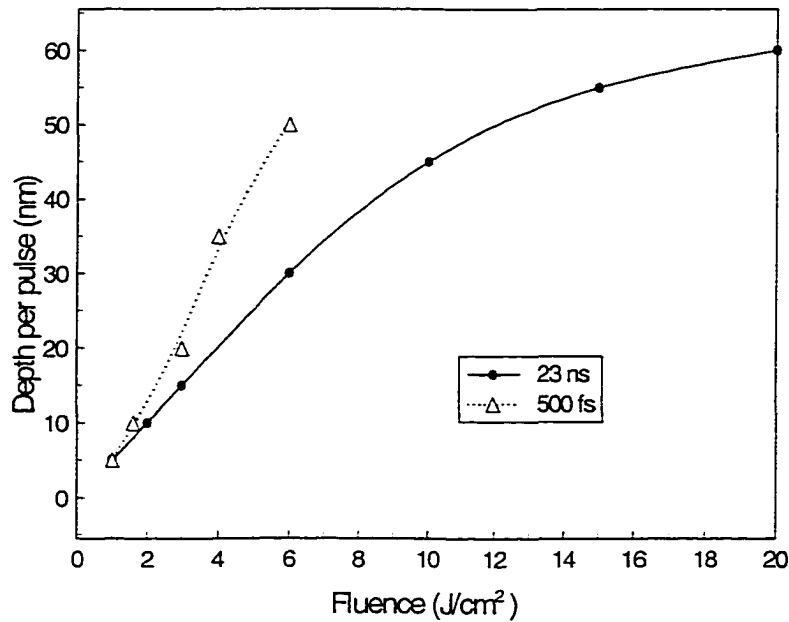


Figure 4. Ablation depth versus fluence for 23-ns and 500-fs 248-nm lasers on CVD diamond. taken from Shirk et al.<sup>3</sup>. The ultrashort pulsed laser deposits its energy efficiently in the material being removed. No significant diffusion of thermal energy to surrounding material is observed.

### *Conclusion*

Ultrashort pulsed lasers significantly improve the quality achievable in removing material from a diamond surface. This is primarily due to absence of significant phase changes that adversely affect optical, electrical, structural, and thermal properties of the surface. This improvement should eliminate the post-processing currently necessary to ensure structural purity of a surface. Ultrashort pulsed processing also improves the precision with which holes and other structures may be created, because thermal diffusion into the bulk does not occur, again making ultrashort pulsed lasers superior to longer pulsed lasers.

### *Acknowledgements*

The authors thank the National Science Foundation (DMI 9622518) and the Iowa Center for Emerging Manufacturing Technologies for their support of this research. We also thank Professor Joseph Prusa for his significant help with the finite difference model.

### *References*

1. Windholz, R., and P. A. Molian. "Nanosecond pulsed excimer laser machining of CVD diamond and HOPG graphite, part I: an experimental investigation." Journal of Materials Science, Vol. 32, (1997) pp. 4295-4301.
2. Pimenov, S. M., A. A. Smolin, V. G. Ralchenko, and V. I. Konov, "Excimer laser processing of diamond films." Diamond Films and Technology, Vol. 2: (1993), pp. 201-214.
3. Shirk, M. D., P. A. Molian, and A. P. Malshe. "Ultrashort pulsed laser ablation of diamond." Journal of Laser Applications. Vol. 10: (April, 1998). pp. 64-70.
4. Corkum, P. B., F. Brunel, , and N. K. Sherman. "Thermal responses of metals to ultrashort-pulse laser excitation." Physical Review Letters. Vol. 61: (December, 1988). pp. 2886-2889.
5. Shermann, N. K., F. Brunel, P. B. Corkum, and F. A. Hegmann. "Transient responses of metals to ultrashort pulse excitation." Optical Engineering. Vol. 28: (October, 1989). pp. 1114-1121.
6. Pronko, P. P., P. A. VanRompay, R. K. Singh, F. Qian, D. Du, and X. Liu. "Laser induced avalanche ionization and electron-lattice heating of silicon with intense near IR femtosecond pulses", Materials Research Society Symposium Proceedings, Vol. 397: (1996) pp. 45-51.

7. Wang, C. Z., K. M. Ho, and C. T. Chan. "Structure and dynamics of liquid carbon." Physical Review B, Vol. 47: (June, 1993). pp. 14,835-14,841.
8. Stuart, B. C., M. D. Perry, M. D. Feit, L. B. Da Silva, A. M. Rubenchik, J. Neev, S. Herman, H. Nguyen, and P. Armstrong. "Femtosecond laser materials processing." Conference on Lasers and Electro-optics, Vol. 11, 1997 OSA Technical Digest Series (Optical Society of America, Washington D.C.), (1997) pp.159-160.

### *Meet the authors*

Michael Shirk is a graduate research assistant pursuing a Ph.D. in Mechanical Engineering at Iowa State University. He received his M. S. in Materials Science and Engineering from Iowa State University in December of 1996.

Palaniappa Molian is a Professor of Mechanical Engineering at Iowa State University. His research interest include materials processing and manufacturing.

Cai-Zhuang Wang is a Research Scientist with the Iowa State University Department of Physics and Ames Laboratory who specializes in Tight-binding molecular dynamics of carbon and silicon.

## CHAPTER 6. CHIRPED PULSE AMPLIFIED Ti:SAPPHIRE LASER ABLATION OF DIAMOND: MODELING AND EXPERIMENTAL VERIFICATION

A paper to be submitted to the journal Carbon

M. D. Shirk, C. Z. Wang, P. A. Molian, K. M. Ho, J. Prusa

### *Abstract*

Ultrashort pulsed laser ablation of diamond was modeled with a combination of a finite-difference heat transfer model and tight-binding molecular dynamics to achieve a firm understanding of the ablation process. A discussion on the theory used to calculate the important electronic properties is presented, and then applied to the finite-difference model to predict the temperature distribution within the electrons in the material. The data from the tight-binding molecular dynamics are used to predict the electron temperature threshold for atomic movement and ablation in diamond. This information was used to predict the thresholds for ablation and heat affected zones dimensions resulting from ultrashort pulsed ablation. The model data was validated using experimental data obtained using a CPA Ti:Sapphire laser.

### *Introduction*

Diamond fabrication has been an ongoing effort for centuries, and has grown from art to science. Initial processes were used to make gemstones. Ralchenko and Pimenov<sup>1</sup>, recently reviewed the processes needed to shape diamond: cutting, cleaving, sawing, polishing, bruiting, and grinding. It should be noted that most of these processes have not changed significantly over the years.

Cleaving is the simplest of these processes. Traditionally a diamond stone is examined and marked with India ink and then a thin mark is scribed along the ink with a sharp diamond tip. The stone is then mounted in a resin and then struck with a dull iron rod that is inserted in the

scribed groove. In general it is limited to the (111) plane of diamond, however on rare occasions other planes (low surface energy planes) can be formed. The advantage of this method is that no material is lost during the process.

Diamond sawing is performed with an iron or bronze wheel that has been charged with diamond abrasive powder. This process is extremely slow and can be only perform along (110) and (100) planes. Therefore it is not possible to use this method to saw polycrystalline diamond, as is formed by chemical vapor deposition (CVD).

Polishing of diamond can be accomplished both mechanically and chemically. Mechanical polishing of diamond is usually performed on an iron wheel called a scaife charged with abrasive diamond powder. Chemical polishing is performed using iron or manganese powders that have large carbon solubility. Chemical polishing is a high temperature ( $\sim 900^{\circ}\text{C}$ ) process, and is relatively slow.

Recent developments using alternative fabrication methods were also discussed to form polycrystalline diamond.<sup>1</sup> These are electrical discharge machining (EDM) and laser machining. Both methods can be used to create fine three-dimensional structures on diamond.

EDM uses a two-electrode system, where one electrode is a fine wire and the other is what the workpiece is mounted on. A spark is then generated between the two, and this is what erodes the material. Since diamond is an insulator, the surface must either be converted to graphite or a metal coating must be applied in order to make it conductive. This method has been used to make dies, gears, and microdrills, among other shapes from polycrystalline diamond.

Similar work has been done using lasers, primarily Nd:YAG (1064 nm), frequency doubled Nd:YAG (532 nm), and ultraviolet excimer lasers. Lasers have the advantage of being totally non-contact. Diamond machining with a laser is usually performed in either oxygen or air,

which reduces redeposition because the carbon reacts with oxygen upon vaporization to form carbon dioxide. Diamond is transparent to wavelengths longer than 227 nm. However, diamond has defects and microvoids that increase absorption. These features grow upon laser irradiation causing wavelengths that are otherwise transmitted to be absorbed by the diamond. The fundamental Nd:YAG laser is by far the most popular laser used in the diamond industry today to polish diamond surfaces and to etch structures onto the surface. However, these processes leave some undesirable heat affected areas, which limit feature definition, adversely affect optical and electrical properties<sup>2</sup>, and limits aspect ratio of drilled holes (aspect ratio is the maximum depth of a hole divide by the diameter of the hole).

The current state-of-the-art in diamond machining is performed with nanosecond pulsed Nd:YAG and excimer lasers. Ultrashort pulsed laser ablation is new a technology that will enable the generation of microelectromechanical systems (MEMS) and other fine scale devices manufactured from diamond and other engineering materials. It will also offer significant improvements for diamond tools, optical applications (e.g. diamond windows), and electronics applications of diamond (e.g. thermal spreaders).

Diamond has a large optical band-gap, around 5.2 eV, which prevents it from readily absorbing photons below 227 nm. Therefore, a laser must create optical damage in the material before it efficiently absorbs the laser energy. This damage includes the generation of color centers and phase changes. Previous work by Shirk et al.<sup>2</sup> showed that ultrashort pulses (248 nm, 500 fs) were able to eliminate the undesirable ablation products of the longer pulses, and create chemically clean diamond surfaces. In order to investigate the differences between ultrashort pulsed laser ablation and conventional pulsed laser ablation a two-part model has been developed. First a finite-difference model was developed to predict the temperature of the electrons in diamond subjected to ultrashort pulsed ablation. The results of the finite-difference

model were then coupled with tight-binding molecular dynamic simulations to predict how diamond surfaces responded to ultrashort pulses when compared to longer pulses. An 825 nm, 120 fs chirped pulse amplified (CPA) Ti:Sapphire laser was experimentally used to study the effects of ultrashort pulses on diamond in order to verify the theoretical results, and to show that the effects are wavelength independent by comparing the new 825 nm results with previous ultrashort pulsed laser experiments on diamond that used 248 nm light.<sup>2</sup>

### *Computer model*

The computer model had two parts, the prediction of the temperatures of the electrons and lattice with the finite-difference method, and the tight-binding molecular dynamics prediction of the atomic structures on the surface. The finite-difference model considered the electrons only because the ultrashort pulses are much shorter than the electron lattice equilibration times, 100-500 fs pulses versus approximately 2 ps to achieve electronic equilibration with the lattice. The tight-binding molecular dynamics potential was chosen over other computationally simpler methods because of its ability to handle electronic states under excited conditions. Other potentials such as those by Leonard-Jones are often used for covalent solids, but they are inadequate for simulations of ultrashort pulsed ablation because the potentials are not sophisticated enough to model the extreme electronic excitations.

### **Finite-difference model**

The finite-difference model assumed that the electrons absorb all the laser energy and then transported it into the bulk by thermal conduction. A one-dimensional model was deemed adequate because a typical laser spot is on the order of 10-100  $\mu\text{m}$ , and the ablation depths are only 10-80 nm.

The differential equation that describes the heat flow in a one dimensional case is shown in Equation 1:

$$C_v \frac{\partial T}{\partial t} = \frac{\partial}{\partial x} K \frac{\partial T}{\partial x} + A(t, x) \quad (1)$$

The left side of the equation is the time dependence of the temperature, and the right side governs the spatial variations. The  $A(t, x)$  term is the intensity dependent absorption of energy. Equation (1) was solved using a finite-differencing scheme. This method breaks the material into sections, or nodes, that are used to calculate the heat flow over finite time steps. For this model it was assumed that the surface node absorbed all energy. The thermal conductivity of diamond is the highest of any known material. However, diamond's thermal conductivity is dominated by phonon modes. The commonly tabulated heat capacities and thermal conductivity are unsuitable for this application since they are not related to the electrons, as they would be for a metal such as copper. Therefore, the thermal conductivity and heat capacity of the electrons had to be modeled using methods from solid-state physics. A good conceptual starting point for many electronic models is the Drude model, which assumes a free electron gas. With these assumptions all of the electrons in the material conduct electricity and heat. A more accurate model is the free electron model that uses Fermi-Dirac statistics. In this model only the electrons near the Fermi surface are able to conduct energy. The Fermi surface is defined as the highest occupied level when the material is at absolute zero. Metals have empty electronic states just above the filled states and this make the free electron model highly accurate for modeling them. Diamond does not behave this way as the next available electron states are over 5 eV above the highest filled states.<sup>1</sup> In order to deal with this, a theoretically calculated density (DOS) of states was used to determine the electron distribution, and above the maximum energy of this distribution (around 14 eV), the electron states are assumed to be free-electron-like. The equation that defines the number of occupied states is shown in Equation (2):

$$n = \int_{-\infty}^{\infty} p(\epsilon) \cdot f(\epsilon) d\epsilon \quad (2)$$

Here  $n$  is the number of occupied states,  $\epsilon$  is the energy of a state,  $f(\epsilon)$  is the Fermi function, and  $p(\epsilon)$  is the function that describes the density of states. The Fermi function is shown in Equation (3):

$$f(\epsilon) = \frac{1}{1 + e^{\left(\frac{\epsilon - \mu}{k_b \cdot T}\right)}} \quad (3)$$

Its behavior is such that the function equals one when  $\epsilon$  is significantly below the Fermi energy, and zero when  $\epsilon$  is significantly above the Fermi energy. The  $k_b$  is Boltzmann's constant, which relates temperature to energy in the system. The  $\mu$  is the chemical potential of the system. Near the Fermi energy (within around  $k_b T$ ) the function is some fraction less than one, and is indicative of the probability of occupancy. A material always has the same number of states  $n$  (unless electrons are lost in excitation, reducing their population), therefore  $n$  is used as a constant in these simulations. For diamond this number was determined by calculating the number of valence electrons per volume. This was performed by taking the product of the number of valence electrons, four, and the number of atoms per unit cell, eight, and dividing by the volume of the unit cell, a cube 0.356 nm on a side.

The first step to calculate the heat capacity is to integrate Equation (2) over all energy levels and solve for the chemical potential ( $\mu$ ) to keep  $n$  constant. This  $\mu$  was then used to solve for the total energy of the electrons at a given temperature. Equation (4) shows the energy of the electrons  $u$ :

$$u = \int_{-\infty}^{\infty} \varepsilon \cdot p(\varepsilon) \cdot f(\varepsilon) \, d\varepsilon \quad (4)$$

This expression was then solved for the temperatures within the expected experimental range, and numerical differentiation was then used to generate a table of constant volume heat capacities ( $C_v$ ). The calculation of the thermal conductivity ( $K$ ) was then simply performed by the relationship in Equation (5):

$$K = \frac{1}{3} C_v v l \quad (5)$$

where  $v$  is the electron velocity, a quantity determined from the band structure of diamond, and  $l$  is the mean-free-path length of an electron, that is the distance that an electron can travel (on average) before undergoing a scattering event. For CVD diamond the maximum value for  $l$  would be the size of the grains in the material, as electrons scatter at grain boundaries. For single crystal diamond this value could be significantly larger. It is also a function of temperature and defect sites. For these simulations the value used was 50  $\mu\text{m}$ , the approximate grain size of the CVD diamond used in the experiments. The average electron velocity was calculated to be  $6.0 \times 10^5$  m/s from the band structure of the conduction band of diamond by taking the numerical derivative of the conduction bands along the different crystallographic orientations and then averaging using symmetry to weight the different orientation's velocity. These properties were then used to predict the electron temperature distributions.

A preliminary step in this model was a simple integration that was written in order determine the amount of energy required to raise a typical ablation volume's electron temperatures to expected temperatures. Integrating the heat capacity over a typical ablation volume and temperature range was used to generate these results. This predicted the amount of absorbed energy required in order elevate the electrons to particular temperature, important for the

determination of ablation thresholds. A one-dimensional finite difference simulation was then constructed to solve Equation (1). The partial derivatives were replaced with difference equations which are numerical approximations of the derivatives as shown in Equation (6):

$$\Delta T_n^m = \frac{\Delta t}{C \left( \frac{T_n^m + T_n^{m-1}}{2} \right)} \left[ \left( \frac{K(T_{n+1}^{m-1}) - K(T_{n-1}^{m-1})}{2\Delta x} \right) \left( \frac{T_{n+1}^{m-1} - T_{n-1}^{m-1}}{2\Delta x} \right) + K \left( \frac{T_n^m + T_n^{m-1}}{2} \right) \left( \frac{T_{n+1}^{m-1} - 2T_n^{m-1} + T_{n-1}^{m-1}}{\Delta x^2} \right) \right] \quad (6)$$

This is simple a rearrangement of Equation (1) where both sides have been divided by the heat capacity, and the change in temperature is calculated by taking short time steps ( $\Delta t$ ). The superscript on the T is representative of time, and the subscript is the node representing the position in depth, spaced  $\Delta x$  apart. The first term within the brackets is the difference representing the product first derivative of the heat capacity times and the temperature, both with-respect-to (WRT) depth. The second term is the product of the average thermal conductivity at the node throughout the timestep and the difference representing the second derivative of the temperature WRT depth. The difference equation was solved by using iterations because it was necessary to use an accurate prediction of the final temperature to determine the average properties of the heat capacity and thermal conductivity during the time step. The heat capacity for diamond's electrons is virtually zero up to around 4,000 K, as it is impossible for diamond to thermally elevate electrons below this temperature. This made this equation extremely unstable, requiring timesteps below  $10^{-16}$  s and node distances of 10 nm, if  $\Delta t/\Delta x^2$  was large, then the model did not work.

### **Tight-binding molecular dynamics**

This method was developed as a computationally efficient means of calculating the forces on and movement of atoms in a computer simulation that explicitly incorporates the electronic states of the atoms into the calculations. For ultrashort pulsed laser ablation, this is of critical

importance, as the electrons absorb the laser light without significantly heating the lattice. This method was presented in an excellent paper by Tang et al.<sup>3</sup> TBMD has been shown to accurately model conditions which are not readily studied in a laboratory. The high pressure state of liquid carbon is one such situation that has been successfully modeled.<sup>4</sup> The input files for these simulations contained (x,y,z) coordinates for each atom in the simulation, these were generated from known structural configurations of diamond. The boundary conditions were periodic, that is the left and right, and front and back (as viewed in the figures) were viewed for the surface simulations. The top and bottom surfaces were left unbounded. For the bulk all three boundaries were treated as periodic.

### *Experimental methods*

A chirped pulse amplified (CPA) Ti:Sapphire laser (825 nm) operated at 1 kHz, with a pulse width of 120 fs, and a 12 mm diameter circular beam profile which was approximately 95% Gaussian was used to produce holes in CVD and single crystal diamond. The beam was focused onto the surface of the diamond (CVD diamond on silicon substrate, HIDECC, University of Arkansas and (111) single crystal diamond type IIA) which was mounted on a four axis micropositioner in a vacuum chamber at pressures of less than  $10^{-4}$  torr. The diameter of the spot was 100  $\mu\text{m}$  for the CVD diamond and 90  $\mu\text{m}$  for the type IIA single crystal diamond as determined by beam analysis, schematic shown in Figure 1. An electronic shutter was then used to control the exposure time and a quarter wave-plate-Brewster window combination was used to control the pulse energy. Ablated samples were then characterized using micro-Raman spectroscopy, atomic force microscopy (AFM), and scanning electron microscopy (SEM).

### *Results and Discussion*

Simulations were carried out using the heat capacities and thermal conductivities calculated using the DOS model. Figure 2 shows the modified DOS used, a version of that was tabulated

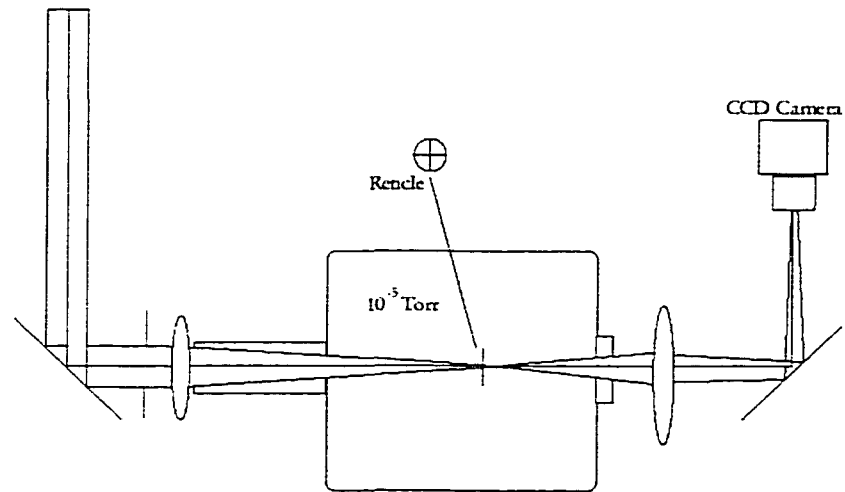


Figure 1. Beam diagnostics setup, the reticle is placed at the same place that the sample would be so that the image on the camera is identical to that used for ablation.

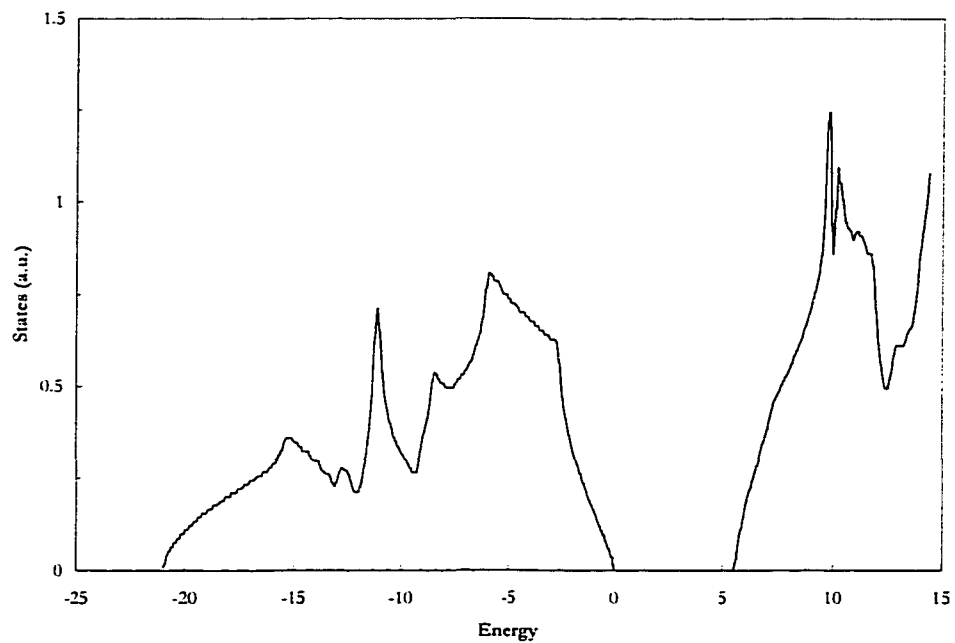


Figure 2. The modified density of states<sup>5</sup> used in this simulation, free electron conditions were assumed above 14 eV

by Papaconstatopoulos.<sup>5</sup> It was modified by artificially increasing the band gap from the calculated 4.8 eV to 5.2 eV by adding 0.4 eV to the energy of every state above 0 eV. It is well known that there is a discrepancy between the calculated and experimental band gap in diamond, therefore this modification was necessary.

Figure 3 shows values for the heat capacity up to 150,000 K. The first simulation predicts the amount of energy to heat a volume of electrons to specific temperatures, as shown in Figure 4, obtained for a 100  $\mu\text{m}$  diameter spot irradiated to a 50 nm absorption depth. The second simulation, which used the finite-difference code was performed for 100 fs pulses with an intensity of  $1.3 \times 10^{17} \text{ W/m}^2$ , an intensity equivalent to a 0.1 mJ pulse with a 100  $\mu\text{m}$  diameter spot size. The results are shown in Figure 5.

The tight-binding molecular dynamics was then used to predict that the temperature thresholds for atomic movement. These occurred at electron temperature at 15,000 K for (111) surfaces, 25,000 K for (001) surfaces, and 60,000 K for bulk diamond. It can be predicted from the finite-difference model that when these temperatures are exceeded that the material will undergo transitions that will lead to disordered carbon or ablation. Simulations were also performed to see what the actual equilibrium temperatures (that is electron and lattice temperature at the same value) were required to cause atomic movement. It was found for (111) surfaces that only 2,700 K was required and for (001) surfaces 4,000 K was required to create ablation conditions and collateral thermal degradation on diamond surfaces.

Figure 6 shows the results from animations of the TBMD simulations for the (001) surface as both the electrons and lattice are excited to 4000 K, the threshold for thermal degradation of the respective structures. Figure 7 shows a simulation of the (001) surface under electron excitation at 25,000 K, which was the threshold for atomic movement using only electronic excitation.

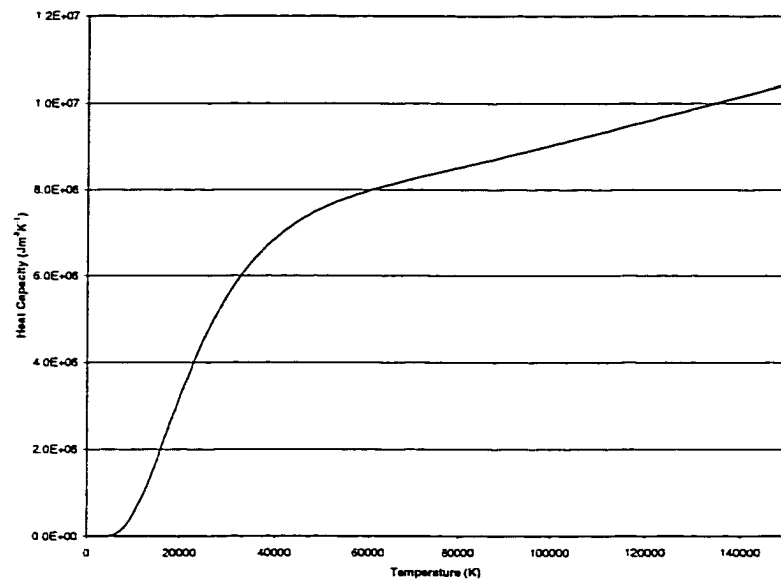


Figure 3. Calculated heat capacity for the electron gas in diamond

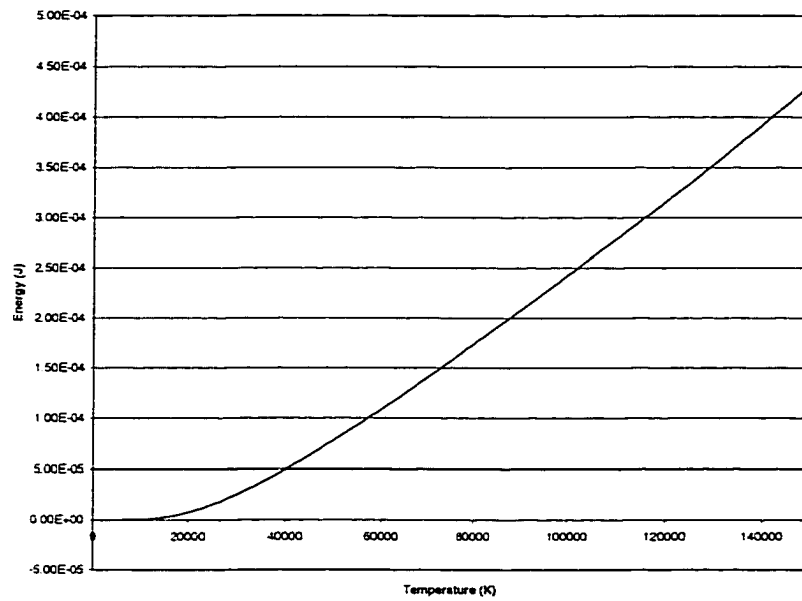


Figure 4. Electron temperature versus absorbed energy for a 100  $\mu\text{m}$  diameter, 50 nm absorption depth region, only applicable to pulse widths less than about 500 fs

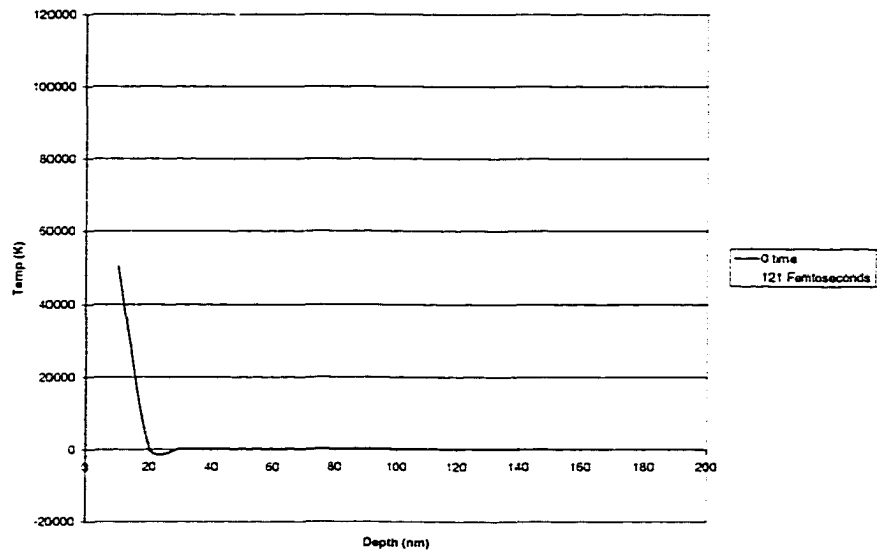


Figure 5. Results of a finite-difference calculation at  $1.3 \times 10^{17} \text{ W/cm}^2$  for a 100 fs pulse

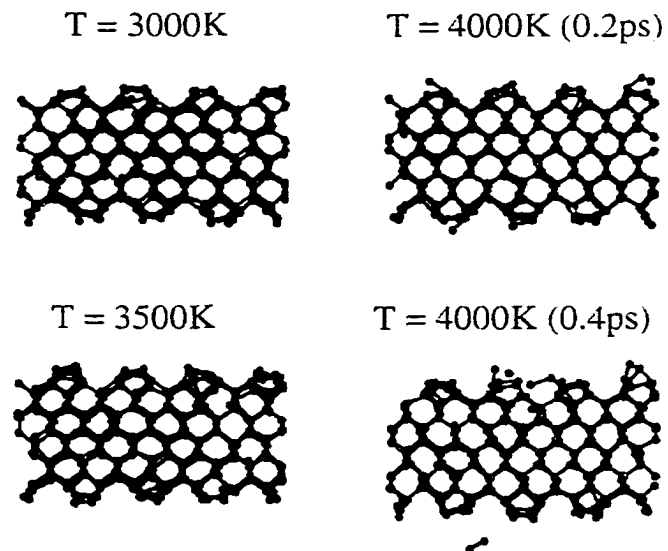


Figure 6. (001) diamond surface undergoing thermal decomposition at 4000 K

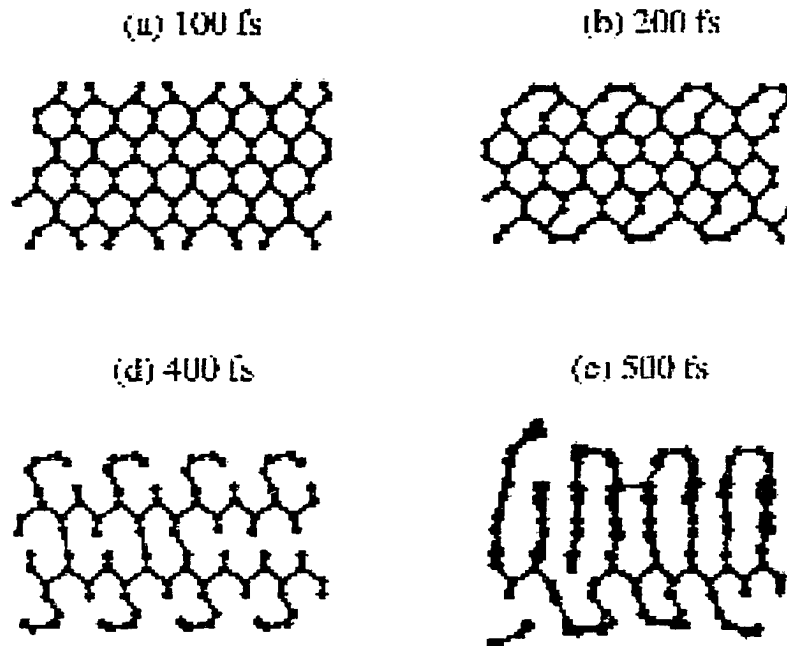


Figure 7. (001) diamond surface undergoing amorphitization at an electron temperature of 25,000 K

Figure 8 shows a simulation of a (111) surface undergoing thermal decomposition at 2700 K for both electrons and lattice. Figure 9 shows the degradation of the surface at 15,000 K electron temperature. The (111) surface can quickly convert from  $sp^3$  hybridization to  $sp^2$  hybridized graphite sheets by simply breaking 1 bond per 2 atoms and removing the pucker from the 6 membered rings, as happens extremely fast in this simulation. In the (001) surface, the same change occurs along the (111) plane, except at higher temperatures. The increased temperature is due to the fact that the planes that were converting to the graphitic sheets were not in the same plane as the surface, which caused increase restrictions on the movement of the plane, thereby increasing the energy required.

The mechanism and energies of change vary significantly due to the different stabilities of the surfaces. The (111) plane is the most easily created plane, as evidenced by it being the only cleavage plane that is possible. The (001) surface requires more energy to create. The energy

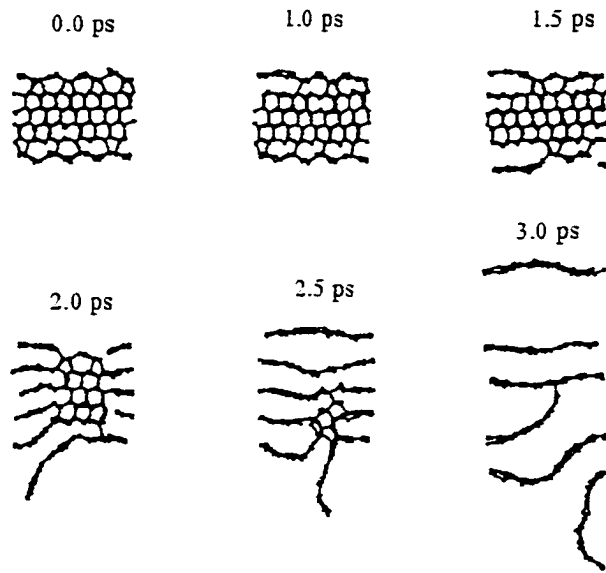


Figure 8. Thermal decomposition of a (111) surface at 2700 K

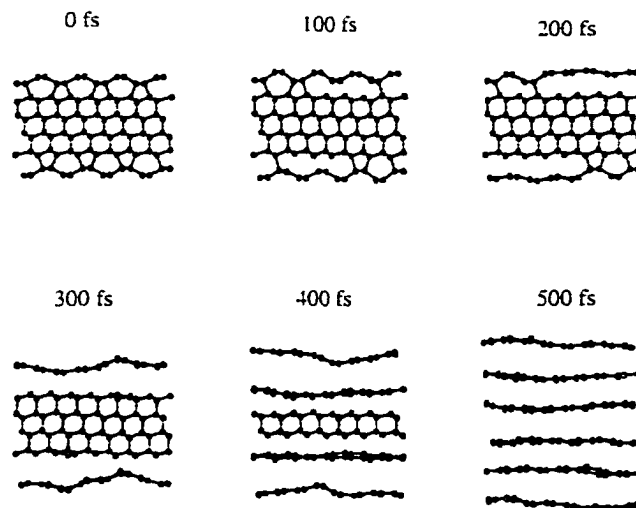


Figure 9. (111) surface undergoing graphitization at 15,000 K electron temperature

required to convert diamond to graphite is also lowest along the (111) plane, as it is only necessary to break 1 bond per two atoms on the surface to get the structure to go to the stable graphite form. When these bonds break, the 6 membered puckered rings quickly flatten leaving graphite. Since the  $\pi$  bonding between planes of graphite is rather weak, these planes are easily removed during ablation.

Finally, it was decided to determine the stability of bulk diamond with regard to electronic excitation. It was found that bulk diamond was extremely stable, and that when atomic motion occurred it required extreme temperature, 60,000 K. When this temperature was reached the structure disintegrated within 250 fs.

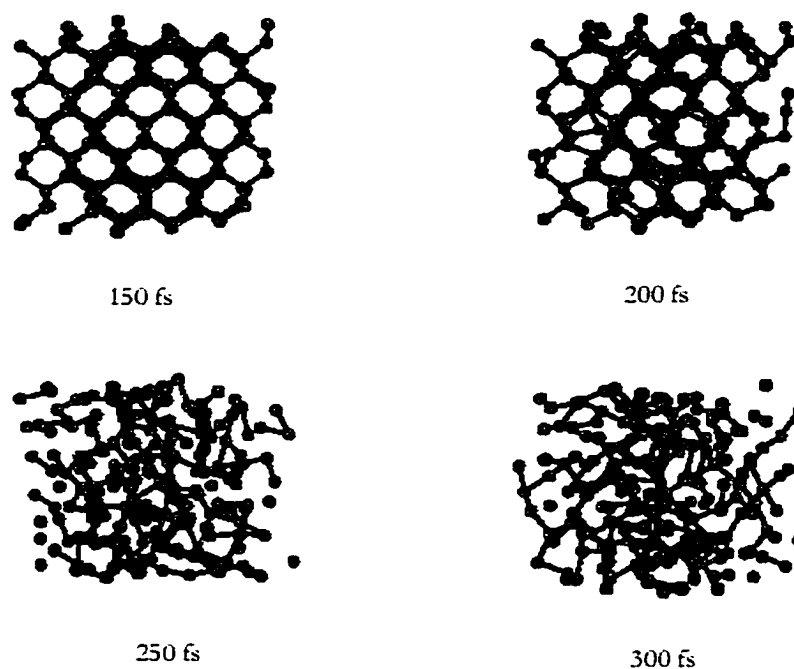


Figure 10. Bulk diamond as it undergoes severe atomic disordering at 60,000 K electron temperature

The model data is then correlated to physical experiments performed on diamond. Figure 11 is a SEM image of untreated CVD diamond. CVD diamond has a rough surface, the average size of the crystals in this image are on the order of 50  $\mu\text{m}$ . This can also be seen in Figure 12, which also includes four of the holes that were ablated in the surface. Figures 13 and 14 show higher magnification SEM images of holes drilled in CVD diamond using 120 fs pulses. Notice the fine scale features visible around the edges of the holes. This ablation was a very clean process. No recast layer, collateral damage, or other undesirable effects were observed. The same effects are true for single crystal diamond. In Figure 15, a hole ablated in single crystal diamond and characterized using AFM, shows a nearly perfect 90- $\mu\text{m}$  diameter hole. The edge of the hole is a rapid transition from the flat, pristine diamond surface to a steeply-sided, smooth-edged hole. There is absolutely no evidence of recast or collateral damage. Figure 16 shows an AFM image of a groove ablated in single-crystal type IIA diamond. This was made by slowly translating the sample as the laser ablated at 1 kHz, there is no sign of ridging from the individual pulses being slightly offset. Similar effects are observed here, however it is apparent that the base of the groove is not as smooth as the edges, a factor that would be expected due to irregularities in the beam profile. Micro-Raman show pure diamond surface, the only difference between the laser ablated surface and the untreated surface is a reduction in the intensity of the peak from 170,000 counts to around 70,000 counts. This could be attributed to the change from a flat planar surface to the slightly rougher surface within the hole. Previous studies have seen significant peak broadening and even elimination of the diamond peak from a longer pulsed laser treated surface.<sup>2,6</sup> It is clear that the ultrashort pulses create very chemically pure, defect free surfaces, as is desirable for most applications.

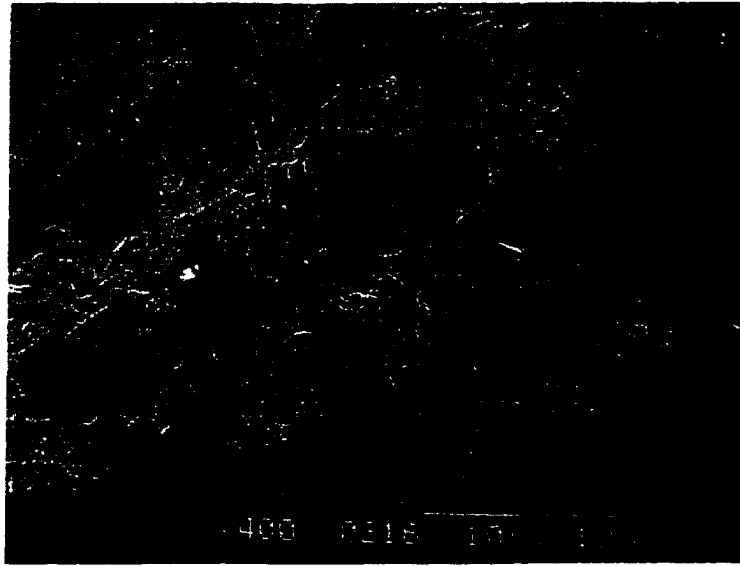


Figure 11. SEM image of untreated CVD diamond surface

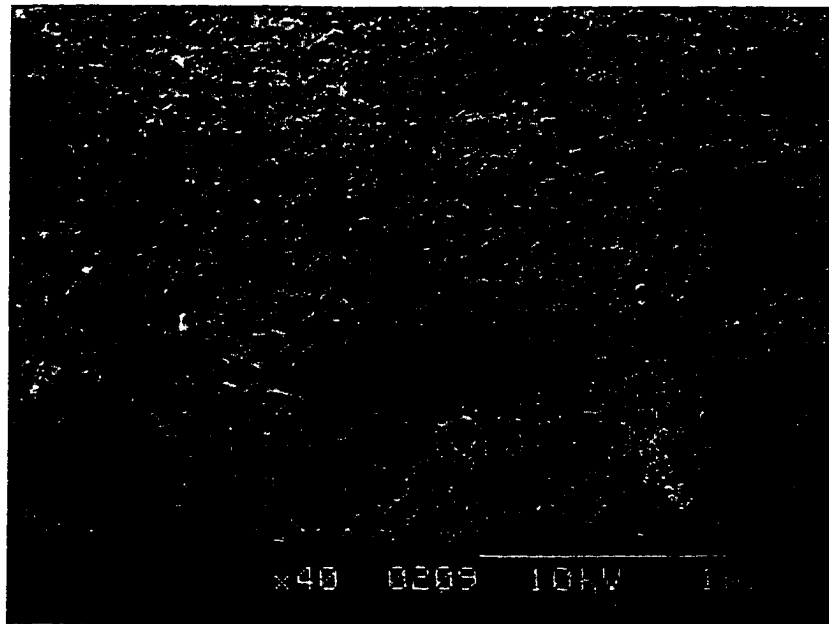


Figure 12. SEM image showing 4 holes ablated in CVD diamond with 1000 pulses, left two at 150  $\mu\text{J}/\text{pulse}$ , right two at 200  $\mu\text{J}/\text{pulse}$  using a 100  $\mu\text{m}$  focused spot size

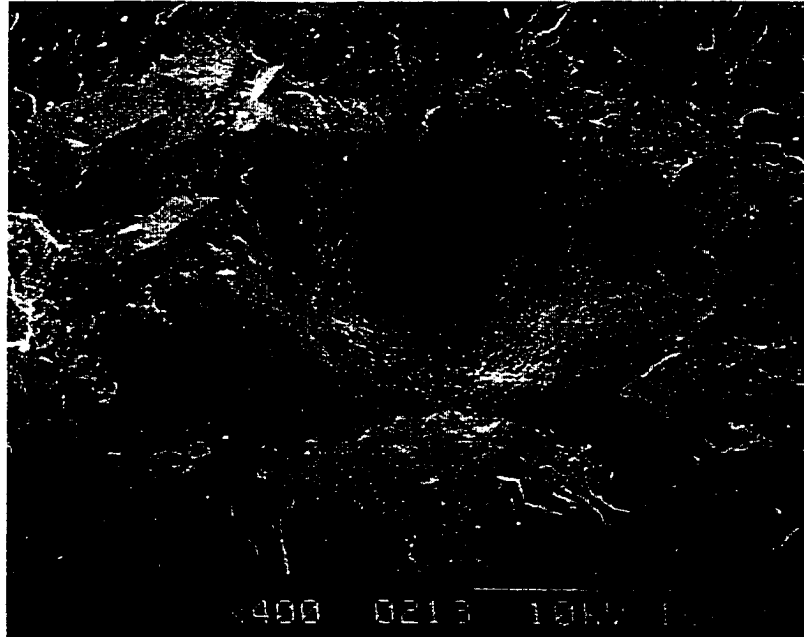


Figure 13. SEM image of a hole ablated in CVD diamond with 1000, 150  $\mu\text{J}$  pulses (100  $\mu\text{m}$  spot size)

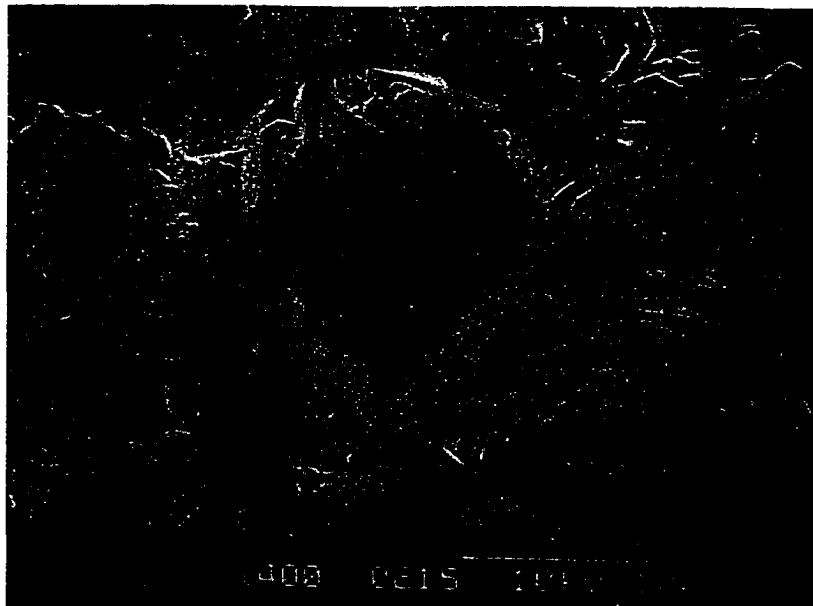


Figure 14. SEM image of a hole ablated in CVD diamond with 1000, 200  $\mu\text{J}$  pulses (100  $\mu\text{m}$  spot size)

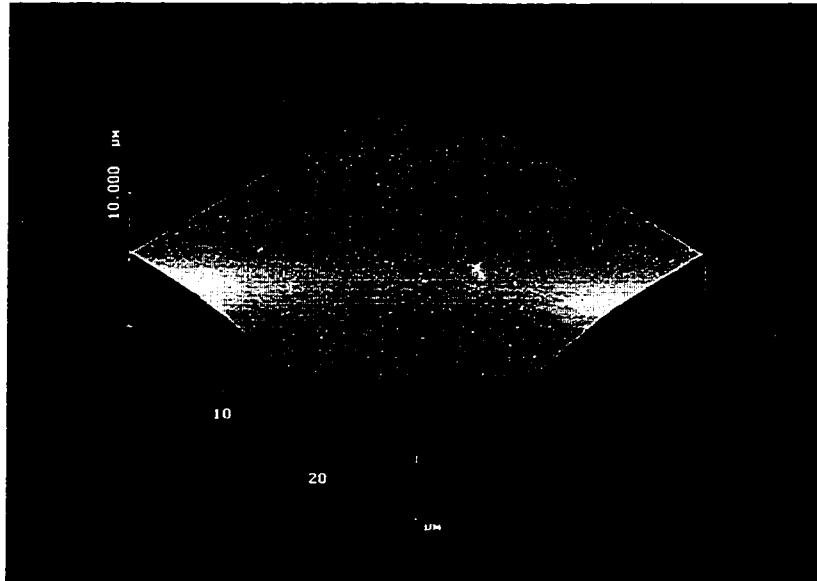


Figure 15. AFM image of a hole ablated in single crystal type IIA diamond with 1,000, 120 fs pulses (spot size=90 μm and 200 μJ/pulse)

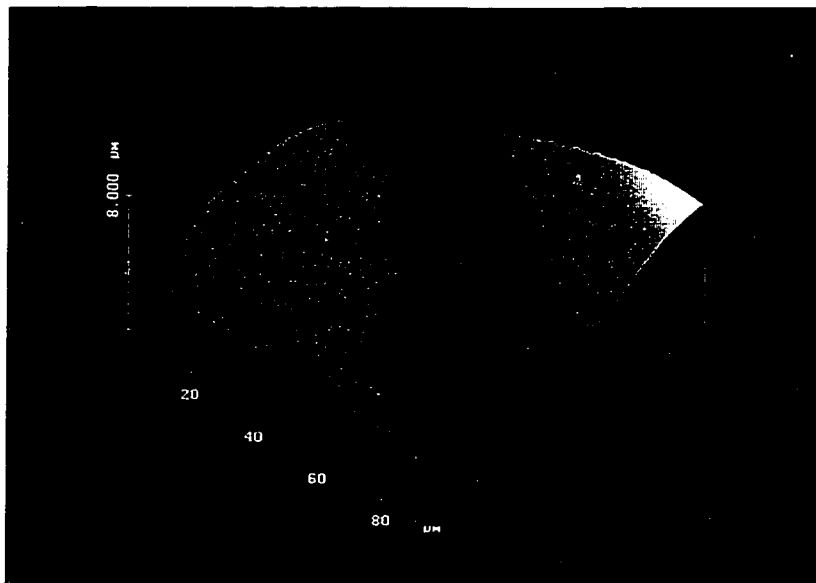


Figure 16. AFM image of a groove ablated in single crystal type IIA diamond with 120 fs pulses at 1 kHz.

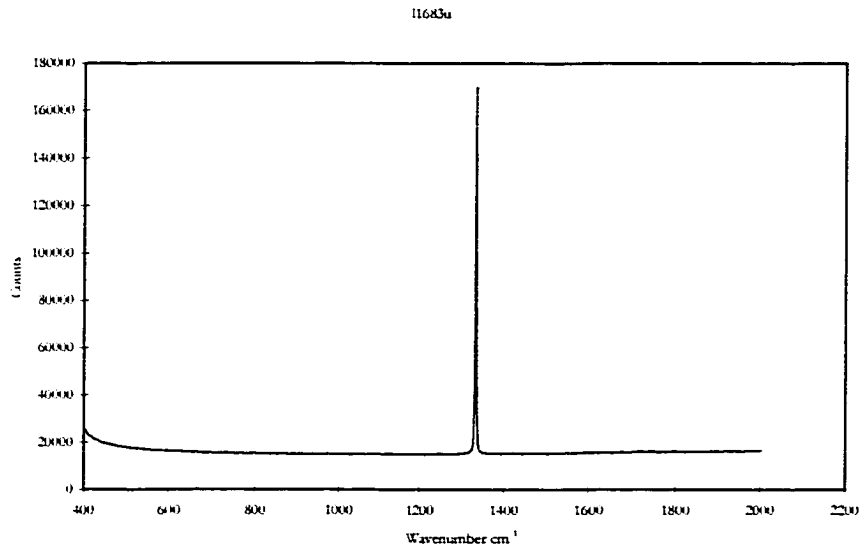


Figure 17. Raman spectrum of untreated single crystal type IIA diamond

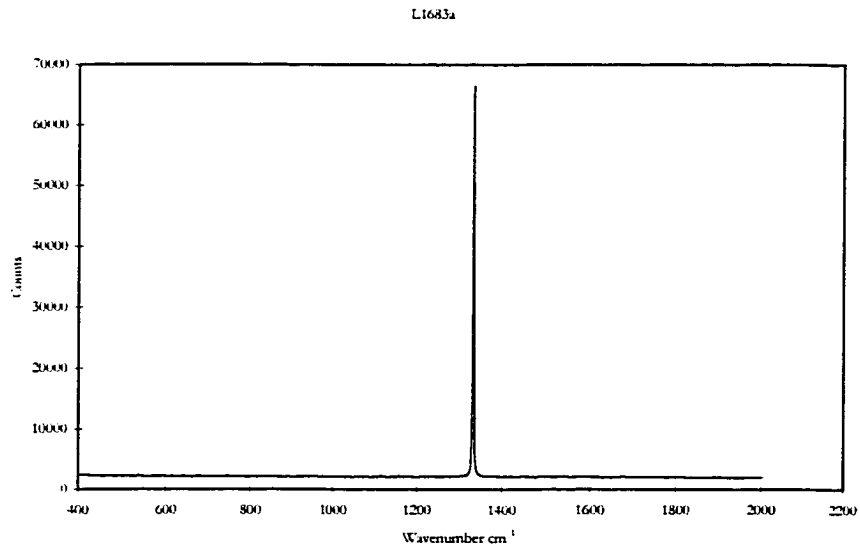


Figure 18. Raman spectrum of type IIA single crystal diamond ablated with 825 nm (120 fs) laser

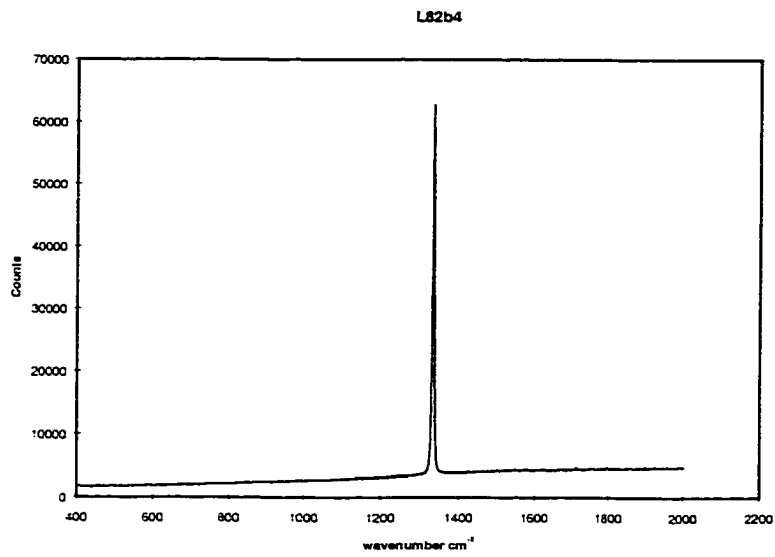


Figure 19. Raman spectrum of CVD diamond ablated with 120 fs 150  $\mu$ J pulses

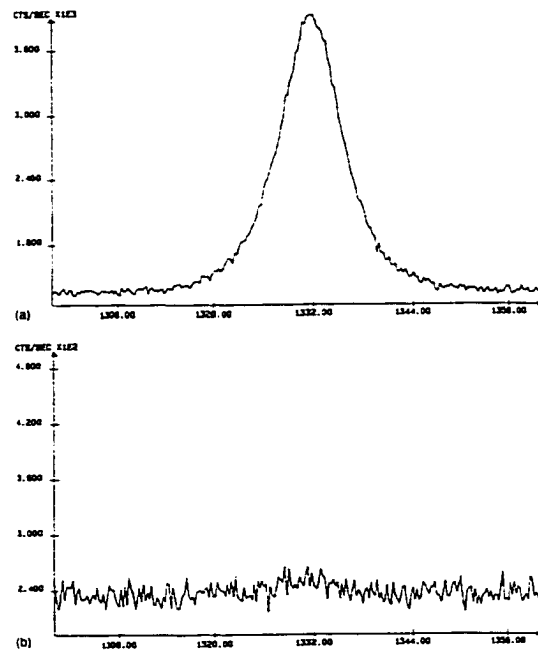


Figure 20. Raman spectrum of CVD diamond in untreated form (a) and ablated with an excimer laser using 23 ns pulses (b)<sup>6</sup>

### ***Conclusions***

Finite-difference and molecular dynamics model predictions of ultrashort pulsed ablation of diamond show that the ablation threshold and the heat affected zone are minimized with ultrashort pulses. The cleaner surfaces created with ultrashort pulses was explained by the models. Experimental data validated model findings.

### ***References***

1. V. G. Ralchenko, and S. M. Pimenov, *Handbook of Industrial Diamonds and Diamond Films*, 983-1021 (New York: Marcel Dekker, Inc. 1999).
2. M. D. Shirk, P. A. Molian, and A. P. Malshe, *J. Laser App.* **10**, 64-70 (1998).
3. M. S. Tang and C. Z. Wang, *Phys Rev B* **53**, 979-982 (1996).
4. J. R. Morris, C. Z. Wang, and K. M. Ho, *Phys. Rev. B* **52**, 4138-4145 (1995).
5. D. A. Papaconstatopoulos, *Handbook of the Band Structure of Elemental Solids*, 230 (Plenum Press NY, 1986).
6. R. Windholz and P. A. Molian *J. Mater. Sci.* **32**, 4295-4301 (1997).

## CHAPTER 7. FEMTOSECOND LASER-INDUCED PERIODIC STRUCTURE WRITING ON DIAMOND CRYSTALS AND MICRO-CLUSTERS

A paper accepted for publication in Applied Physics Letters (1999)

A. M. Ozkan, A. P. Malshe, T. A. Railkar, W. D. Brown, M. D. Shirk, and P. A. Molian

### *Abstract*

Three-dimensional, periodic nano-writing on diamond clusters is reported in this letter. Concentric circular rings were observed on diamond micro-clusters, nucleated near the periphery of laser irradiated region, when chemical vapor deposited (CVD) diamond was processed in air, with laser pulses of 380 fs duration and at a wavelength of 248 nm. Periodic ripples also have been observed on single crystal and polycrystalline diamond surfaces. Further, it is experimentally shown that the periodicity of these corrugated 2D and 3D structures is *shorter* than that of the laser wavelength used (248 nm for excimer fs laser and 825 nm for Ti-Sapphire fs laser). This work thus opens doors for writing three-dimensional periodic structures on diamond and other materials for various device applications.

### *Introduction*

Femtosecond (fs) laser technology attracts tremendous interest from scientific and manufacturing communities alike due to its ultra-precise and chemical/mechanical *damage-free* material processing capabilities<sup>1</sup>. As the understanding of fs laser-material interaction improves, and as novel phenomenon are discovered, increasing applications are becoming feasible<sup>2</sup>. In particular, the ability of fs laser processing to write three-dimensional structures in various materials is technologically attractive for applications such as microelectromechanical systems (MEMS), mesa structures, etc.

In this letter, we report the experimental observation of sub-micron writing of diamond crystals and clusters. A three-dimensional concentric ring pattern, separated by a period of about 125 nm, has been observed on polycrystalline diamond using ultraviolet excimer ( $t_p \sim 380$  fs,  $\lambda = 248$  nm) laser. We attribute the formation of such periodic 2-D as well as 3-D structures to optical interference of the light reflected from the surface with the incident light and/or the back reflected light from the laser generated plasma.

Periodic surface structures, or ripples, have been produced in dielectrics, semiconductors, and metals by lasers operating at wavelengths from the infrared to the ultraviolet region of the electromagnetic spectrum, and having pulse durations ranging from continuous wave (cw) to femtosecond pulses<sup>3-9</sup>. It has been suggested that these ripples arise from a standing wave that is produced due to the interference of incident laser light with scattered waves from a surface disturbance<sup>5</sup>. Consequently, the melting threshold of the surface is periodically exceeded, and rapid re-solidification of a thin layer of molten material may give rise to a corrugated structure. In order for the interference pattern to be etched on the target surface, the intensity should be sufficiently high. The first pulse causes random surface roughening, while the subsequent pulses create periodic ripples that are classified as S+, S-, and  $\epsilon$  fringes<sup>10</sup>. The wavelength, polarization and incident angle of the laser radiation determine the spatial period. The S+ and S- type of fringes occur perpendicularly to the polarization and have a period given by:

$$\Lambda_{\pm} = \lambda / (1 \pm \sin\theta) \quad (1)$$

where  $\theta$  is the angle of incidence. The S- is usually dominant. The  $\epsilon$  type of fringes are rarely formed and run parallel to the polarization, with a period given by:

$$\Lambda_{\epsilon} = \lambda / \cos\theta \quad (2)$$

Thus, the spatial period,  $\Lambda$ , of these ripples is known to be closely related to the wavelength,  $\lambda$ , and the angle of incidence<sup>11</sup>. Ageev *et al.*<sup>12</sup> have demonstrated periodic structures in CO<sub>2</sub> laser treated CVD diamond films, with a period of 10  $\mu\text{m}$ , which is close to that of the laser wavelength used (10.6  $\mu\text{m}$ ).

However, our results suggest a spacing that is much shorter than what is predicted by the above equations, and by previous experimental data. Also, the presented results are novel due to the fact that they demonstrate laser writing, not only on 2-D surface but also 3-D features. Yet, our observations are consistent with the predictions since, for circularly polarized light, no ripples were observed<sup>11</sup>. Linear polarization, as against to circular polarization, promotes the periodicity.

Recently, with fs laser pulses, Sokolowski-Tinten *et al.*<sup>13</sup> reported Newton fringes caused by optical interference of light reflected from two boundaries confining the expanding layer of ablated metals, and have attributed it to the laser-induced plasma<sup>13</sup>. We attribute the fringe pattern formations on different types of diamond to the same interference phenomenon, that is, incoming light is reflected from the surface and interferes with the back reflected wave from the plasma, forming standing waves. This gradient in the intense electric field leads to linear interference patterns on smooth plane surfaces, as on the surface of a single crystal. Concentric rings have been formed on three-dimensional surfaces such as those found in diamond clusters. For unpolished, extremely coarse, CVD diamond, the traveling interference patterns cross and a cross-hatch pattern was observed. The novel findings of this research are:

- ◆ Periodic writing of 3D-structures during *in-situ* processing;

- ◆ observation of a periodicity *smaller* than the wavelength of the laser radiation used, thereby demonstrating a deviation from established predictions<sup>13</sup>;
- ◆ surface morphology of the periodic writings depends on the virgin surface morphology of the samples.

The following text describes and discusses the findings in more details. Single crystal type IIA natural diamond samples with (100) orientation (Harris Diamond Corporation, NJ) and chemical vapor deposited (CVD) polycrystalline diamond (Norton Diamond Films, MA) were used for these experiments. All samples were initially degreased using trichloroethylene, methanol, and ethanol, then submersed in boiling ( $\text{Cr}_2\text{O}_3 + \text{H}_2\text{SO}_4$ ) and ( $\text{H}_2\text{O}_2 + \text{NH}_3\text{OH}$ ) mixtures, then rinsed with de-ionized water, and finally dried in a jet of dry nitrogen gas. The average surface roughness ( $R_a$ ) of the diamond used in this study was as follows: single crystal type IIA diamond,  $R_a \sim 40$  nm; polished CVD diamond,  $R_a \sim 0.2 - 0.5$   $\mu\text{m}$ ; unpolished CVD diamond samples,  $R_a \sim 20$  to  $50$   $\mu\text{m}$ .

Femtosecond UV and NIR lasers were used in these experiments. The UV excimer laser (Laser Laboratorium, Göttingen, Germany) delivered pulses of  $\sim 380$  fs duration, 248 nm wavelength, and 100 mW average output power with at a repetition rate of 10 Hz. The output beam was linearly polarized in the horizontal plane of the laser light. The laser light, imaged through a mask, was focused using a cylindrical lens with a focal length of 200 mm. All experiments were performed in air ambient, unless otherwise stated. A femtosecond IR (Ti-Sapphire, Lawrence Livermore National Laboratories, Livermore, CA) laser delivers pulses of  $\sim 150$  fs duration at an 825 nm wavelength, and with 0.5-2 W average power at a repetition rate of 1 kHz. The output beam was linearly polarized.

Figure 1 shows scanning electron micrographs of an untreated single crystal type-II A diamond surface for reference, and ripple structures observed on the region treated with a laser when the sample was processed with  $\sim 1.5$  J/cm<sup>2</sup>, with about 100 pulses in vacuum.

The grooves are formed perpendicular to the direction of the electric field. The spacing of ripples is of the order of the laser wavelength ( $\Lambda \sim \lambda = 248 \text{ nm}$ ), which agrees with previously observed ripple formations due to optical interference<sup>11</sup>. Since the light was incident at  $\theta = 0$  (normal incidence), in agreement with predictions from equation (I), the maxima are separated by  $\Lambda = 248 \text{ nm}$ . However, on observing the periodic structures in Figure 1b more closely, it is seen that there are also regions where ripple formations of intermediate spacings, lesser than 248 nm, are formed. Figure 1c clearly shows these structures at a higher magnification. Here, the period is of the order of 50 nm to 100 nm, and formation of these secondary minima and maxima could be attributed to out-of-phase superposition of electromagnetic fields from the laser pulses. We hypothesize that the scattered wave is not only produced by the interference, but also by a thin waveguide etched on the surface.

Since the interference phenomenon results from constructive and destructive superimposition of incident electric field with a surface scattered wave, we predict that the morphology of the surface directly affects the nature of ripples formed, which is observed in the following results. Unpolished CVD diamond employed in this study had 50 to 100  $\mu\text{m}$  wide grains at various orientations on the surface. Figure 2a shows the periodic structure formation on the terrace of a CVD diamond crystal. Figure 2b shows two surface ripple trains crossing each other on the side of a crystal wall, creating a crosshatch pattern. The periodicity of these ripples does not agree with the relation  $\Lambda = \lambda / (1 \pm \sin\theta)$  as suggested previously<sup>11</sup>. A more complex interaction between the incident, scattered, and possibly diffracted light could lead to integer fractions of  $\lambda$ .

Figure 3a shows the deposition of diamond micro-clusters around the ablation area. The diamond phase is confirmed by micro-Raman spectroscopy measurements. Some clusters are deposited *on* the ablation spot. When irradiation experiments were carried out in the absence of vacuum and flow of gases, the sublimed/evaporated material, present in the plasma, would fall back onto the material, thereby initiating nucleation on the CVD surface. Further systematic analysis of these findings is underway. Figure 3b shows a close-up view of the clusters. Surface structuring on larger clusters is readily observable. Figures 3c and 3d show a view of many 2  $\mu\text{m}$  size clusters with circular corrugations on them. The periodicity is of the order of half the incident wavelength. We attribute this to interference between the incident field and the scattered field that propagates parallel to the surface. Figure 4 presents a schematic of the proposed model for the interaction between an incoming wave and the scattered wave to form an interference pattern on the clusters. The consistent periodicity ( $\lambda/2$ ) observed on all the clusters nucleated along the ablation path indicates that the formation of circular corrugations on these clusters may not be due to random stacking faults which occur during the growth process. Thus, the observance of fringe patterns, of the same nature, on other diamond surfaces is supporting evidence for attributing these 3D corrugations on diamond clusters to optical interference. The periodicity of these ripples is greatly influenced by the surface roughness and morphology of the surface. For an extremely smooth, single-crystal, diamond surface, the interaction is only between the incident wave and the wave reflected from the surface. However, for a surface with polycrystalline grains, i.e., pyramids with smooth facets, on an unpolished diamond surface or spherical random features on laser processed diamond, the interaction between the incident, scattered, and back-scattered waves is more complex. The angle of incidence that different grain surfaces see deviates from the normal incidence, leading to variations in the periodicity observed on particular grains.

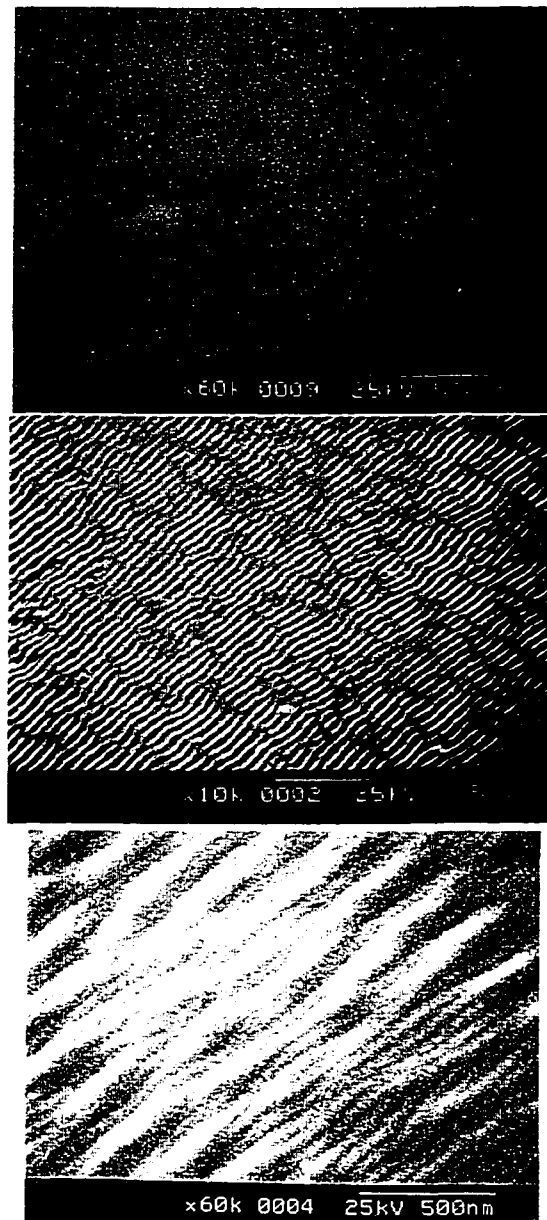


Figure 1. Scanning electron micrographs of a) original untreated single crystal type IIA diamond surface, b) excimer fs laser treated ( $F=1.5 \text{ J/cm}^2$ , 100 pulses,  $t_p=380 \text{ fs}$ ,  $\lambda=248 \text{ nm}$ ) CVD diamond surface, c) same surface at a higher magnification, with multiple periodicities,  $\sim 250 \text{ nm}$  as well as  $\sim 50$  to  $100 \text{ nm}$ .

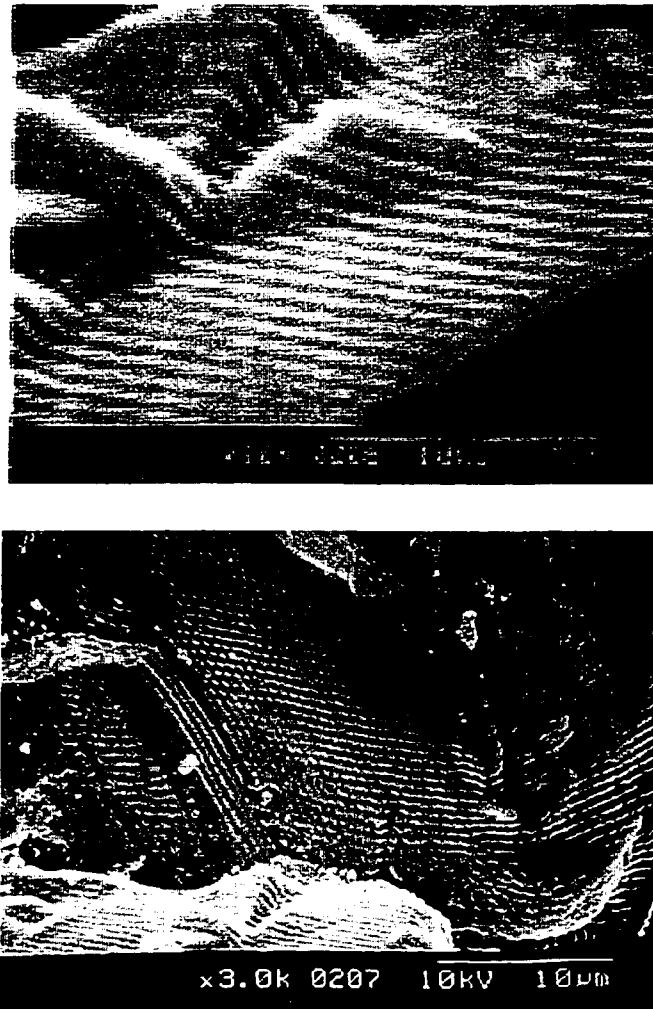


Figure 2. Scanning electron micrographs of unpolished CVD diamond irradiated with a Ti-Sapphire fs laser ( $E=2.5 \text{ J/cm}^2$ , 1000 pulses,  $\tau_p=150 \text{ fs}$ ,  $\lambda=825 \text{ nm}$ ), a) single interference pattern, b) two interference patterns crossing each other at 90 degrees.

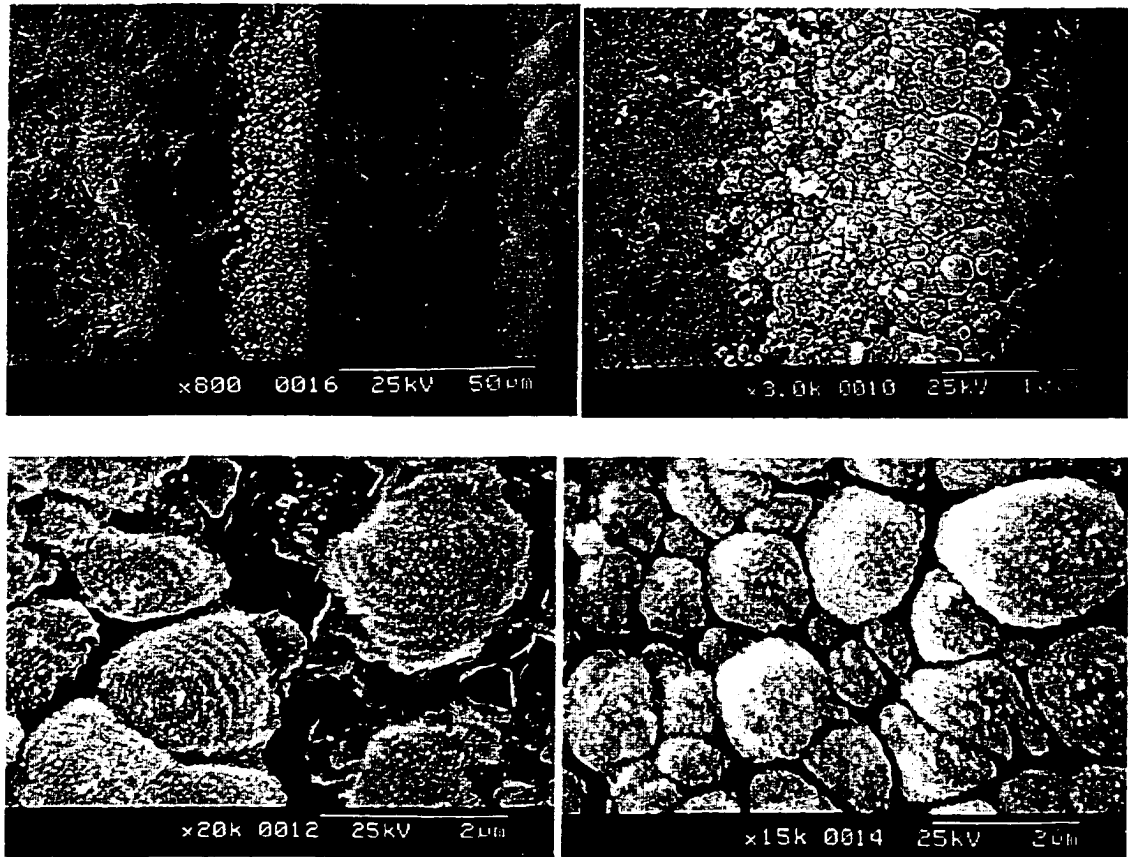


Figure 3. Scanning electron micrographs of polished CVD diamond irradiated with an excimer fs laser ( $E=0.7 \text{ J/cm}^2$ , 1000 pulses,  $\tau_p=380 \text{ fs}$ ,  $\lambda=248 \text{ nm}$ ), a) clusters formed around the ablation area, b) at a close-up view, periodic patterns are observable, c) and d)  $2 \mu\text{m}$  sized clusters with concentric periodic ring structures.

Periodic structure formation on diamond and similar other technologically important, but difficult to etch materials using fs lasers has applications in important fields such as MEMS, patterning for field-emitting displays, etc. In this letter, we have reported on periodic nano-patterning of diamond surfaces and clusters. Further research is underway to understand the parameters affecting this interference phenomenon and to implement this method to write 3D sub-micron structures on diamond.

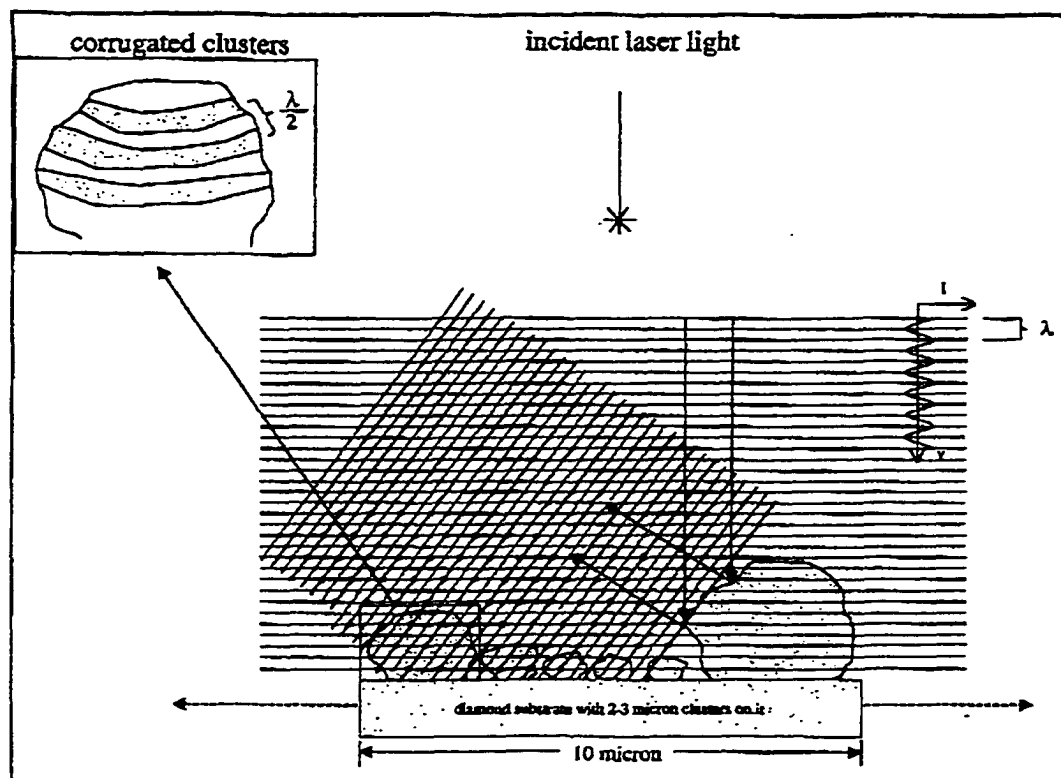


Figure 4. A schematic of proposed model for formation of 3D interference pattern, and hence writing on diamond clusters.

### *Acknowledgements*

The authors would like to acknowledge the National Science Foundation (NSF) for supporting this research work (Contract # DMI-9622518). MDS acknowledges Lawrence Livermore National Laboratory (LLNL) and Dr. Brent Stuart for Ti:Sapphire laser processing of diamond samples during a summer internship.

### *References*

1. A.P. Malshe, T.A. Railkar, A.M. Ozkan, P.A. Molian and W.D. Brown, Proceedings of the ASME Manufacturing Science and Engineering Division - ASME 1998, p. 193 (1998).
2. "Pulsed Femtosecond Excimer Laser-Induced Chemically Clean Etching of Diamond" A.P. Malshe, A.M. Ozkan, T.A. Railkar, P.A. Molian and W.D. Brown; Mat. Res. Soc. Symp. Proc. Vol 526 p. 123 (1998). Also, the entire proceedings of 'Conference on Lasers and Electro-Optics (CLEO), Baltimore MD May 1999 as well as International Conference on the Applications of Lasers and Electro-Optics (ICALEO) Orlando, FL November 1998.
3. F. Keilmann and Y.H. Bai, Appl. Phys. A, **29** 9 (1982).
4. G. N. Maracas, G.L. Harris, C.A. Lee, and R.A. McFarlane, Appl. Phys. Lett., **33** 453 (1978).
5. N.R. Isenor, Appl. Phys. Lett., **31** 148 (1977).
6. H. Varel, M. Wahmer, A. Rosenfeld, D. Ashkenasi, and E.E.B. Campbell, Appl. Surf. Sci., **127-129** 128 (1998).
7. J.F. Young, J.E. Sipe, J.S. Preston, and H.M. van Driel, Appl. Phys. Lett., **41** 261 (1982).
8. P. M. Fauchet and A.E. Siegman, Appl. Phys. Lett., **40** 824 (1982).
9. J. Ihlemann, B. Wolff and P. Simon, Appl. Phys. A, **54** 363 (1992)
10. "Laser Ablation and Desorption", edited by John C. Miller and Richard F. Haglund Jr., Academic Press, San Diego p. 341 (1998).

11. Zhou Guosheng, P.M. Fauchet and A.E. Siegman, *Phys. Rev. B*, **26** 5366 (1982).
12. V.P. Ageev, L. Bullov, V.I. Konov, A.V. Kuzmichev, S.M. Pimenov, A.M. Prokhorov, V.G. Ral'chenko, B.V. Spitsyn and B.I. Capliev; *Sov. Phys. Dokl.*, **33** 840 (1988).
13. K. Sokolowski-Tinten, J. Bialkowski, A. Cavalleri and D. von der Linde, *Appl. Surf. Sci.*, **127-129** 755 (1998).

## CHAPTER 8. ULTRASHORT PULSED LASER ABLATION OF HIGHLY ORIENTED PYROLYTIC GRAPHITE

A paper to be submitted to the journal Carbon

M. D. Shirk and P. A. Molian

### *Abstract*

Ultrashort pulsed lasers show potential for uses in precision micromanufacturing in which nearly all the material within the focal spot is ablated before any significant heat conduction or mass flow takes place, thus resulting in precise machining with little or no collateral thermal damage. The objective of this contribution is to demonstrate the benefits of ultrashort laser pulses varying from 120 fs to 20 ps for the ablation of graphite. In this investigation highly oriented, pyrolytic graphite (HOPG) targets were irradiated by use of an ultrafast Ti:Sapphire laser operating at 825-nm wavelength at energy fluences ranging from 0.1 to 6 J/cm<sup>2</sup>. The morphology and quality of laser ablated surfaces were characterized by profilometry, scanning electron microscopy (SEM), atomic force microscopy (AFM), and Raman spectroscopy. The results were also compared with those obtained in conventional nanosecond pulsed laser ablation.

The ablation rate, about 70 nm/pulse at 2 J/cm<sup>2</sup> (120-fs), was increased with an increase energy fluence until saturation was reached. By comparison, the 248-nm excimer laser beam with 23-ns duration ablated a depth of 15 nm per pulse at 2 J/cm<sup>2</sup>. The ablation depth per pulse was in close agreement with the theoretical model predictions of laser-solid interactions in the short-pulse regime. The enhanced ablation efficiency in femtosecond pulses is attributed to the increased absorption coefficient caused by the multiphoton absorption. Post-analysis of laser irradiated regions revealed a reduction in thermal effects and a decrease in the formation of diamond-like carbon as the pulse width was shortened. This demonstrates the clean and precise

machining capabilities of ultrashort pulsed lasers for HOPG that could be applied in the areas of thin-film deposition, nanotube synthesis, and dust-free machining.

### *Introduction*

Pulsed laser ablation (PLA) is a technique of vast scientific and significant industrial interest because of its numerous applications in micromachining and thin-film deposition. The most attractive feature of PLA is the highly localized spatial interactions between the beam and the material, leading to small features, precision, excellent edge quality, and minimal heat-affected-zone (HAZ). In addition, PLA works on most materials and does not chemically contaminate surfaces.

Graphite is the material of choice for a number of engineering applications, and lasers are used in various ways for fabricating graphite. PLA is applied on graphite targets to deposit diamond-like carbon (DLC) films for many applications<sup>1-8</sup>. Time-of-flight and mass spectrometry methods have been used extensively to identify and characterize various carbon species formed during PLA and their velocity distributions. Several mechanisms have been proposed for the ablation of graphite and synthesis of DLC films. PLA has also been used to fabricate carbon nanotubes, or fullerenes<sup>9-11</sup>. The laser method produces single-wall carbon nanotubes (SWNT) in high yields by a basic process that involves preheating the graphite target in vacuum and then subjecting it to a pulsed laser. The soot generated largely of SWNT. Both single and dual laser beams have been investigated for this purpose. The CO<sub>2</sub> laser was superior to the Nd:YAG laser in allowing SWNT to form at lower temperatures<sup>10</sup>. In addition, the lasers have proven to be the environmentally benign tools for machining fuel cells made of graphite and to replace the expensive diamond-tip fabrication procedure that produces large amounts of graphite dust<sup>12</sup>.

The work described in this paper focused on the role of an ultrashort pulsed laser beam in the ablation of highly oriented pyrolytic graphite (HOPG), a specific form of graphite. The primary objectives were to elucidate the role of pulse width (120 fs to 20 ps) in the ablation of HOPG and to obtain improved understanding of ultrashort pulse laser/material interactions.

Windholtz and Molian<sup>13</sup> used a 248 nm, 23 ns KrF excimer laser to study laser ablation of HOPG. Significant collateral thermal damage and evidence of phase changes were observed on the ablated surfaces, including some evidence for diamond and DLC phases. Threshold energy fluence was reported to be about 0.9 J/cm<sup>2</sup>.<sup>7</sup> Reitze et al.<sup>13</sup> also studied laser ablation of HOPG, using a 620 nm ring-dye laser operating at 90 fs. Pulse-probe investigations were used to determine time-dependent reflectivity of the surface after laser irradiation. Results showed that the excited surface rapidly becomes liquid, with self reflectivity rising from around 0.3, for the unexcited surface and for pulses below the damage threshold fluence, to slightly above 0.7 for pulses 20 times the damage threshold. This increase is followed by hydrodynamic expansion a few picoseconds after irradiation, which significantly reduces reflectivity as a result of the expanding plasma and disrupted surface. The reported damage fluence for HOPG was  $0.13 \pm 0.02$  J/cm<sup>2</sup> at 90 fs, 620 nm,<sup>14</sup> much lower than that at 23-ns, 248 nm.<sup>13</sup>

At present excimer lasers are considered as the best choices for certain PLA applications, including photoablation, chemical etching, lithography, and surface cleaning. Excimer lasers produce high energy per pulse (up to 2 J/pulse) and nanosecond (ns) pulse duration that allows the beam to interact strongly with materials. In addition, the short wavelengths (157-351 nm) create photochemical interactions with the target material, resulting in enhanced material removal. However, excimer lasers have three major shortcomings that limit their use. First, the poor beam quality does not allow the excimer beam to be tightly focused down to the size of the

wavelength, with the result that it is difficult to fabricate features with dimensions less than 10  $\mu\text{m}$ . Second, excimer lasers distribute the heat on the work over a distance of some microns during the pulse duration, particularly in metals and semiconductors (high thermal conductivity materials). Third, excimer lasers have been only slightly successful in industrial applications because of the presence of corrosive gases in the laser cavity (handling problems). Recent developments in ultrafast laser technology can successfully overcome these problems.

Ultrafast lasers, which are those with pulse durations approaching  $10^{-15}$  sec and peak powers up to 1300 TW, are capable of providing extreme intensities up to  $10^{21}$  W/cm<sup>2</sup>—the equivalent of focusing the power of all sunlight falling on earth on a spot of 0.1 mm in diameter. In ultrafast lasers, photons are tightly packed to form an extremely short pulse. The two ultrafast lasers presently available for materials processing are the solid-state CPA Ti: Sapphire (800 nm) and the gaseous-liquid excimer-dye (248 nm) lasers. The Ti:Sapphire laser is superior to the excimer-dye laser in the following respects: shorter pulse width (20-150 fs), high pulse repetition rate (1-10 kHz), tunable wavelength (735-1053 nm), and superior beam quality (about 95% Gaussian).

Potential applications of ultrafast lasers include precision drilling and cutting of sub-micron features for the microelectronics/medical industry, pulsed laser deposition of thin films, and desorption of water molecules in microelectromechanical systems (MEMS) to prevent the “stiction” failure. Two excellent review articles<sup>14,15</sup> provide substantial information on the applications and capabilities of ultrafast lasers. The reviews indicate that ultrafast lasers are superior to ns-pulsed excimer lasers in spatial resolution, reduction of thermal damage, and plasma formation. The beneficial effects of ultra-short pulse lasers with regards to material interaction are summarized in Table 1.

Table 1. Benefits of ultrafast lasers

<ul style="list-style-type: none"> <li>• Precision with reduced thermal damage</li> <li>• Clean material removal</li> <li>• Lower thresholds for ablation</li> <li>• Feature sizes smaller than laser spot size</li> <li>• Hydrodynamic expansion occurs after pulse has ended, no interaction of expanding plume with beam</li> </ul>
--

Ultrafast lasers have brought about significant improvements in precision processing of metals, semiconductors, Teflon, and dielectrics<sup>16-19</sup>. However, these improvements depend largely on the specific material and wavelength. It is not clear whether shorter pulse widths always produce favorable results in terms of precision and controllability of ablation. For example, the highest precision was obtained in 790-nm Ti:Sapphire laser irradiation of CaF<sub>2</sub> only when the pulse width was a few picoseconds<sup>5</sup> rather than femtoseconds

### *Material*

Carbon can crystallize in two entirely different configurations: graphite and diamond. The characteristic feature of graphite is layers of hexagonally arranged carbon atoms in a network resembling a honeycomb. The three-dimensional crystal is made up of a huge number of single layers, each one shifted by half a lattice constant relative to the lower one, forming the so-called A-B stacking. Graphite is a material of high strength, good chemical stability, high thermal/electrical conductivity, low expansion, and high thermal shock resistance. Graphite is used for a wide range of metallurgical (crucibles, casting molds, high-temperature refractories) and electrical (heating elements, brushes and resistors, electrodes, contacts) applications.

Highly oriented pyrolytic graphite (HOPG), a unique form of graphite, is produced in two steps: thermal decomposition of hydrocarbon gases such as methane onto a hot substrate in a vacuum furnace to form pyrolytic graphite, followed by heat treatment of pyrolytic graphite under compressive stress. HOPG is a high-purity, polycrystalline material with near theoretical

density that exhibits many of the properties of single-crystal graphite. Mechanical, thermal, and electrical properties of HOPG are superior to those of conventional graphite. The layered structure of HOPG, shown in Figure 1, results in anisotropic properties. For example, HOPG exhibits a very high thermal conductivity, similar to that of the best metal conductors in the "AB" plane but lower than that of ceramics in the "C" direction. Typical properties of HOPG are listed in Table 2.

HOPG is available as plate, freestanding shapes (crucibles, boats, tubes, etc.), and as an impermeable coating on graphite and other substrates. It is chemically inert, stable up to approximately 3000°C, impermeable to gases, and self-lubricating. It is used extensively in research on graphite and graphite intercalation compounds. HOPG also has valuable properties for application as monochromators for x-rays and thermal neutrons, and as calibration substrates for scanning tunneling microscopy. Other applications include sputtering targets, ion beam grids, ion implant hardware, liquid phase epitaxy hardware, crucibles for ultra high vacuum, thermal insulators, rocket nozzles, and heating elements.

### *Experimental procedure*

#### **Samples**

The samples used in this study were HOPG made for use as X-ray monochromators, of which the AB surface was used. The samples (Grade ZYB), obtained from Advanced Ceramics Corporation, Lakewood, OH, were flat and had dimensions of 12 mm x 12 mm x 2 mm.

#### **Laser**

The laser used to perform ablation was a Ti:Sapphire oscillator-amplifier system based on the chirped-pulsed-amplification technique. The specifications of this laser are presented in Table 3.

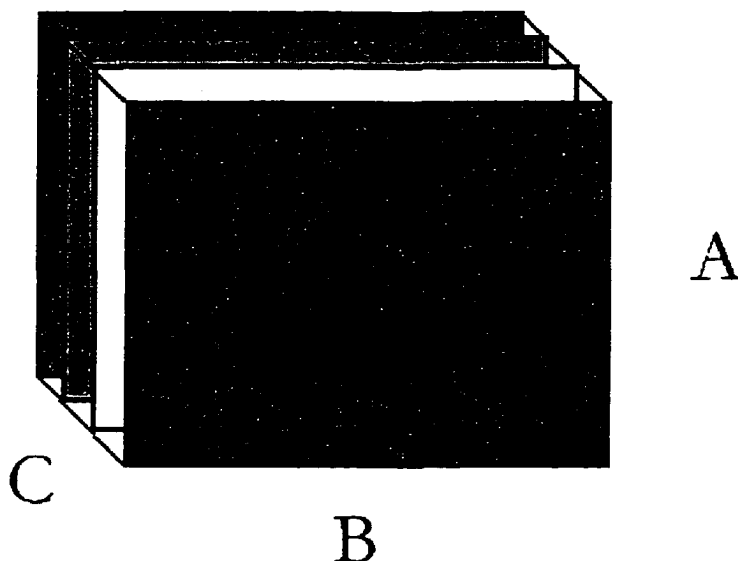


Figure 1. Anisotropic layered structure of HOPG

Table 2. Properties of HOPG at room temperature

Density	2.18-2.22 g/cc
Flexural Strength (AB directions)	120 Mpa
Tensile Strength (AB directions)	80 Mpa
Compressive Strength (AB directions)	100 Mpa
Young's Modulus (AB directions)	30 Gpa
Thermal Conductivity	
AB directions	400 W/m K
C direction	2 W/m K
Thermal Expansion	
AB directions	$0.5 \times 10^{-6} /K$
C direction	$15 \times 10^{-6} /K$
Electrical Resistivity	
AB directions	$0.5 \times 10^{-3}$ ohm-cm
C direction	0.5 ohm-cm
Melting point	Sublimes at 3650°C

Table 3. Characteristics of Ti:Sapphire laser

Wavelength	Pulse width	Pulse energy	Repetition rate	Beam size
825 nm	120 fs. min	5 mJ max.	1 kHz	12-mm round

The beam quality is the most important parameter affecting the accuracy, repeatability, and spatial resolution of laser-machined features. The beam quality of the Ti:Sapphire laser was characterized by use of beam-diagnostic equipment. This was done by using a vacuum chamber that has a second window opposite the entrance port. A second lens placed outside the chamber was used to image the beam at the plane where the sample was to be placed. This plane was imaged on the surface of a CCD camera, which was then passed into a PC running Coherent's Analyzer PC for Windows 1.1.10 (Analyzer can be set up for specific cameras by inputting the pixel size on the CCD chip). The first step in this method was to place a reticle where the sample would go and decrease the laser power so as not to machine the reticle. The beam was then focused onto the camera by moving the camera and turning the mirror until the reticle was visible. It is best if the focusing lens (before the chamber) is not at perfect focus at this point, so that the laser spot on the reticle is not extremely small; Figure 2 shows the optical setup used. Part of the reticle should contain a ruler with denominations of 10 microns to allow measurements to be verified. The beam profile was 92% Gaussian in one axis and 97% Gaussian in the other. The spot size for the sample that had varied power was oblong, with the major axis 120  $\mu\text{m}$  and the minor axis 100  $\mu\text{m}$ . The spot size for the sample that had varied pulse width was 160  $\mu\text{m}$  by 100  $\mu\text{m}$ . After the reticle is properly imaged onto the camera, then it can be removed, and the focusing lens can be adjusted to achieve a spot of the desired size. For this work, a 450-mm focal length, 825-nm anti-reflection coated lens was used. The spot for the varied pulse width was oblong because the lens was not perfectly perpendicular to the beam. One warning that must be heeded is that the intensity of the laser should not be raised to the point that the camera is damaged. The vacuum chamber was used to prevent distortions in the beam due to interaction with air when the beam is highly focused within the chamber.

## Laser ablation

Laser ablation of HOPG samples was carried out in a vacuum chamber evacuated to  $10^{-4}$  torr after the beam had been well characterized. Vacuum was used because processing in air often leads to highly undesirable particulate contamination, reduced rate of material removal, and distortions in the beam that can adversely affect precision and accuracy. A four-axis computer-controlled translation stage was used to position the samples within the chamber. A power meter was used to determine the average power incident on the sample. The pulse width was varied from 20-ps to 120-fs by moving the compressor grating away from its optimal position. The intensity was varied by rotating a quarter waveplate in front of a Brewster window, which allowed precise control of delivered power. Machining experiments were conducted using the experimental setup shown in Figure 4. For the studies on pulse width, the laser beam was focused through a lens to an oblong spot  $160\ \mu\text{m} \times 100\ \mu\text{m}$  in size. The power was set at 100 mW (0.1 mJ per pulse) and pulse width was varied as 120-fs, 1-ps, 5-ps, 10-ps, 15-ps, and 20-ps. The compressor grating had to be moved approximately 1.2 mm per picosecond of variation. The electronic shutter was opened for 30 s, 20 s, 10 s, 1 s, 0.5 s, 0.1 s, and 0.05 s, yielding approximately 30,000 pulses, 20,000 pulses, 10,000 pulses, 1,000 pulses, 500 pulses, 100 pulses, and 50 pulses, respectively.

For the studies on energy fluence effects at a pulse width of 120 fs, the spot was an oblong measuring  $120\ \mu\text{m} \times 100\ \mu\text{m}$ , and the power was varied as 1.0 W, 0.5 W, 0.4 W, 0.2 W, 0.1 W, 0.05 W, and 0.025 W. The exposure was varied as 50 s, 20 s, 10 s, 5 s, 1 s, 0.5 s, 0.1 s, and 0.05 s.

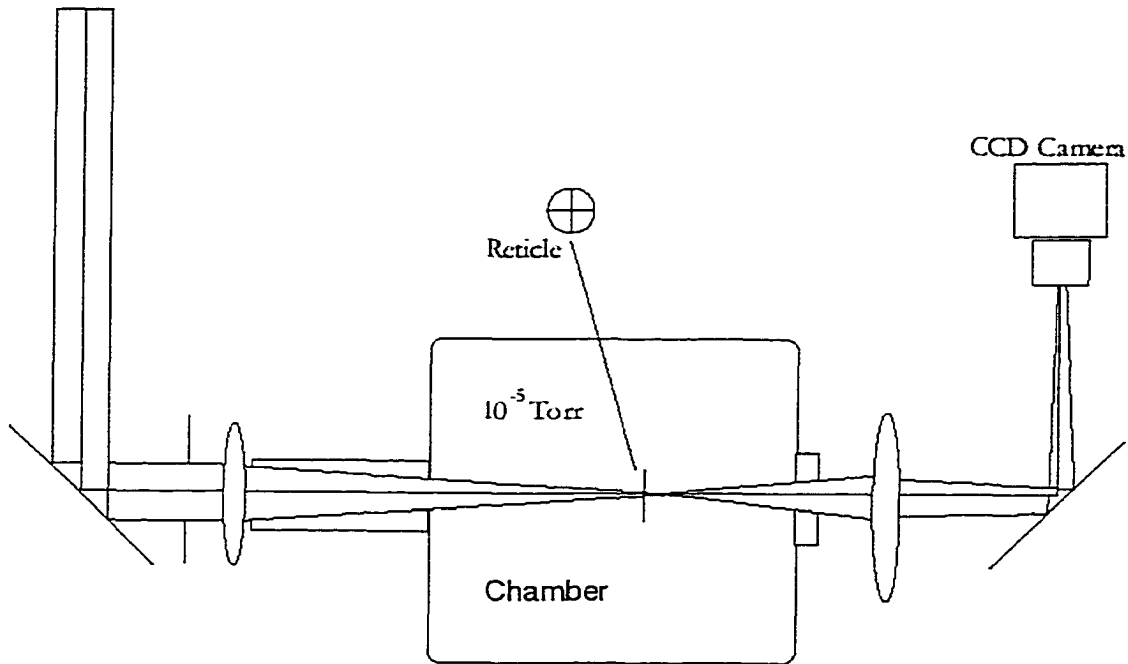


Figure 2. Optical setup for beam diagnostics

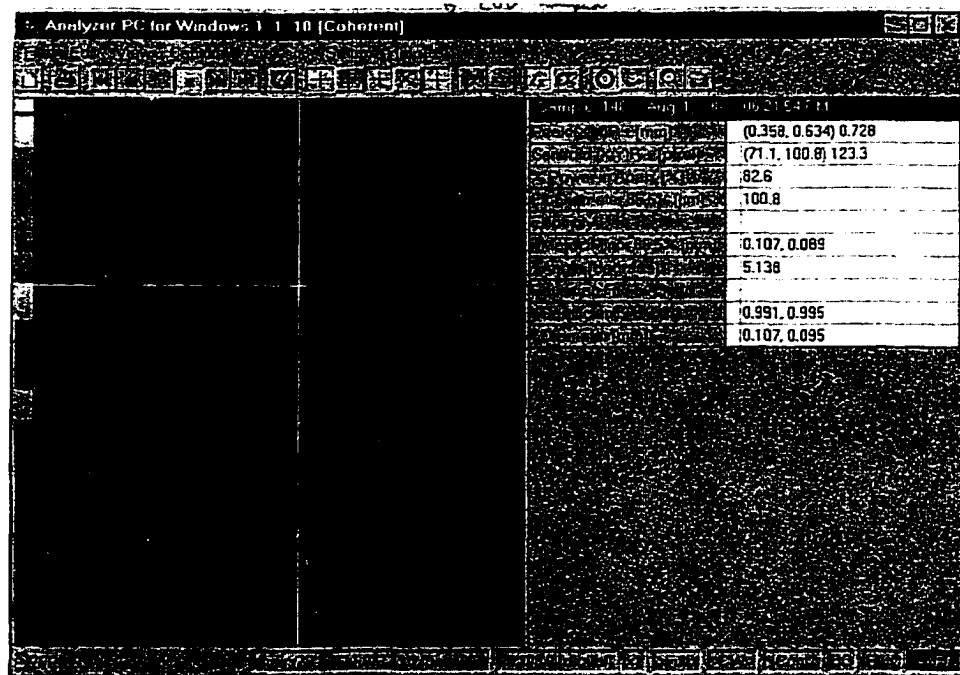


Figure 3. A sample window from the beam diagnostics software

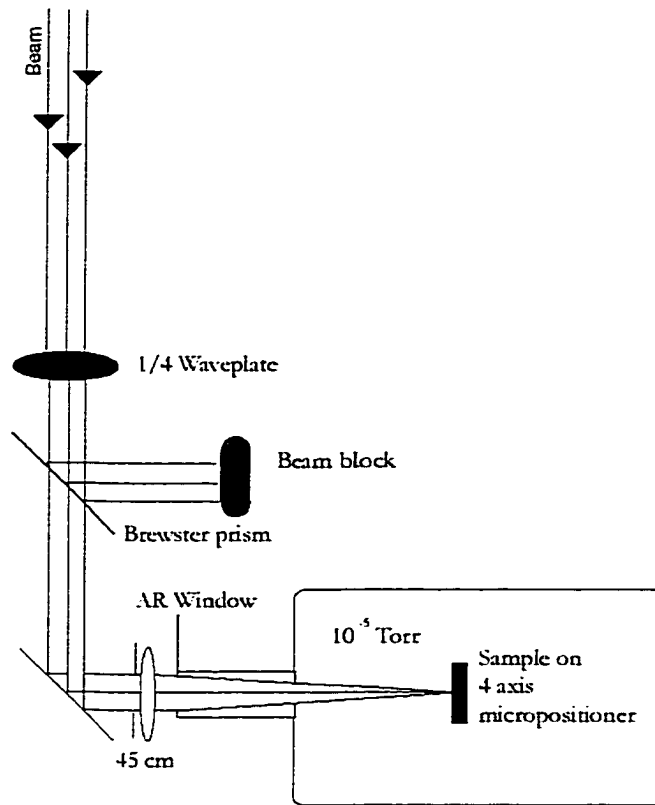


Figure 4. A schematic of experimental setup

### Characterization and analysis

A number of analytical instruments were used to measure and characterize the size, shape, taper, aspect ratio, recast layer, crack formation, surface roughness, and chemical contamination of machined regions.

*Profilometry:* A Sloan Dektak II diamond-tipped profilometer set at medium speed and  $500\ \mu\text{m}$  scan size was used to measure the hole depth. The depth was determined as the height of the unablated HOPG surface minus the depth of the hole (distance into the surface is negative). The data were then fitted using linear regression to obtain the etch depth per pulse. It should be noted that it was very difficult to verify that the tip had penetrated to the deepest part of the hole.

*Scanning Electron Microscopy (SEM):* SEM yields high-resolution images of surfaces of samples. The 5-kV accelerating voltage electron beam (JEOL JSM-35) was scanned over the surface and secondary electron images were generated to obtain information on the feature size, shape, grain structure, recast layer, and crack formation, along with laterally resolved chemical information. Representative plan-views of SEM images were taken at various locations.

*Atomic Force Microscopy (AFM):* AFM was performed using a Dimension 3000 SFM (Digital Instruments) equipped with a 90- $\mu\text{m}$  tube scanner and operated under ambient conditions to perform scanning force microscopy (SFM). All AFM topographic images were collected in the contact mode by use of a 200  $\mu\text{m}$  oxide sharpened triangular  $\text{Si}_3\text{N}_4$  cantilever (Nanoprobes) with normal bending of 0.12 N/m. All images were acquired using a constant-force mode at a normal force of  $\sim 30$  nN.

*Micro-Raman Spectroscopy:* Raman spectroscopy is the most widely accepted technique for determining the signatures of various forms of carbon. Raman experiments were performed at the Materials Research Laboratory at Pennsylvania State University, using an ISA U-100 Raman spectrometer in the micromode and using an Ar-ion laser; experimental conditions are listed in Table 4. Rapid scans from 1100-1700  $\text{cm}^{-1}$  wavenumbers were performed first, after which slower scans were carried out on the relevant peaks.

Table 4: Micro-Raman parameters

Raman Parameter	Value
Power	150 mW
Slit size	300 $\mu\text{m}$
Magnification	40X
Wavelength	514.532 nm

### *Results and discussion*

The first step in analysis of graphite samples is to determine the depth per pulse. This was done by determining the depth of holes produced with various numbers of pulses and then fitting the data by use of linear regression to determine the average depth per pulse. Figures 5-8 show results obtained with energy fluences of 2.1, 4.2, 5.3, 10.6 J/cm<sup>2</sup>. Figure 9 shows tabulations of the depths per pulse, along with evidence of saturation.

The ablation depth per pulse obtained in this study for 120-fs pulses is several times larger than those reported in the literature for conventional nanosecond excimer lasers. The average depth per pulse at 2 J/cm<sup>2</sup> was about 700 angstroms. Mechler et al.<sup>8</sup> observed an ablation rate of 100 angstroms per pulse for the 193-nm, 14 ns-pulse at 2 J/cm<sup>2</sup>. Windholz and Molian<sup>13</sup> reported a depth of 150 angstroms per pulse for the 248-nm, 23 ns pulses at 2 J/cm<sup>2</sup>.

The experimental data shown in Figure 9 was used to develop the following approximate relation between energy fluence,  $F$ , in J/cm<sup>2</sup>, and depth per pulse,  $z$ , in angstroms.

$$Z = 370 F^{0.95} \text{ for } F_{th} < F < F_s \quad (1)$$

Where  $F_{th}$  is threshold energy fluence and  $F_s$  is the saturation energy fluence. A scaling law analysis for laser pulses smaller than the lattice heating time, described by Momma et al.<sup>20</sup>, shows that the ablation depth per pulse,  $z$ , is approximately proportional to  $F_1^{0.67}$  where  $F_1 =$  absorbed energy fluence =  $F/0.7$  for HOPG.<sup>14</sup> Further simplification for  $F$  in the range 2 to 5 J/cm<sup>2</sup> shows that  $z \propto F^n$  where the exponent,  $n$ , varies between 0.8 and 1.0, suggesting close agreement with what is observed experimentally. The principles of ultrashort beam-solid interactions that were used to derive and validate the above quantitative relation can be summarized as follows:

The photons within the absorbed volume interact with free electrons through excitation processes (inverse Bremsstrahlung effect), resulting in a high electron temperature. It should be

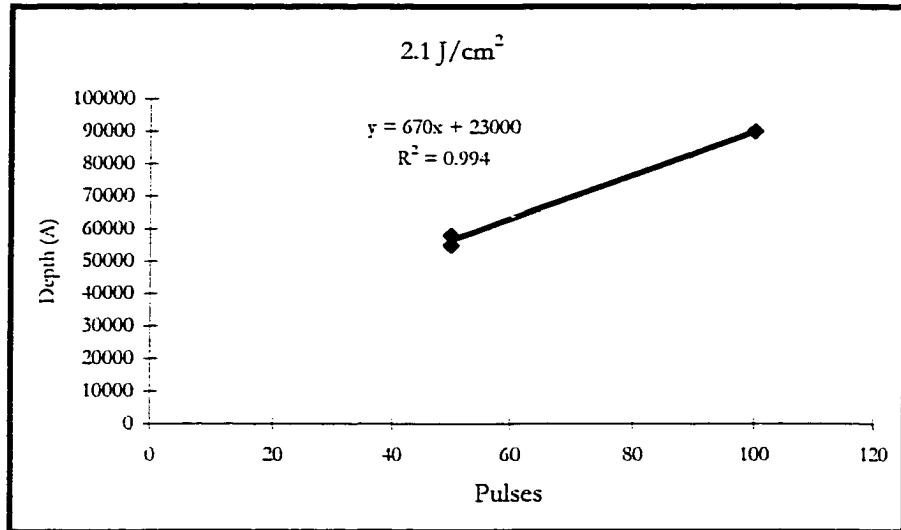


Figure 5. Depth per pulse fit for 2.1 J/cm<sup>2</sup> (120-fs)

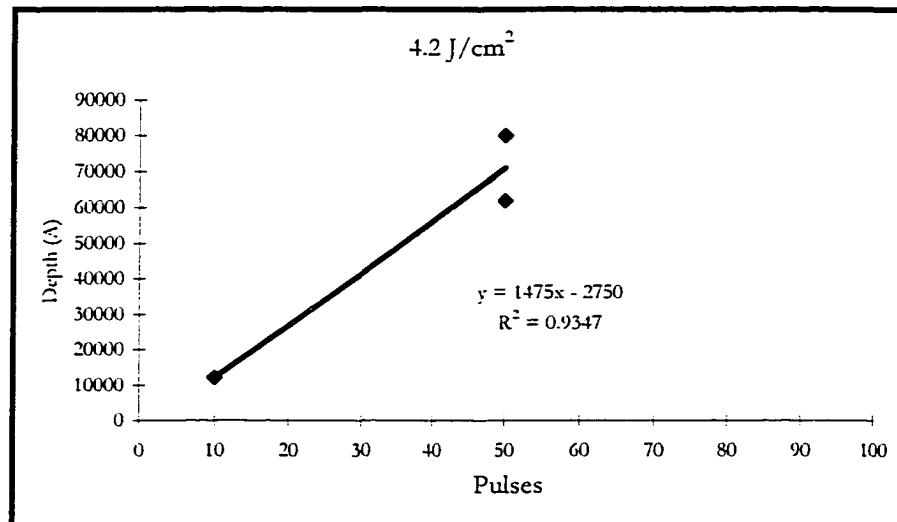


Figure 6. Depth per pulse fit for 4.2 J/cm<sup>2</sup> (120-fs)

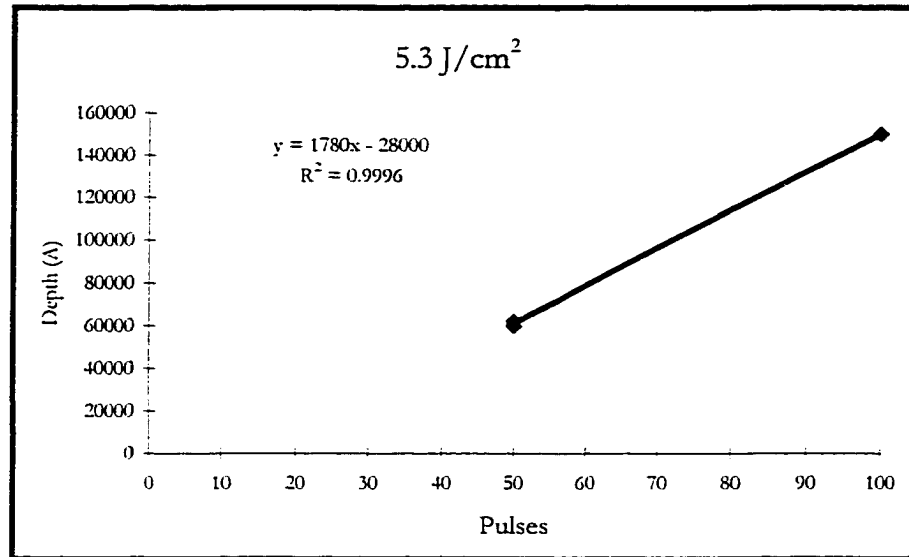


Figure 7. Depth per pulse fit for 5.3 J/cm<sup>2</sup> (120-fs)

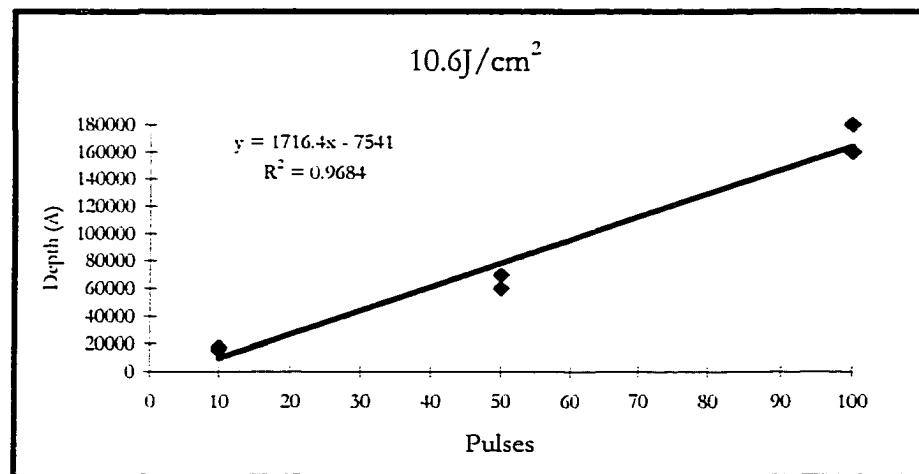


Figure 8. Depth per pulse fit for 10.6 J/cm<sup>2</sup> (120-fs)

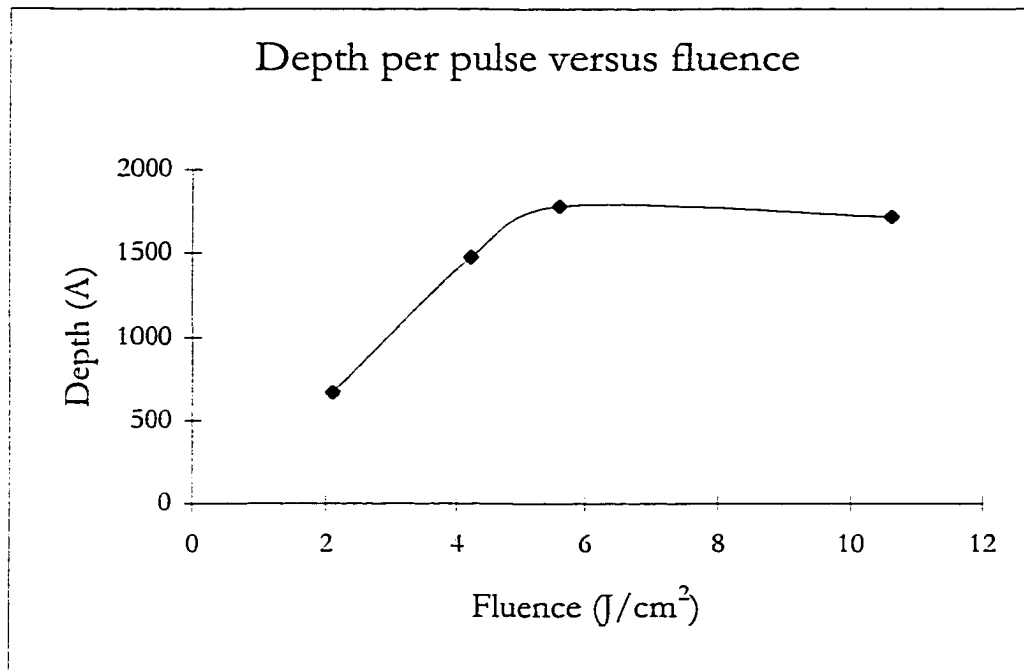


Figure 9. Plot of depth per pulse showing evidence of saturation above  $5.2 \text{ J}/\text{cm}^2$  for 120-fs pulses

noted that the electrons directly absorb laser energy without hydrodynamic expansion when ultrashort pulses are used.

Thermalization of the electrons cause acquisition of high kinetic energies and subsequently create an electron motion for about 1 ps, which is approximately the electron cooling time.

Energy transport from the electrons to the lattice occurs as the result of electron thermal diffusion cooling, a process that takes place only after the cessation of laser pulse because the lattice heating time is on the order of 100 ps.

Ablation is initiated when the kinetic energy of lattice in the interaction volume reaches a threshold value. Ablation continues until the kinetic energy is completely transformed into vapor energy. During ablation, the kinetic energy of the lattice is much higher than that of electrons because energy transfer slows down electron motion.

An important issue is to establish threshold fluence for ablation. Anismove et al.<sup>21</sup> described the beam-solid interactions by a one-dimensional, two-temperature diffusion model given by:

$$C_e \partial T_e / \partial t = - \partial Q / \partial z - \gamma (T_e - T_i) + S \quad (2)$$

$$C_i \partial T_i / \partial t = \gamma (T_e - T_i) \quad (3)$$

Where  $C_e$  = volumetric heat capacity of electrons,  $C_i$  = volumetric heat capacity of lattice,  $z$  = depth direction,  $Q$  = electron heat flux =  $-k_e \partial T_e / \partial z$ ,  $k_e$  = electron thermal conductivity,  $\gamma$  = electron-lattice coupling,  $T_e$  = electron temperature,  $T_i$  = lattice temperature,  $S$  = laser source =  $I(t) A \alpha \exp(-\alpha z)$ ,  $A$  = absorptivity, and  $\alpha$  = absorption coefficient

For fs-pulses, the electron-lattice coupling term can be neglected. To simplify further, the electron heat conduction term can also be ignored by assuming that the electron thermal diffusion distance (given by the square root of electron thermal diffusivity and pulse width) is less than the absorption coefficient. The hydrodynamic expansion may also be neglected. Under these conditions, the solutions to (2) and (3) for electron and lattice temperatures are given by<sup>22</sup>

$$T_e = 2 F \alpha / C_e \exp(-\alpha z) \quad (4)$$

$$T_i = F \alpha / C_i \exp(-\alpha z) \quad (5)$$

These equations imply that  $F_1 \exp(-\alpha z_1) = F_2 \exp(-\alpha z_2)$ . Thus, one can write the ablation depth per pulse as:

$$z = (1/\alpha) \ln F / F_{th} \quad (6)$$

The application of (6) to the present study yields an effective penetration depth,  $1/\alpha$ , of 1200 angstroms and  $F_{th}$  of 1.2 J/cm<sup>2</sup>. However, experimental data show that significant ablation occurs at energy fluences much lower than 1.2 J/cm<sup>2</sup>. Furthermore, this value is much higher than the 0.9 J/cm<sup>2</sup> reported by Windholz and Molian<sup>13</sup> for 248 nm, 23-nanosecond pulses.

Equation 6 could not successfully predict the threshold fluence because it assumes only linear absorption (Beer's law) and does not consider multiphoton absorption effects.

The next items of interest are the images of the surfaces obtained with SEM and AFM. Both methods are very effective at fine scale imaging, and they provide complementary information. The holes were ablated at  $0.8 \text{ J/cm}^2$  at 1,000 pulses and 10,000 pulses for the pulse width study. The images will be described in order of increasing pulse width.

With ns-pulsed lasers, the interaction processes are linear absorption (single-photon absorption) for opaque materials, the category that includes graphite is opaque because it is a semi-metal and therefore has no band gap. At high intensities, as with use of ultrafast lasers, multiphoton absorption occurs when the bound electrons of the transparent material are directly ionized by simultaneously absorbing  $m$  photons in the laser pulse. The multiphoton absorption and electron avalanche absorption mechanisms result in much smaller absorption volumes (shorter absorption depths) compared with single-photon absorption. Consequently, energy coupling is enhanced and threshold energy fluence is reduced.

Figures 10 and 11 show holes ablated with 10,000 and 1,000 (120 fs) pulses, respectively. Both these holes are extremely clean and show excellent definition with very little evidence of collateral thermal effects. At 10,000 pulses, a smooth-surfaced hole has been formed; for 1,000 pulses, the hole has not developed to a large extent.

The laser was then set for 1 ps pulse widths by increasing the distance between the mirror and the compressor grating. The results of a single hole ablated with 1,000 (1 ps) pulses is shown in Figure 12, which shows slightly pronounced thermal damage on the surrounding surface, compared with Figure 11.

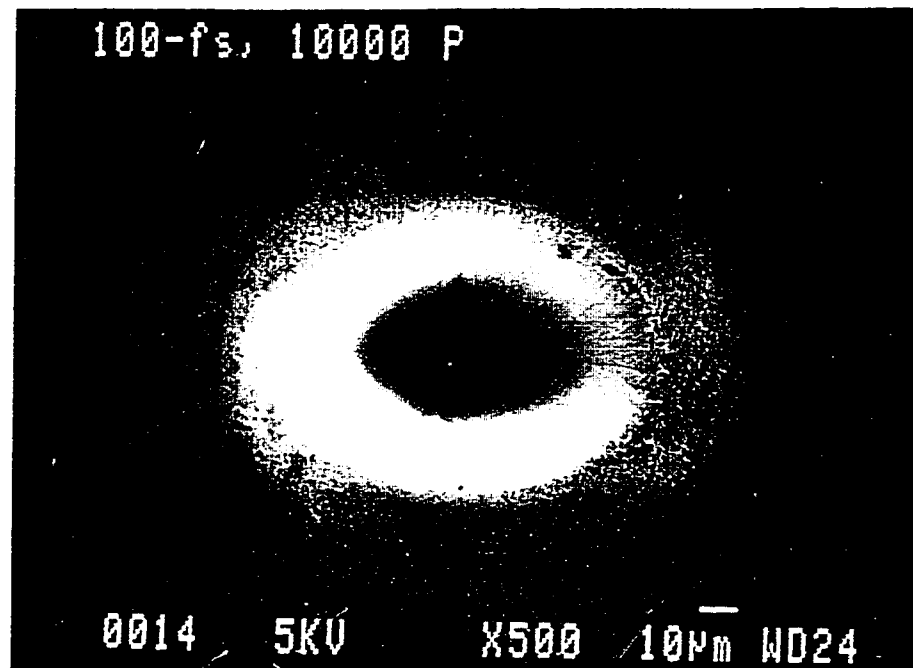


Figure 10. A hole ablated in HOPG with 10,000 (120 fs) pulses

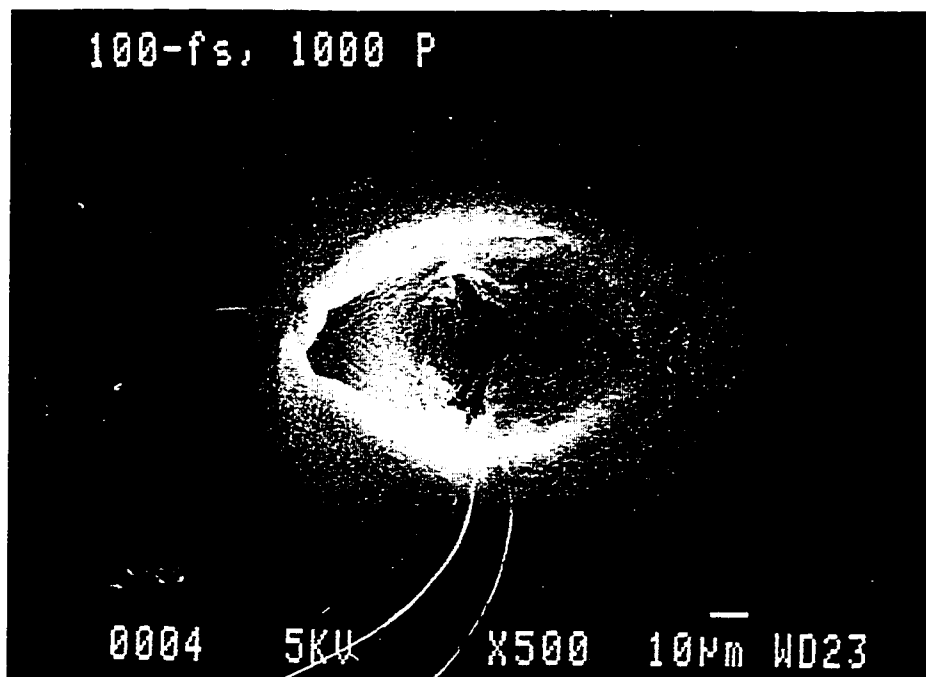


Figure 11. A hole ablated in HOPG with 1,000 (120 fs) pulses

Figure 13 (5 ps) is almost indistinguishable from Figure 12; however, a significant amount of what appears to be scattered debris from thermal shock can be seen at the lower left edge of the hole. The debris could have been generated by thermal shocking at the edge of the hole, after which the cracked material was scattered by exiting plasma.

At 10 ps this trend continues, and the edge definition on the hole is definitely degraded now (Figure 14). The graphite on the edge appears to have melted and reformed, or more likely to have undergone plastic flow.

At 20 ps, the collateral damage is more pronounced than at 10 ps. There is the halo around the holes indicating thermal shock damage, peeling of the surface graphite layers, and the less precise boundary around the hole edge. Also, with increased pulse widths, the bottom of the 1,000 pulse holes appears to be thermally degraded and does not show the effects of minor variation in beam quality as seen with shorter pulse widths. This strongly indicates thermal conduction, which averages out the effects of the beam, causing material to be removed by thermal mechanisms instead of by the effects of electron excitation.

Figure 17, which shows the effects of excessive energy, depicts a hole drilled with pulses of 1 mJ ( $10.6\text{J}/\text{cm}^2$ ). Even though the pulse width was 120 fs, there are strong indications of thermal effects attributable to etching by highly energized plasma exiting from the hole during ablation.

The differences between ablation with shorter and longer pulses, demonstrated in Figures 10-16, suggest that longer pulses created thermal waves to generate a large “halo” or vapor dust ring around the holes. Mechler et al.<sup>8</sup> observed a narrow ring similar to a halo around the ablated holes with 193-nm, 14-ns laser, and characterized the ring as a mechanically soft region consisting of nanocrystalline and turbostratic carbon.

For longer pulses, the energy transfer from the electrons to the lattice is significant, and the heat diffusion involves a volume much larger than the focus volume. The electrons and lattice are in thermal equilibrium and the peak temperatures are low. The shorter pulse duration limits the heat conduction and results in a greater degree of precision because there is a large density of free electrons and valence electrons with an ionization potential less than the photon energy. When the absorption depth is smaller than the diffusion length ( $\sqrt{Dt}$  where  $D$  is the thermal diffusivity and  $t$  is the pulse width) – as is generally the case for long pulses – the melt expulsion or plastic flow accompany the material removal, resulting in low precision. When the pulse length is reduced, the absorption depth becomes greater than the diffusion length, which leads to the localization of energy within the depth and, consequently, causes direct vaporization, resulting in high precision.

Use of AFM provides more details concerning the initial stages of ablation. The method is incapable of studying depth variations of more than a few microns, but it provides excellent quantitative information for holes 3 to 4  $\mu\text{m}$  deep. Figure 18 shows an AFM image of an HOPG surface ablated with 50 pulses, at 120-fs and  $0.8 \text{ J}/\text{cm}^2$ . A few conical structures are visible on the bottom of the crater. AFM excels at quantifying the size of structures. Figure 19 shows the fringes on the bottom of the hole in Figure 18. The laser creates these conical structures as well as wavy structures that result from interference patterns. Figure 20 shows an HOPG surface ablated by 1 ps pulses; the hole ablated is very similar to those ablated at 120 fs. Edge definition is excellent, the interior of the hole is very clean, and little debris or recast layer is observed around the hole. There does appear to be a halo, either from thermal shock or from excitation of the material by plasma exit, for approximately 30  $\mu\text{m}$  from the edge of the ablated region.

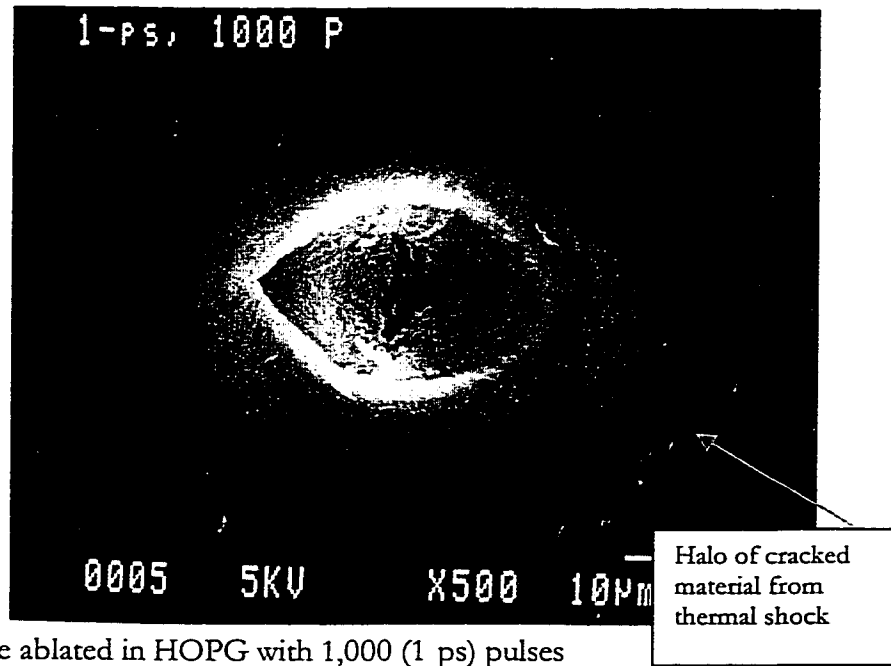


Figure 12. A hole ablated in HOPG with 1,000 (1 ps) pulses

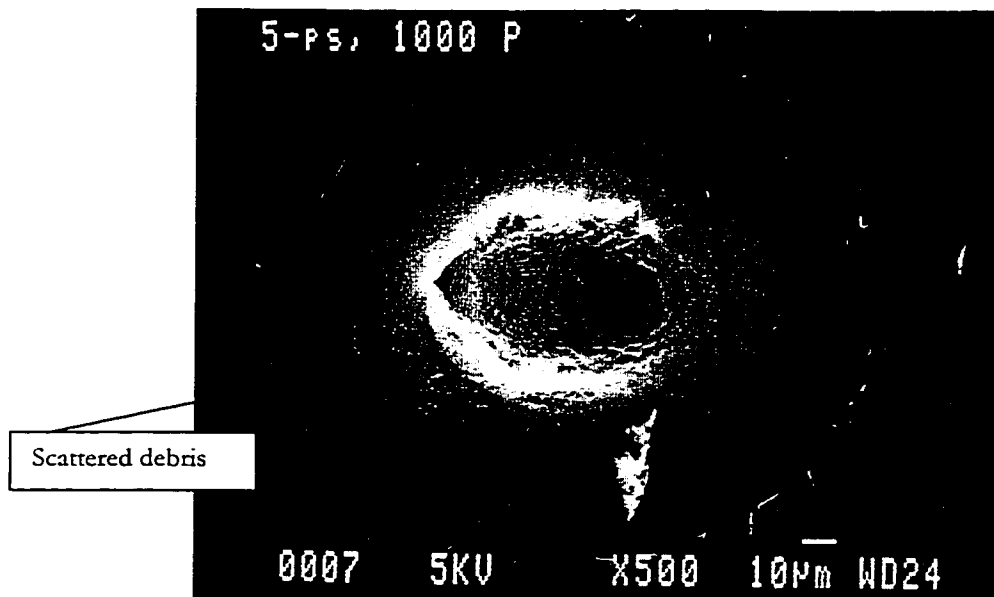


Figure 13. A hole ablated in HOPG with 1,000 (5 ps) pulses

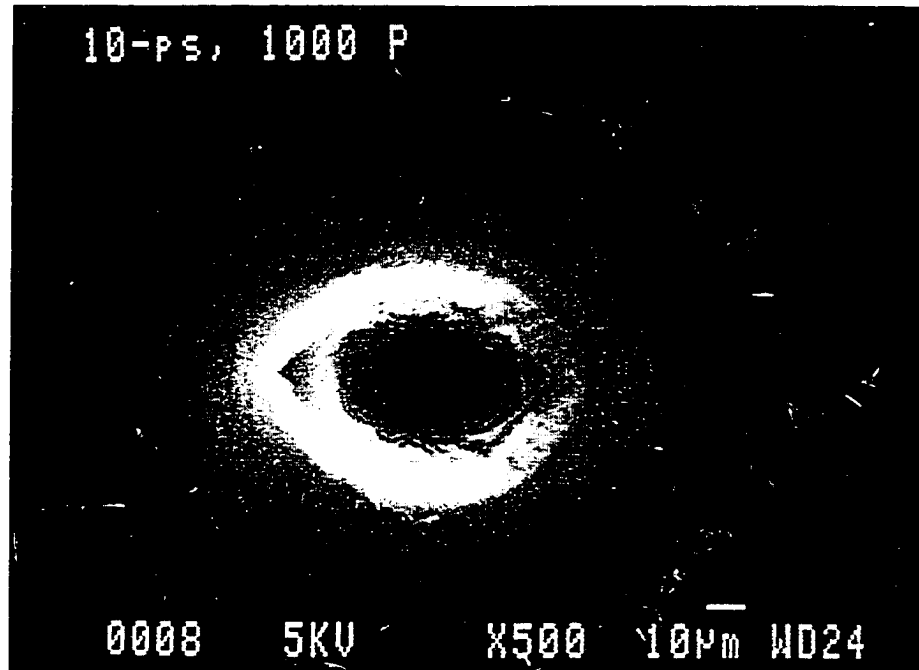


Figure 14. A hole ablated in HOPG with 1,000 (10 ps) pulses

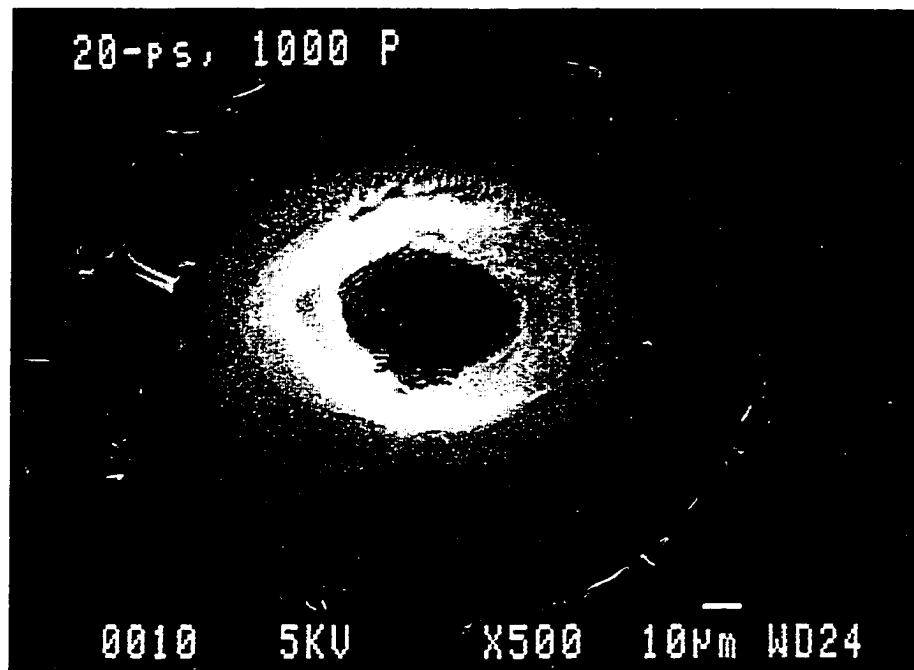


Figure 15. A hole ablated in HOPG with 1,000 (20 ps) pulses

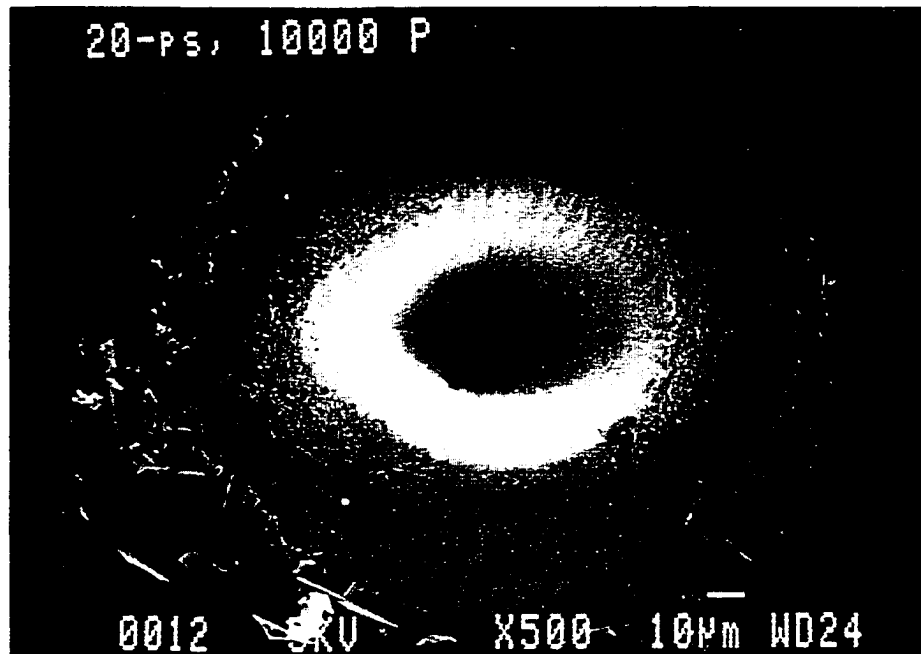


Figure 16. A hole ablated in HOPG with 10,000 (20 ps) pulses



Figure 17. Hole ablated with 120 fs, 1 mJ pulses, demonstrating the effects of excess fluence

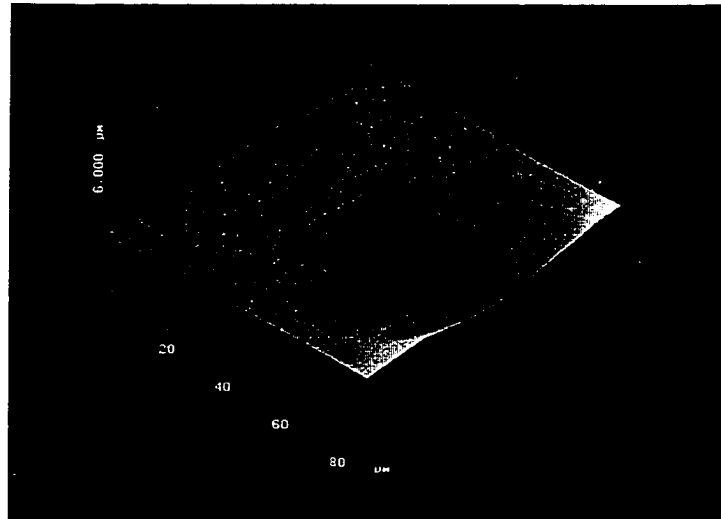


Figure 18. AFM image of HOPG ablated with 120 fs pulses

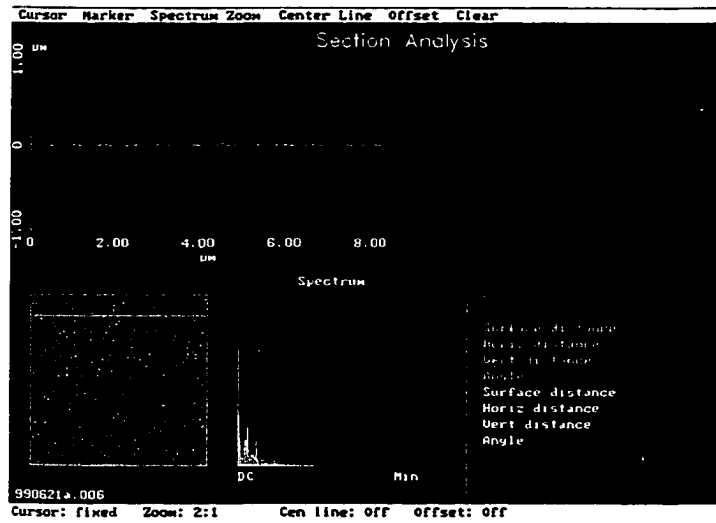


Figure 19. 825 nm fringes on the bottom of the hole pictured in Figure 18

Figure 21 shows a part of the hole ablated with 5 ps pulses. The conical structures within the hole result from preferential ablation. The halo of thermally shocked material is of approximately the same size as observed at 1 ps. There also appears to be evidence of plastic deformation around the edges of the hole, as the rim is slightly raised relative to the rest of the specimen. There is a distinct difference between results obtained with 120 fs and 5 ps pulses.

At 10 ps, the thermal effects are even more pronounced. This AFM scan, Figure 22, was not large enough to show the halo of thermally shocked material. The center of the hole has the conic structures present in many of the short-pulsed holes. There is also evidence of either plastic or viscous flow around the edge of the crater, along with evidence for a recast layer, which was not observed at 120-fs. The AFM image of the hole at 20 ps (Figure 23) shows structure similar to that of the 10-ps hole, except for substantive evidence of recast layer formation and a larger region of thermal shock. In general, the longer pulse widths appeared to caused more collateral thermal effects, larger recast layers, and reduced edge definition.

A few studies have investigated the species generated in the pulsed laser ablation of graphite<sup>8,23</sup>. Time-of-flight (TOF) and optical emission spectrometry methods were employed to characterize the ablated particles. Nanosecond pulsed lasers at 193 nm and 248 nm produced electronically-excited neutral carbon atoms as well as singly and doubly charged atomic carbon ions<sup>5,6</sup>. Arimondo et al.<sup>23</sup> reported the formation of carbon clusters, detected by time-resolved, ion mass spectrometry, in the 16 ns-pulsed, 308 nm laser vaporization of carbon. The mass spectra of laser ablation experiments conducted in vacuum showed  $C_n^+$  clusters, where n is between 2 and 7. The most abundant ions were  $C^+$  and  $C_3^+$  formation of which was attributed to recombination processes in the gas phase. Muller et al.<sup>7</sup> investigated the effect of 30 ns and 500 fs UV laser pulses of 248 nm on the ablation of graphite and reported striking differences in

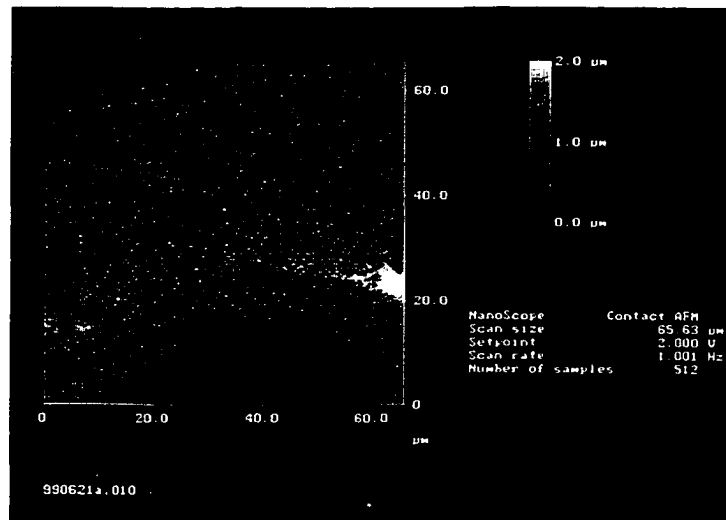


Figure 20. The edge of a hole ablated with  $0.8 \text{ J/cm}^2$  1 ps pulses

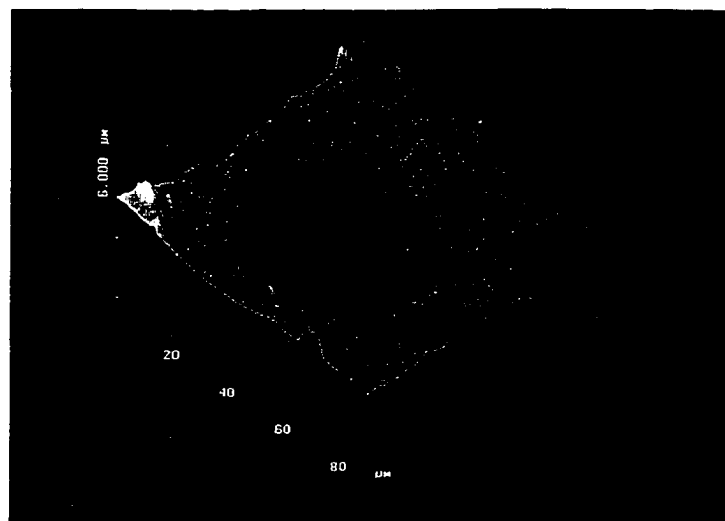


Figure 21. A hole ablated in HOPG with  $0.8 \text{ J/cm}^2$  5 ps pulses

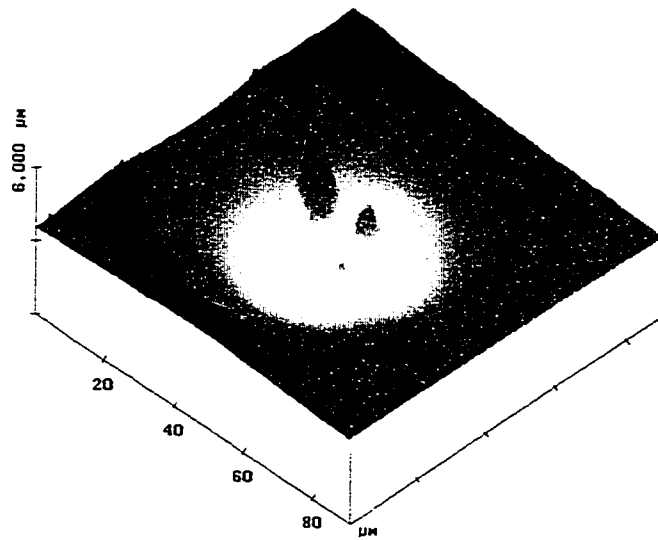


Figure 22. A hole ablated in HOPG with  $0.8 \text{ J/cm}^2$  10 ps pulses

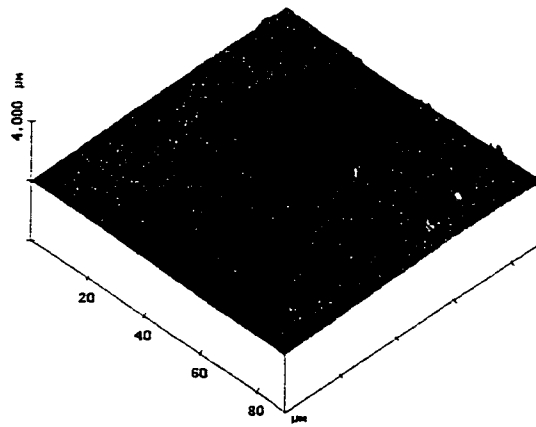


Figure 23. An AFM image of a hole ablated with  $50 \times 0.8 \text{ J/cm}^2$ , 20 ps pulses

the time-of-flight measurements of the ablated particles. The 30 ns laser pulses generated large carbon clusters over a wide distribution of kinetic energies, with a flight time to arrive at the substrate of 250 to 1000  $\mu\text{s}$ . The primary species identified were  $\text{C}_3^+$  and  $\text{C}_4^+$ . In contrast, for 500 fs pulses, there was no evidence of cluster formation, and the species had much greater kinetic energies. The flight time was narrowly distributed with an average value of 50  $\mu\text{s}$ . The major species was singly charged carbon ions.

It can thus be inferred that the kinetic particle energy, the mass distribution, and the optical emission spectra are strongly altered when the pulse width is increased. The short pulses create a higher degree of atomization as well as ionization, both of which can be attributed to multiphoton effects.

The next step in the characterization was investigation of the short-range structure of the surfaces, using micro-Raman spectroscopy. This procedure was performed on HOPG samples ablated at different pulse widths. A pure graphite surface shows a single peak, at  $1580\text{ cm}^{-1}$ . This peak is indicative of  $\text{sp}^2$  (trigonal planar) hybridization, whereas a peak around  $1330\text{ cm}^{-1}$  is indicative of  $\text{sp}^3$  (tetrahedral) hybridization.

Figure 24 shows a Raman spectrum of HOPG in an untreated, pristine state. There was only one sharp peak, at  $1580\text{ cm}^{-1}$ . Figure 25 shows the Raman spectrum of HOPG that has been exposed to  $0.8\text{ J/cm}^2$  120-fs pulses. Here, the peak at  $1580\text{ cm}^{-1}$  is reduced in intensity and broadened in wavenumber, and there appears to be a secondary peak at  $1330\text{ cm}^{-1}$ , indicating that the ablated surface is exhibiting a thin layer of amorphous carbon, with a preponderance of  $\text{sp}^2$  hybridization. Figure 26 shows the Raman spectrum for a 20 ps pulse. It exhibits the same two peaks as Figure 25, but the  $\text{sp}^3$  proportion ( $1580\text{ cm}^{-1}$  peak) appears significantly larger,

indicating a thicker layer of amorphous carbon (broad peaks are indicative of amorphous material, whereas diamond, which is pure  $sp^3$  carbon, has a very sharp peak at  $1332\text{ cm}^{-1}$ ). The mechanism of peak broadening is distortion of bond angles and short range structures from their optimal, crystal forms. This broadening is observed in many systems that have amorphous or glassy phases, including silicate glass systems and many polymers.

The Raman spectra show that the formation of a DLC peak increases with an increase in pulse width. Windholz and Molian<sup>13</sup> and later Mechler et al.<sup>8</sup> through use of Raman spectra and ns-pulses independently inferred the presence of DLC in the ablated regions of HOPG. In addition, Mechler et al.<sup>8</sup> identified the formation DLC in the halo surrounding the hole.

Figure 27 shows the Raman spectrum of HOPG ablated with a 248 nm, 23 ns excimer laser.<sup>13</sup> Comparing this spectrum to spectra of samples obtained with use of the shorter pulses provides even more evidence of collateral thermal damage of ns-pulses, mostly in the form of a broad peak indicative of  $sp^3$  hybridization.

The most plausible explanation lies in emission of the carbon species with high kinetic energies. In general, pulsed ablation creates localized changes in pressures and temperatures on the graphite surface. Carbon in the graphite form is the low-pressure, low-temperature stable phase, whereas if temperature and pressure are raised locally, then the preferred phase is  $sp^3$  and the graphite will be transformed to DLC, a process that occurs irrespective of the pulse duration. However, for ultrashort pulses, heating is very localized and the species are ejected with very high kinetic energies. The vast majority of the transformed DLC is thus removed in the ablation process.

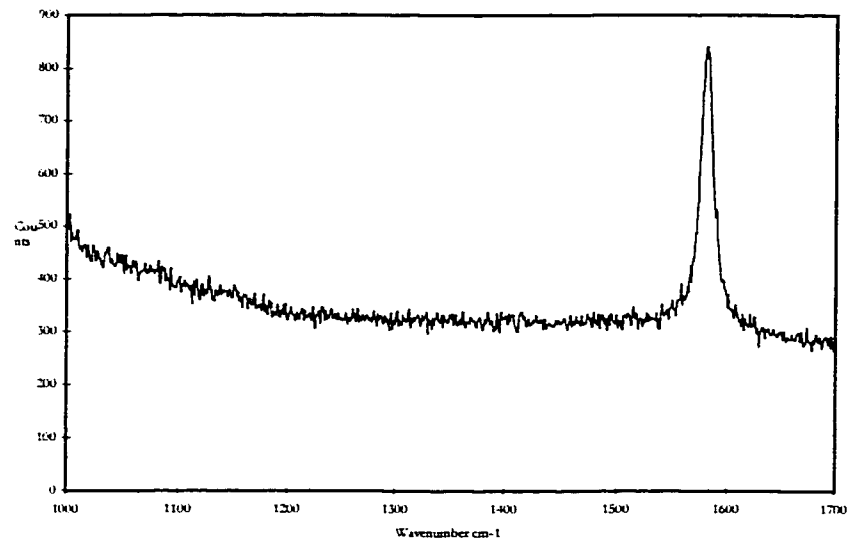


Figure 24. Raman spectrum of untreated HOPG

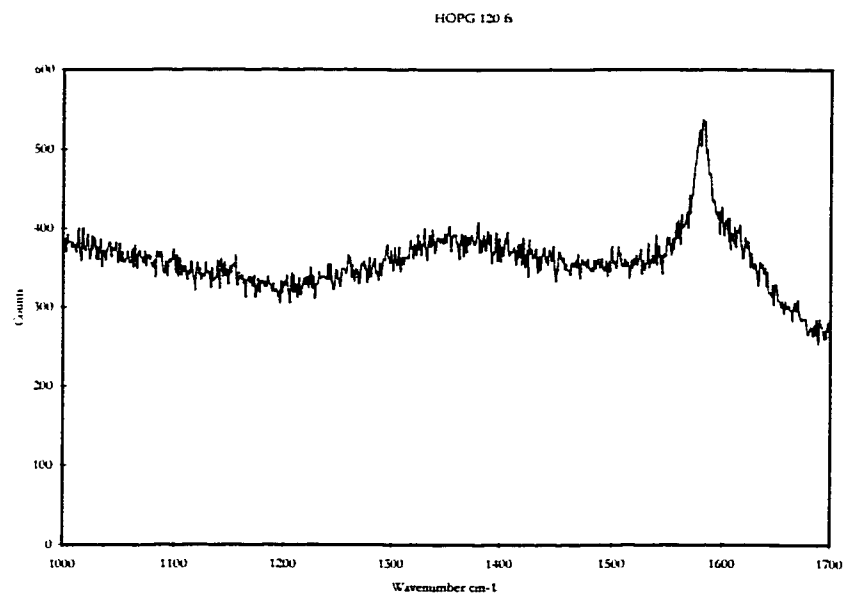


Figure 25. Raman spectrum of 120 fs treated HOPG

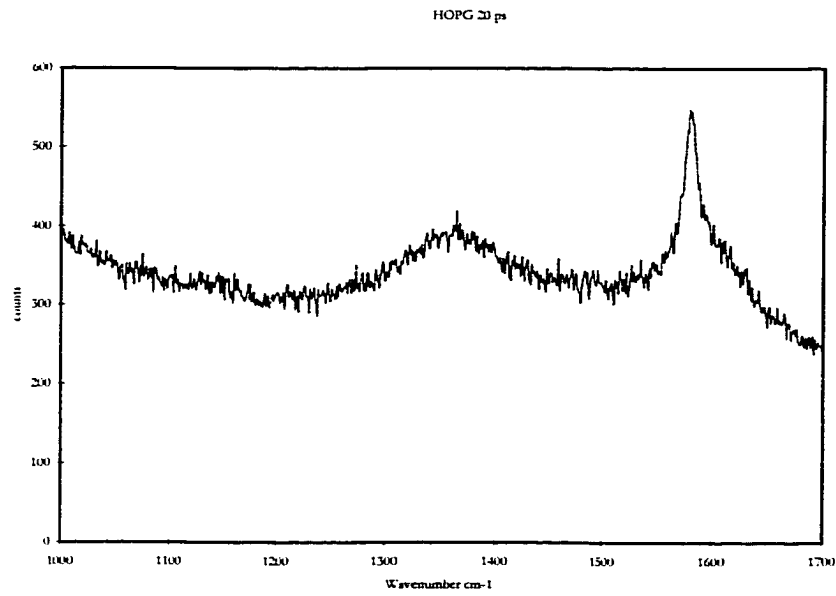


Figure 26. Raman spectrum of 20 ps treated HOPG

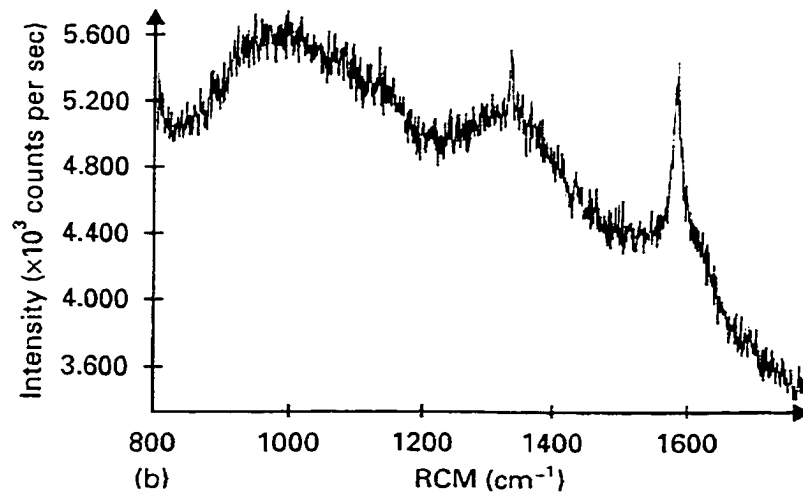


Figure 27. Raman spectrum of 248 nm, 23 ns treated HOPG

Most of the collateral thermal effects in graphite are observed within the AB plane, but the thermal shock is observed up to 30  $\mu\text{m}$  away from the edge of the hole in the 20 ps case. Evidence points to a very narrow depth in the C direction. This can be related to differences in thermal conductivity, which is 200 times greater in the AB plane than in the C direction. Also, the anisotropy between the AB and the C directions with regard to thermal conductivity indicate why saturation may be expected. An increase in laser power will cause very little increase in conduction into the material because of low conductivity along the C direction, whereas in the AB plane, increased power, especially at longer pulse widths, will create larger areas of heat affected material.

### *Conclusion*

Laser irradiation of highly oriented pyrolytic graphite was performed as a function of pulse width, using an ultrafast Ti:Sapphire laser operating at 825-nm wavelength. The effects on material removal rate and thermal damage were investigated. Wherever possible, the results were compared to those obtained with nanosecond pulsed lasers. Simple models and qualitative explanations were offered to explain the observed results. Ultrashort pulsed lasers are demonstrated to be superior to longer-pulsed lasers for micromachining of graphite with regard to their ability to form fine scale structures, as evidenced by increased definition of the features and well defined contours. There is definite evidence of decreased thermal damage on both micro- and macroscopic levels as laser pulse widths are shortened. The reduction in thermal shock is very important, as most micromachining applications would be adversely affected by reduced edge definition and increased recast layer formation. There is also evidence also evidence of reduced plastic deformation around the hole's edge, further improving structural accuracy of laser-machined structures.

## References

1. J.J. Cuomo, D.L. Pappas, J. Bruley, J.P. Doyle, and K.L. Saenger, *J Appl Physics*, 70, 1991, 1706
2. C.B. Collins, F. Davanloo, E.M. Juengerman, D.R. Jander, and T.J. Lee, *Surface Coatings Technology*, 47, 1991, 244
3. F.Xiong, Y.Y. Wang, and R.P.H. Chang, *Phys. Rev. B* 48, 1993, 8016
4. S.E. Johnson, M.N.R. Ashfold, M.P. Knapper, R.J. Lade, K.N. Rosser, N.A. Fox and W.N. Wang. 'Production and Characterisation of Amorphous Diamond Films produced by pulsed laser ablation of graphite', *Diamond Rel. Mater.*(1997), 6, 569-73
5. <http://www.chm.bris.ac.uk/pt/diamond/ablation/ab4.html>, Studies of the ablation plume arising in 193 nm laser irradiation of graphite in vacuo, 1999
6. Togashi, H.; Saito, K.; Koga, Y.; Yamawaki, H.; Aoki, K.; Kameyama, T.; Mukaida, M. Formation of large carbon cluster ions at graphite (HOPG) surfaces by laser irradiation, *Applied Surface Science*, Vol: 96-98, April 1996 pp. 267-271
7. F. Muller, K. Mann, and P.Simon, "A comparative study of deposition of thin films by laser-induced PVD with fs and ns laser pulses, *SPIE Proceedings*
8. A. Mechler, P. Heszler, Z. Kantor, T. Szorenyi, and Z. Bor, *Applied Surface Science*, 138-139, 1999, 174-178
9. [http://www.phys.ttu.edu/~tlmde/thesis/CARBON\\_NANOTUBES.html](http://www.phys.ttu.edu/~tlmde/thesis/CARBON_NANOTUBES.html)
10. <http://www.aps.org/meet/CENT99/BAPS/abs/S8775005.html>
11. C. Bower, S. Suzuki, K. Tanigaki, and O. Zhou, *Applied Physics A* 67, 1998, 47-52
12. <http://www.iit.edu/departments/pr/research/graphite.html>, Clean and inexpensive: laser machining fuel cells from graphite
13. Windholz, R., and P.A. Molian, *Journal of Materials Science*, 32, 1997, 4295-4301.
14. Shirk, M. D., and P.A. Molian, "A review of ultrashort pulsed laser ablation of materials," *Journal of Laser Applications*, V.10, No.1,1-11, 1998.
15. Liu, X., and G. Mourou, "Ultrashort laser pulses tackle precision machining," *Laser Focus World*, August, 101-118, 1997.
16. Pronko, P., S. Dutta, J. Squier, J. Rudd, D. Du, and G. Mourou, "Machining of submicron holes using femtosecond laser at 800 nm," *Opt. Comm.*, V.114, 106-110, 1995.
17. Chichkov, B.N., C. Momma, S. Nolte, A. Tunnermann, and F. von Alvensleben, *Appl. Phys.*, A 63, 1996, 109
18. Ashkenasi, D., H. Varel, A. Rosenfeld, F. Noack, and E.F.B. Campbell, *Nuclear Instruments and Methods in Physics Research B*, V. 122, 1997, 359-363.
19. Simon, P., and J. Ihlemann, "Machining of submicron structures on metals and semiconductors by ultrashort UV-laser pulses," *Appl Phys A*, 63, 505-508, 1996.

20. C. Momma, B. Chichkov, S. Nolte, F. Alvensleben, A. Tunnermann, H. Welling, and B. Wellegehausen, *Optics Communications*, 129, 1996, 134-142.
21. S.J. Anisimov, B.J. Kapeliovich, and T.L. elman, *Sov. Phys. JETP* 39, 1974, 375.
22. C. Momma, S. Nolte, B. Chichkov, F. Alvensleben, and A. Tunnermann, *Applied Surface Science*, 109, 1997, 15-19.
23. E. Arimondo, F. Calderazzo, F.Fuso, and C.Toffi, *Applied Physics A*, 66, 407-411, 1998.

## CHAPTER 9. GENERAL CONCLUSIONS

Of currently available tools, lasers are the most promising for machining diamond and graphite because they are non-contact and have the ability to form materials regardless of the materials' mechanical and physical properties. For example, laser machining is dependent on neither the hardness nor on the crystallographic structure of carbon. Also, lasers can quickly remove material without extensive surface pretreatment, thereby allowing carbon to be machined into shapes otherwise unattainable. However, until now, diamond machined with lasers had to undergo post-machining processes to restore the surface to a pure diamond structure, and to improve accuracy, precision, and cleanliness of the freshly ablated surface. Ultrashort pulsed lasers which are the latest tools, have been shown conclusively to eliminate many of the drawbacks of conventional laser machining, while improving on the minimum feature size attainable.

A detailed investigation of ultrashort pulsed ablation of the two phases of carbon led to the conclusion that this tool is superior with regard to the following:

- Increased photon absorption efficiency (decreased absorption depth) from multiphoton absorption and electron avalanche ionization, resulting in lower threshold and more precise ablation.
- Improved energy coupling, yielding higher material removal rates.
- Elimination of secondary phase generation in diamond.
- Greatly reduced secondary phase generation in HOPG.
- Elimination of recast layers.
- Elimination of mechanical thermal shock in graphite.
- Improved feature definition.

- Improved hole stability as the result of eliminating liquid phases.

The models in this work provided the following predictions that helped to explain the conclusions drawn in this study:

- Steep thermal gradients, localized energy
- Relatively low electronic heat capacity up to  $\sim 4000$  K
- Very high electron temperatures, indicative of very dense plasmas
- Rapid graphitization of (111) surface under electron excitation
- (001) diamond surface that is more stable than (111) surface under both thermal and electronic excitation

For diamond and a typical laser ( $\lambda > 227$  nm) with a pulse width in the ns-ms region, absorption of the laser light is initially small, and the damage threshold is unpredictable because of variations in defect size and population in different diamond samples. Therefore, the samples usually go through an incubation period during the first few laser pulses, in which color centers and other defects grow so as to increase laser absorption. It has been hypothesized that a small layer of graphite residue is created and retained on the surface after a laser pulse, and that this is why the multishot damage thresholds on diamond and graphite are low and of the same order. For ultrashort pulsed laser ablation, processes such as multiphoton absorption and electron avalanche make incubation period unnecessary, so that the material is ablated predictably from the first shot. This improves the overall resolution of feature sizes and makes laser machining an easily predictable process because of the lack of variation.

Improved energy coupling also contributes significantly to the increased efficiency of the ablation process as the pulse width is reduced. More of the laser energy is used to remove material, instead of being diverted into other processes, such as thermal diffusion, reflection, and

other radiative processes. Lower energy pulses can be used to remove material in a time efficient manner, thus preventing many of the other phenomena that result from excess energy.

Reduced collateral thermal damage is proven to be a major benefit of the ultrashort pulsed laser ablation of carbon. All the physical evidence presented in this work indicates that pulses less than 1 ps create surfaces having greatly improved chemical purity and reduced collateral damage. The chemical purity of diamond surfaces is improved compared with that obtained by use of longer ns-pulsed lasers, regardless of laser wavelength. Graphite shows similar behavior, although results are somewhat less clear when times fall below about 5 ps, because lasers create intense temperatures as well as intense pressures during a very short time. Because graphite is the phase of carbon that is stable at lower pressure, it is not surprising that some of the material has been converted to an amorphous state with an increased amount of  $sp^3$  hybridized carbon. However, this conversion is minimized if the pulse width is decreased. In graphite there is definite evidence of macroscopic thermal effects when the pulsed width is above 5 ps; there is evidence of increased thermal diffusion, and some evidence for transient existence of liquid phase during the ablation process. In general, the presence of liquid in an ablation process leads to many undesirable effects, such as instability of hole drilling, which is a major concern, especially in high aspect ratio holes.

Diamond has been shown to remain more stable than graphite under laser ablation conditions. Clearly, for creating precise shapes and structures in diamond, ultrashort pulsed lasers are the ideal tools at this time. The solid-state lasers, such as the CPA Ti:Sapphire laser are the most promising industrial solutions, offering the best combination of pulse width, repetition rate, beam quality, and total power of any of the ultrashort pulsed lasers developed so far.

## CHAPTER 10. FUTURE RESEARCH

This body of work has thoroughly investigated the processes of ultrashort pulsed ablation of diamond and graphite. However, a few other experiments and model improvements could more accurately explain many phenomena, primarily, because the experimental work in diamond is still incomplete. A more detailed study using both single crystal and CVD diamond would be enlightening. The first study that needs to be done would experimentally determine single shot ablation thresholds with regard to pulse width. Further characterization of diamond ablated under various pulse widths and energy conditions would also yield information that could be used to create procedures most appropriate for machining specific structures. Such characterization would include a study of the dependence of ablation rates on fluence and pulse width, a study to determine if spot size affects ablation rate, and further Raman analysis of ablated surfaces at longer pulse widths and higher energy fluences. The Raman data would give an indication of the limits of these parameters so as to guarantee that a pure diamond surface remains after ablation.

With regard to modeling, improvements could be achieved in both finite-difference prediction of the temperature profile and in the tight-binding simulation. For the finite-difference calculations, the largest gains to be made are in improving the modeling of the absorption processes and the electron-lattice coupling, as well as the numerical methods used. At present, the very large gradients tend to produce numerical instabilities. Incorporation of a higher order solver should help eliminate many of these problems. The absorption processes are currently modeled by assuming complete absorption of energy at the surface node, although the process is not that simple. It would be a great improvement if processes such as multiphoton absorption, electron avalanche, and the effects of some of the nearly instantaneous phase changes could be more accurately modeled. The electron lattice-coupling is a very complex

process, and is therefore difficult to model. It may help significantly to obtain gated spectroscopic measurements of the ablation process, to ascertain the actual temperatures and plasma conditions.

Finally, future molecular-dynamics experiments involving thousands or millions of atoms will be possible as computational resources become cheaper and more powerful. Improvements in TBMD could also be achieved by modeling the effects of thermal gradients, with a larger distribution of nonequilibrium electron and lattice excitation states (e.g., electrons at very high and lattice at moderately high temperatures, instead of high temperature electrons and room temperature lattice), and by using improved boundary conditions. Beyond TBMD, first-principles potentials could be used, which may be even more accurate and may not have the limitations of the plane-to-plane attractive forces in graphite. Ultimately, a simulation that combined the finite-difference and molecular dynamics calculations would be extremely informative; it would allow the simulations to interact, providing better estimates of current material properties and states to each simulation.

Improved understanding of these processes is not only possible, it is essential to the technological improvements they will drive. Miniaturization of mechanical systems is the primary beneficiary of this technology; however, there are many other applications in which it will be necessary to understand how and why these processes occur.

## APPENDIX A: TITANIUM SAPPHIRE LASER SYSTEM

The system used for most of the laser ablation studies in this work was a chirped pulse amplified Ti:Sapphire laser system. It consisted of several components, including a modelocked oscillator, a pulse stretcher, a regenerative amplifier, an optional power amplifier, and a compressor. The system will be explain from seed pulse generation to the actual amplified pulse output. The first stage was the mode-locked Ti:Sapphire oscillator that was optically pumped by an argon ion laser. This produced low energy ultrashort pulses with several megahertz repetition rates. These pulses were then sampled to drop the repetition rate to 1 kHz. They were then stretched using the diffraction gratings and mirrors in the beam stretcher, which made the pulse width much longer, it went from around 120 fs to 500 ps. One property of an ultrashort laser pulse is a broad line width, or in other words the spectral purity of the beam is much broader compared with other lasers. This means that, depending on the way the stretcher is set up, the longer wavelength light take either more or less time to go through the stretcher. This changes the spatial distribution of the wavelengths of light within the pulse. Figure 1 shows the results of an optical stretcher on the distribution of light.

This longer pulse can then be amplified safely (the pulse must be stretched, otherwise the amplification will increase the intensity of the light to be well above the damage threshold of the amplification medium). Figure 2 shows the regenerative optical amplifier. This is another laser cavity where the seed pulse is brought in, then passed twice through an optically pumped Ti:Sapphire rod to raise the energy of the pulse from several microjoules to around 2 mJ. The Ti:Sapphire rod is pumped with lasers that are either frequency doubled Nd:YAG or Nd:YLF operating at approximately 532-nm. The pulse may then be further amplified by running it through another amplifier to get nearly 8 mJ per pulse, although for these experiments that much energy was not needed. The pulse was then passed through the compressor, a set of

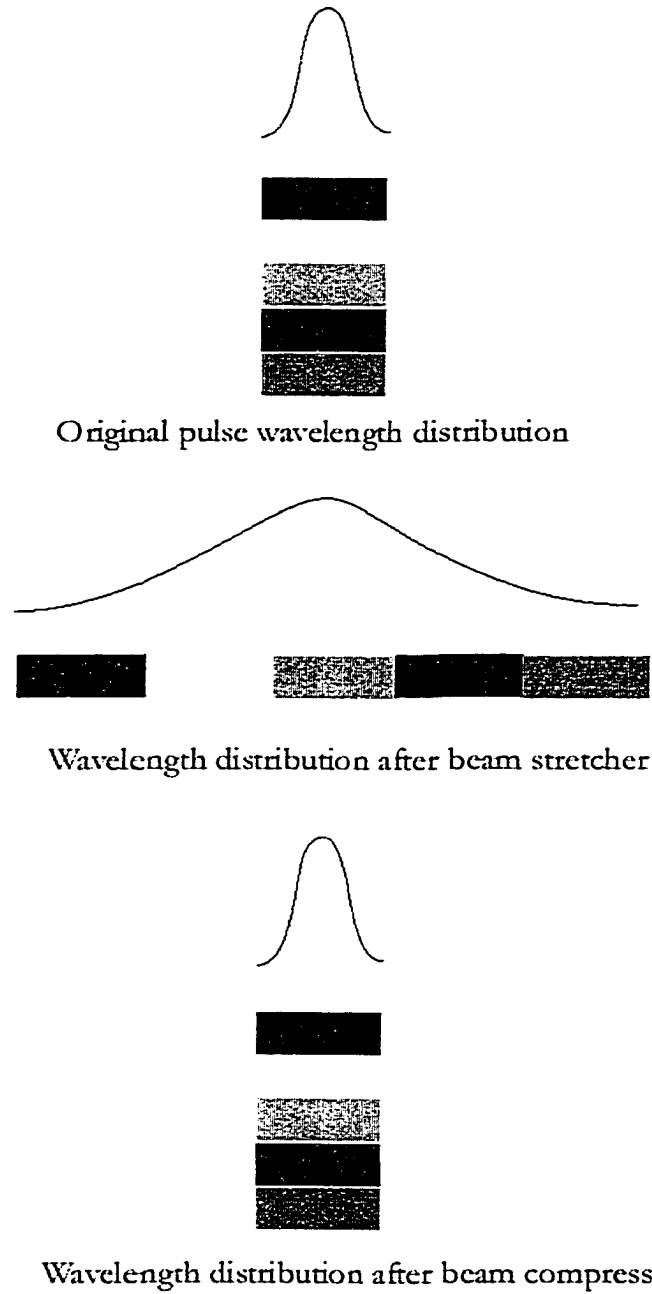


Figure 1. Distribution of wavelengths in space as generated from the oscillator, as it is after the stretcher for safe amplification and after the compressor so that the pulse can be used at its maximum intensity

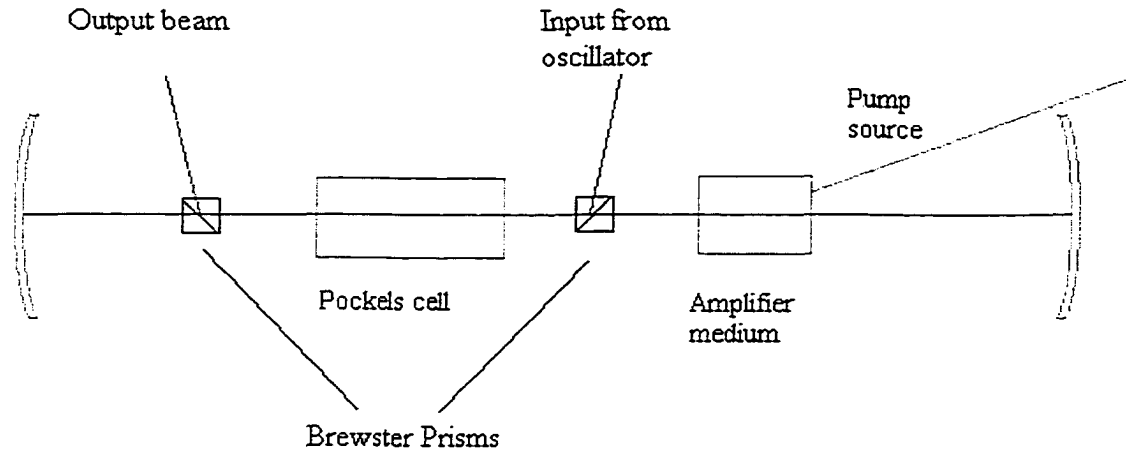


Figure 2. Diagram describing a regenerative amplifier

optics very similar to the stretcher, except they were larger in scale so that the power amplified beam could be distributed over a larger area to prevent optical damage. They were set up to restore the spatial distribution of the wavelengths to their original 120 fs distribution. That means that the longer wavelengths that took longer to go through the stretcher went more quickly through the compressor, and vice versa for the shorter wavelengths. It should be noted that the efficiency of the compressor is on the order of 60%, so you need to put in nearly double the energy that you want in the final pulse. The beam was then delivered to the focusing optics and the workpiece.

The laser beam was directed by reflective dielectric coated fused silica mirrors (metal mirrors are not nearly as efficient) to the focusing lens and through the anti-reflection (AR) coated optical window in the vacuum chamber. Figure 3 shows a typical configuration for ablation studies. It was very important that the window be very close to the lens to prevent optical damage from occurring in the window. This prevented the beam from becoming too

concentrated; however, the lens could not be placed inside the chamber as it would have been coated with the ablated material, destroying a ground optic that is much more expensive than the flat windows. Once the beam is concentrated, air can cause a condition called self-phase modulation, a condition that leads to beam distortion, loss of power, and loss of coherence, all of which have deleterious effects on precision machining. Processing took place in a vacuum below  $10^{-4}$  torr to avoid these problems. The laser operated continuously, and the beam is controlled by the use of a mechanical shutter, which was driven electronically. Therefore, the ability to count pulses is limited to opening the shutter for a specific amount of time. If 100 pulses were desired, the shutter was opened for 100-ms. It should be noted that it was very difficult to try to get a single pulse, or even a small number of pulses, say 10, as a 10 ms opening of the shutter may admit 9 to 11 full pulses. If one is working with more than 100-1000 pulses, then the loss of one pulse is insignificant.

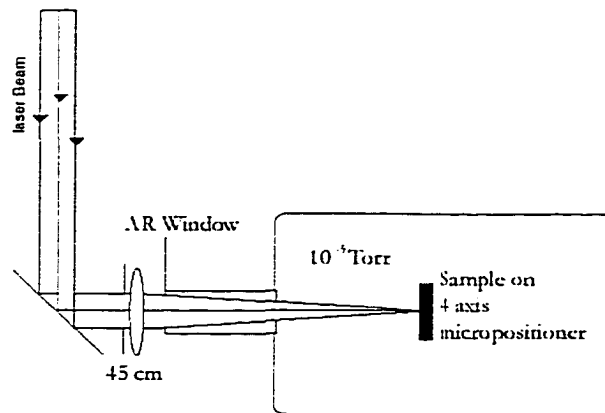


Figure 3. A typical experimental setup for ultrashort pulsed laser ablation experiments.

For the ablation studies, the sample material was then mounted on a computer controlled 4-axis micropositioner inside the vacuum chamber. The diameter of the beam when it entered the lens was approximately 12 mm. Beam diagnostics were carried out using a pass-through

configuration where the beam, without the sample in place, was imaged onto the photocell of a CCD camera. Placing a reticle where the sample was to be mounted ensured that the beam characteristics were accurately measured at the sample's surface. The image of the reticle was then brought into focus by moving the imaging lens and/or camera so that the image was in focus on the CCD surface. Then, as the focusing lens was adjusted, the camera and beam analysis software could directly measure the spatial distribution of the energy in the spot. Figure 4 shows the general layout of this kind of beam analysis. This arrangement may seem very complex, but it removes much of the guesswork from positioning of optics, as very small displacements can have significant effects.

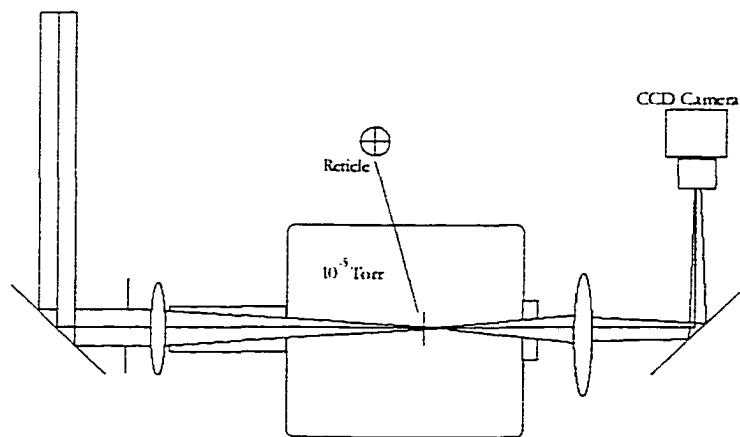


Figure 4. Beam diagnostics setup

Measurement and verification of the pulse width is performed by the use of an autocorelator. This is similar to a Michelson interferometer, where the beam is split into two components using a partially silvered optic called a beam splitter. The two beams are then passed off of mirror and crossed into a frequency doubling crystal. Frequency doubling is a

process whereby two photons of the laser beam interact with each other within a material, and become a photon of light with half the wavelength (double the frequency) of the original light. This process is a strong function of the intensity of the light. Also, since the duration of the pulses are so short, there are strong spatial effects too. A 100-fs pulse has a wavetrain, that is the length of the electromagnetic wave in vacuum, is 30  $\mu\text{m}$  in length. This characteristic was used to measure the pulse width of the light. The doubling only occurs strongly when the two beams overlap, therefore, if one observes the size of the illuminated region in the crystal, then the pulse width can be extracted by determining the size of the illuminated region. The size is directly in proportion with the length of the electromagnetic wave, a smaller, more intense region is indicative of shorter pulses, where a broader, less intense region indicates that the laser is emitting longer pulses than optimum. It is essential that the auto correlator be in alignment, a few microns of misalignment can destroy the ability to take measurements. The illuminated region is often observed with a CCD camera, which can be calibrated with beam diagnostic software so that the number of pixels strongly illuminated can be correlated to the pulse width.

## APPENDIX B. FINITE-DIFFERENCE MODEL

The finite-difference model created for this research was a one-dimensional model. A one-dimensional model was used for simplicity and computational efficiency. Only one dimension is sufficient because the typical spot diameter is 10-100  $\mu\text{m}$ , whereas the typical ablation depth is 10 nm. The model essential deals with heat transfer associated with electrons.

Table 1. Nomenclature

Symbol	Description	Symbol	Description
$n$	Node number	$C_v$	Electrons constant volume heat capacity
$m$	Step number in time	$T_n^m$	Temperature of the electrons in Kelvin
$\Delta x$	Distance between nodes	$t$	The time in seconds
$\Delta t$	Length of time in one time step	$K$	Thermal conductivity of the electrons
$l$	Mean free path of electrons	$A(t,x)$	Laser light absorption function
$v$	Electron velocity	$\epsilon$	Energy of an electron state
$\tau$	Mean time between electron collisions	$p(\epsilon)$	Density of states function
$F(\epsilon)$	Fermi function		
$k_b$	Boltzmann's constant		

In this model the material is treated as a series of nodes that transfer heat from one to the next. The nodes are parallel to the direction of the incident laser beam and model the electrons

that react quickly to optical excitation and equilibrate among themselves very quickly. The tightly bound ions, which interact with the electrons slowly and not at all with the optical photons, are ignored for the time-scale of these simulations (which should be on the order of 100-500 fs). The electrons and the lattice take on the order of 1-2 ps to come to equilibrium. This scenario would be quite different in longer pulses (5-ps and longer) where it can be safely assumed that the electrons and lattice are near equilibrium, and therefore any separate treatment for them can be neglected.

The equation used to describe the heat transfer is as follows in Equation (1):

$$C_v \frac{\partial T}{\partial t} = \frac{\partial}{\partial x} K \frac{\partial T}{\partial x} + A(t, x) \quad (1)$$

The left side of the equation shows the time dependence of the temperatures, where the  $C_v$  is the volume dependent heat capacity. The  $A$  is a function that covers the absorption of energy from the laser light by the electrons; it is dependent on the intensity of the light. For this simulation, it is assumed that all light is absorbed by the surface node,  $n=0$ . This differential equation was solved by finite differencing as follows. The following equation represents the above equation, except that the partial derivatives have been replaced by difference equations, Equation (2):

$$\Delta T_n^m = \frac{\Delta t}{C \left( \frac{T_n^m + T_n^{m-1}}{2} \right)} \left[ \left( \frac{K(T_{n-1}^{m-1}) - K(T_n^{m-1})}{2\Delta x} \right) \left( \frac{T_{n-1}^{m-1} - T_n^{m-1}}{2\Delta x} \right) + K \left( \frac{T_n^m + T_n^{m-1}}{2} \right) \left( \frac{T_{n-1}^{m-1} - 2T_n^{m-1} + T_{n-1}^{m-1}}{\Delta x^2} \right) \right] \quad (2)$$

For each node and time step a change in temperature is calculated, and used to predict the next time step's temperature profile. However the heat capacity and thermal conductivity used here are not tabulated the way that other materials, such as copper are. Although diamond has the highest thermal conductivity know, it conducts using phonon modes and this model is

examining the electronic conduction in the material. Electron conductivity values are readily available for metals, but they are not well tabulated for electronic insulators such as diamond.

Diamond's electrons are tightly bound in their valence band and it takes approximately 5.2 eV of energy to excite one to the conduction band. In silicon the band gap is 1.2 eV, and in metals there is no gap that the electrons must pass through. Free electron model concepts have been successfully used to calculate the electronic heat capacity and thermal conductivity of low band-gap semiconductors and metals for many years. But, diamond's band gap is so large that it invalidates the assumptions made with the semiconductors, and necessitates the formulation of the heat capacity in a different manner. Computational materials science has allowed an approach where the electronic structure was calculated, and then used to determine the heat capacity. Therefore if one has access to the calculated density of states and understands solid-state physics theory, the calculation of the electronic heat capacity and thermal conductivity can be numerically solved by a computer and predicted accurately. The density of states function ( $\rho(\epsilon)$ ) is simply a function that indicates the number of available energy states for an electron available to occupy at any given energy. In diamond the valence electrons are located in a filled band that exists from  $-21.0$  eV to  $0$  eV, and the conduction band starts at  $5.2$  eV and continues up from there. In a DOS attained from Papaconstatopoulos<sup>1</sup> that was calculated using the linear augmented plane wave method, the band structure was predicted accurately, however the calculated band gap was too small at  $4.8$  eV, so it was increased by adding  $0.4$  eV to every state above  $0$  eV. Since we are predicting extremely high excitation states, the highest energy of the conduction band states needs to be considerable in excess of  $14$  eV. The free electron approximation was used for the states available higher than  $14$  eV, this was done by taking the equation for the free electron density of states<sup>2</sup> and subtracting  $5.2$  from the energy to compensate for the band gap. The

number of states per volume present in diamond is the valence of the atom (carbon = 4), times the number of atoms per unit cell, (for diamond this is 8), divided by the volume of the unit cell. At absolute zero, only the states below 0 eV are filled. As the electrons are heated up, the states above the band gap become partially occupied. The Fermi function is used to describe the probability of occupation. The number of states in the material is always constant, regardless of temperature. The equations to define this are as follows:

$$n = \int_{-\infty}^{\infty} p(\epsilon) \cdot f(\epsilon) d\epsilon \quad (3)$$

$$u = \int_{-\infty}^{\infty} \epsilon \cdot p(\epsilon) \cdot f(\epsilon) d\epsilon \quad (4)$$

$n$  is always constant,  $u$  is the energy of the system,  $p(\epsilon)$  is the number of states at the energy level  $\epsilon$ , and  $f(\epsilon)$  is the Fermi function, which is defined as follows Equation (5):

$$f(\epsilon) = \frac{1}{1 + e^{\left(\frac{\epsilon - \mu}{k_b \cdot T}\right)}} \quad (5)$$

$T$  is the temperature in Kelvin,  $\mu$  is the chemical potential, and  $k_b$  is Boltzman's constant. When using these equations,  $n$  must be found by integrating all of the states below 0 eV; this is the number of states present at zero Kelvin. For this simulation the DOS was presented in arbitrary units, so they were normalized to the expected number from the number of valence electrons. Equation (3) was used to solve for  $\mu$  at integer temperatures up to 150,000 K, which was done by adjusting chemical potential so that the number of occupied states was equal to the number of valence electrons.  $\mu$  has units of eV and its magnitude is usually somewhere in the band gap, at least for large band gap materials. Once  $\mu$  is known, then the total energy of the electrons can

be calculated by using Equation (4). The derivative of  $u$  with regard to  $T$  is the heat capacity of the electrons, this was found using numerical differentiation. The thermal conductivity is related to the heat capacity as follows:

$$K=(1/3)v^2\tau C_v \quad (6)$$

$v$  is the velocity of the electrons,  $\tau$  is the mean time between collisions of electrons, and  $C_v$  is the per volume electronic heat capacity. Alternatively, the thermal conductivity can be defined with regard to mean free path in place of the electron collision time:

$$K=(1/3)v\lambda C_v \quad (7)$$

The velocity was then determined from the slope of the electron bands from the band structure of diamond and the mean free path was assumed to be on the order of the crystal size in the CVD diamond as grain boundaries are very effective at scattering electrons. With these calculation performed, the physical properties were then applied to the difference Equation (2).

The determination of the temperature profile requires that the partial differential equation be solved with appropriate boundary conditions. The energy was input into the system at the surface where the laser energy is incident. The other end, deep within the solid, was held isothermally at room temperature. This treated the solid as an infinite body. This assumption is reasonable in that the temperature of most work pieces ablated with ultrashort pulsed lasers experience bulk temperature elevations of at most 2-3°C. It was necessary to use approximations for the heat capacity and thermal conductivity so that an average of the initial and final temperature can be determined so that median values can be used to improve the simulation's accuracy. Therefore, Equation (2) was solved so that the predicted temperature was in agreement with the temperature used to find the average temperature for the heat capacity and thermal conductivity. This was done by using iterations to continually improve the

approximations so that they were in good agreement. The bounds of the temperature were known. The temperature could not be higher than the node above, or lower than the node below. This allowed for the use of a solver that used an initial guess and the information that the predicted temperature was lower or higher than the guess to solve for the proper change in temperature. If the value was higher than the guess, the heat capacity was too low, therefore the guessed temperature was raised, and current temperature set as the new lower bound.

Conversely, if the new temperature was lower, then the heat capacity was too high and a lower temperature guess was used, and the old guess was set as the upper limit. The heat capacity was an increasing function, therefore this method worked well. There was some instability if the time-step was too large, or the distance between the nodes was too small. The limits on this were:

$$\frac{K}{C_v} \frac{\Delta t}{\Delta x^2} \leq 1 \quad (10)$$

This mandate small time-steps, around  $10^{-16}$  s, and a node distance of  $5 \cdot 10^{-9}$  m. All of this was coded in C++.

### *References*

1. D. A. Papaconstatopoulos, *Handbook of the Band Structure of Elemental Solids*, 230 (Plenum Press NY, 1986).
2. Ashcroft, N. W. and N. D. Mermin, *Solid State Physics* (Harcourt Brace College Publishers NY, 1976),

## APPENDIX C. TIGHT-BINDING MOLECULAR DYNAMICS

For this study the use of a molecular dynamics (MD) simulation was necessary because ultrashort pulsed laser are capable of creating conditions in materials that have not been well researched previously. The conditions are such that the electrons are highly excited, while the lattice, or core atoms are not significantly energized. This was expected to lead to fundamental changes in the structure of the material. For this reason, MD was chosen as a method to study these phenomena, which are nearly impossible to observe in physical experiments. MD is a computational method whereby the equations of motion are solved for each atom within a material. The way this is performed varies from method to method. Each method has tradeoffs between computational efficiency and physical accuracy.

Tight-binding molecular dynamics (TBMD) was chosen for this work because it has an excellent balance of accuracy and computational efficiency that is unachievable with most other methods. TBMD uses a potential that takes uses quantum-mechanical calculations to predict attractive forces and overall energy of the system. However, it is not as computational intensive as the more complex *ab initio* method.

Tang et al.<sup>1</sup> developed the tight-binding molecular dynamics used in this body of research. This method is novel for TBMD in that it uses compensations for multi-center effects in the two-center integral approximation, and is therefore able to change interatomic parameters depending on the bonding environment, for example the bond length is assumed to be longer for atoms with a higher coordination number. This is essential for modeling materials that have more metal character than tightly-bound covalent electrons, that is they have significant amounts of metallic bonding.

This method uses three different equations to model the individual time-steps or hops that atoms undergo in the simulation. The first equation is a modified two-center approximation with two equations that modify it. The first modification is an equation that acts as a screening function that compensates for the presence of the electronic screening from atoms located between the two atoms for which calculations are being performed. The second function is used to modify the preferred interatomic distance depending on the effective coordination number, larger coordination numbers yield weaker interactions between atoms, and therefore larger interatomic spacing. Three orbitals were used in the tight-binding Hamiltonian for carbon, the s orbital and three p orbitals, which would constitute the valence orbitals. The interaction of these is computed for each atom in the simulation; they are strongest for the nearest neighbors. The shielding function is present to change the character of the material from being more free-electron metal like to increasingly covalent, localized electrons. This is important for a system that has both states possible. Graphite has more metal character (it is a semi-metal) with some free electrons, is one extreme for carbon, and diamond which is a covalent insulator, has strongly bound electrons, and represents the opposite extreme. The TBMD method has been shown to accurately model the behavior of each, except that it does have a drawback in that it does a poor job of modeling the layer to layer forces in graphite. The orbitals only model attractive forces, so another term is necessary. This is to model the pairwise repulsive force, which physically comes from the Pauli exclusion principle.

### *References*

1. M. S. Tang and C. Z. Wang, Phys Rev B 53, 979-982 (1996).

## ACKNOWLEDGEMENTS

I thank the following people and organizations for their support during this project. I would like to acknowledge the work that Dr. Cai-Zhuang Wang has done for this project. He has been my principle source for molecular dynamics simulations, mentoring, and advice. I truly would not have understood half of the material that is in this dissertation without his efforts to teach me about solid state physics. His efforts go way above and beyond the call of collaboration, and I am truly grateful. I would also like to acknowledge the hours that Dr. Prusa spent with me discussing the numerical modeling for the finite-difference model. Although many of the concepts are simple, coming up with efficient code was not, and his advice and mentoring on this part of the project was key to my being able to complete it. I would like to acknowledge Dr. Molian and Dr. Malshe for writing the grants to get this work supported, and for their continued motivation throughout the project.

Finally, this work has been funded by the National Science Foundation under project (DMI 9622518). Thank you for your financial support of this important work.